UNIVERSITY OF CALIFORNIA,
IRVINE

Synthesis and Purification of DNA-Like Nanowires: From Natural to Artificial

THESIS

submitted in partial satisfaction of the requirements
for the degree of

MASTER OF SCIENCE

in Materials Science and Engineering

by

Jonah-Micah David Jocson

Thesis Committee:
Professor Alon A. Gorodetsky, Chair
Professor Hung D. Nguyen
Professor Frank G. Shi

2015

TABLE OF CONTENTS

LIST OF FIGURES

LIST OF TABLES

LIST OF SCHEMES

ACKNOWLEDGMENTS

I would like to thank my advisor, Professor Alon A. Gorodetsky, for the continued guidance and support he has provided over the past few years. I would like to thank Professor Hung Nguyen for being part of my thesis committee and for being one of our collaborators. I would also like to thank Professor Frank Shi for giving his time to be a member of my thesis committee.

I would additionally like to thank the many people that I have had the pleasure of working with during my time in the Gorodetsky Group. In particular I would like to thank David Ordinario and Long Phan for their help earlier in my research career by sharing their knowledge of various techniques with me. I would next like to thank Mary Dickson, Kelsey Miller, Dr. Anthony Burke, and Dr. Nina Hüsken for helping me through the early stages of my involvement with the DNA/PTCDI work. I would like to thank Amir Mazaheripour for being a collaborator and guide as I continued with the PTCDI work. I would also like to thank the newer graduate students, Austin Wardrip and Andy Bartlett, for having worked with me these last few months and for continuing the project. I would like to thank the undergraduates that have contributed to supporting the project, including Katarina Van Wonterghem, Alex Schmidt, Kasha Muzila, Robert Lopez, Michelle Lu, and Linh Doan. I would like to thank Dr. Beniam Berhane and Dr. John Greaves for their insight and help with mass spectrometry. I would like to express many thanks to the very many collaborators that have played a role in advancing our work at the Gorodetsky Group.

I would like to thank my family for supporting me throughout school and helping me pursue my goals.

Portions of the thesis are adapted with permission from the American Chemical Society and the Gorodetsky Group.

I would lastly like to thank our funding sources since without them our work would not have been possible. In particular I would like to thank the University of California – Irvine, the Air Force Office of Scientific Research, the National Science Foundation, the Office of Naval Research, and the Naval Research Laboratory.

ABSTRACT OF THE THESIS

Synthesis and Purification of DNA-Like Nanowires: From Natural to Artificial

By

Jonah-Micah David Jocson

Master of Science in Materials Science and Engineering

University of California, Irvine, 2015

Professor Alon A. Gorodetsky, Chair

Carbon-based materials hold exciting prospects for the future of miniaturized electronics, potentially replacing silicon in next generation devices. However, a stronger fundamental understanding of the charge transport phenomena and structure-function relationships is necessary to effectively employ the favorable properties of these materials. To achieve this we sought to develop a precisely defined model system that emulates aromatic, π-stacked organic semiconductors. We first drew inspiration from the nucleobase stacking structure of deoxyribonucleic acid (DNA) in order to take advantage of well-established oligonucleotide synthesis and self-assembly methodologies. We demonstrated the exquisite control offered by these methodologies through implementation in a microfluidic-encapsulated, DNA-modified carbon nanotube field effect transistor (CNT FET) capable of highly sensitive and sequence specific detection of a prototypical DNA binding protein. We then expanded our studies to include perylene-3,4,9,10-tetracarboxylic diimides (PTCDIs), a well-known class of organic materials that have been incorporated within DNA as base surrogates but were generally unstudied in terms of assembly dynamics and kinetics. By examining molecular dynamics simulated and synthetic variants of DNA-PTCDI hybrid systems, we established a foundation for the rational design and construction of precisely defined one-dimensional organic nanowires. We

proceeded to prepare a novel class of chemically well-defined PTCDI-based organic semiconductor ensembles that could serve as a platform for investigating the emergent electronic phenomena in organic semiconductor materials. Altogether, our studies hold general relevance for fundamentally understanding structure-function relationships in arbitrary organic materials, nanoscale charge transfer phenomena at device-relevant organic/inorganic interfaces, and electrical conductivity in biological and bioinspired systems.

CHAPTER 1 Introduction

1.1 Motivation

Advances over the past few decades in carbon-based semiconducting materials have propelled organic electronics into the spotlight to potentially revolutionize the way our devices function.[1] With applications reaching from organic light emitting diodes (OLEDs)[2], to organic photovoltaics (OPVs)[3], to even organic field-effect transistors (OFETs)[4], the emergence of the organic electronics field seemingly opened up a new wealth of possibilities for what we can do with our technology. A major point of appeal with organic electronics is the huge diversity in both the types of organic semiconductor building blocks to choose from as well as the ways in which these building blocks can be assembled (Figure 1.1).[5] It is through this diversity that organic electronic materials hold a great deal of potential for customizability that can cater to a broad range of material property requirements.

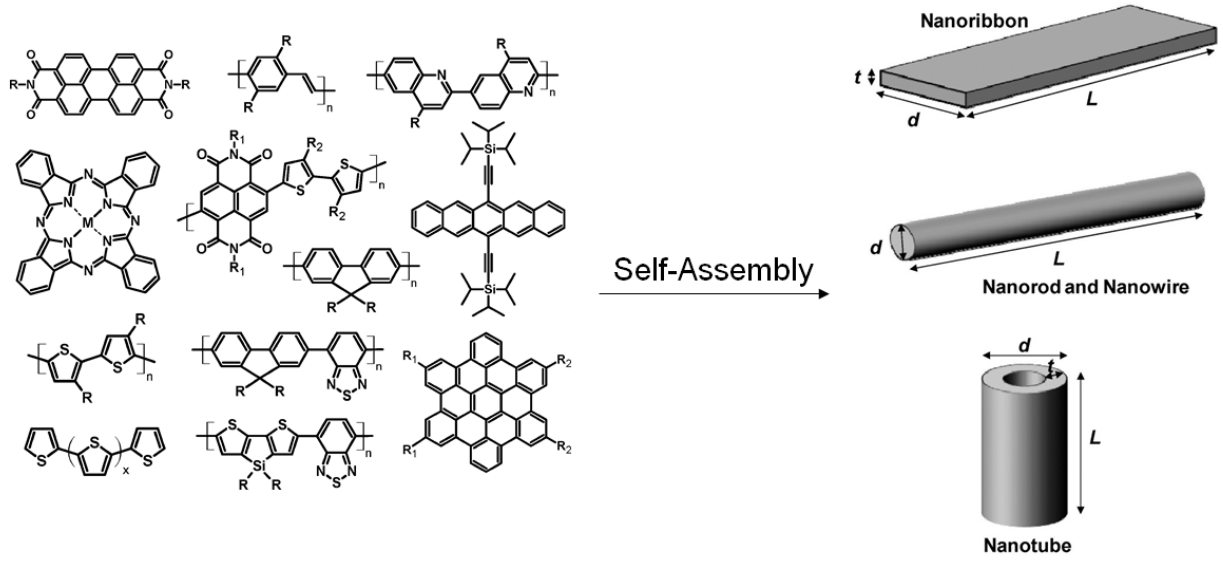

Figure 1.1: Molecular structures of representative organic semiconductors that can be assembled in various geometries and structures. The image has been adapted from reference 5.

Despite the progress over the years, widespread implementation of organic electronic based devices remains somewhat limited, with OLED displays being one of the only prominent applications present in the consumer market.[6] Although the ongoing advances in organic electronics grow more and more impressive, we are still seemingly distant from reaching the predicted revolutionary turning point in our practical technology. Poor control over assembly of organic electronic molecules has been a major hurdle, bringing issues of inadequately ordered patterns and inconsistent reproducibility[1] (Figure 1.2). Furthermore, in-depth analysis of the resulting organic semiconductor constructs can be difficult, requiring creative and novel analytical tools to truly probe the relationships between structure, chemical composition, and function.[1]

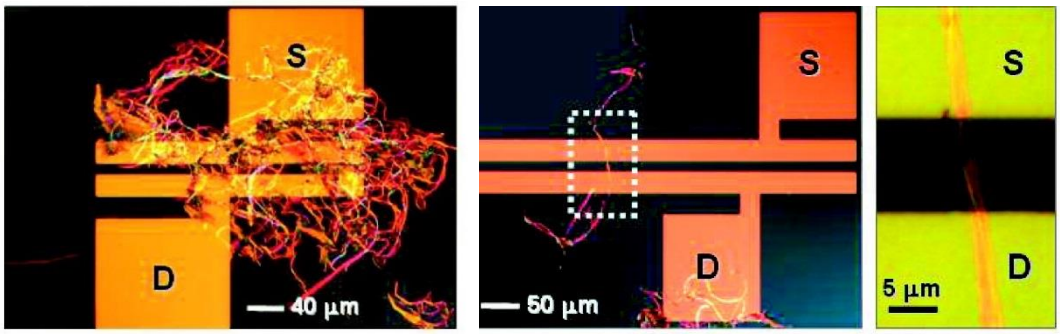

Figure 1.2: A typical strategy for investigating an organic electronic material involves bridging source-drain electrodes for electrical measurements. Common techniques used to cast the organic electronic materials directly onto the substrate can cause difficulties in controlling geometry, orientation, and arrangement. The image has been adapted from reference 7.

With 10 nm node devices already planned for mass production within the next year[8], 7 nm node test chips already being produced[9], and 5 nm to 1.8 nm node devices already present in industry roadmaps for the next decade[10], understanding the smaller length scales are of interest for organic electronic materials in order to maintain relevance relative to their inorganic

counterparts. In particular, the ~1 nm to ~5 nm length regime is important to understand. This size range encompasses several phenomena relevant to potential device functionality, including exciplex formation, electron transfer, Förster energy transfer, exciton Bohr radius, exciton diffusion length, and Debye screening length, among others (Figure 1.3).[11] This length scale presents additional complexity as it represents a key region in the evolution of electronic structure for organic semiconducting materials (Figure 1.4).[12] In the three size regimes outlined in Figure 1.4, the properties and behavior of organic semiconducting materials can be drastically different as you increase in size.[12] Since behavior at the single molecule level does not necessarily translate to the same behavior as you transition to a bulk material, designing devices that use organic semiconducting materials at this intermediate length scale is not only difficult to access synthetically, but also brings additional challenges due to difficulties in predicting functionality.

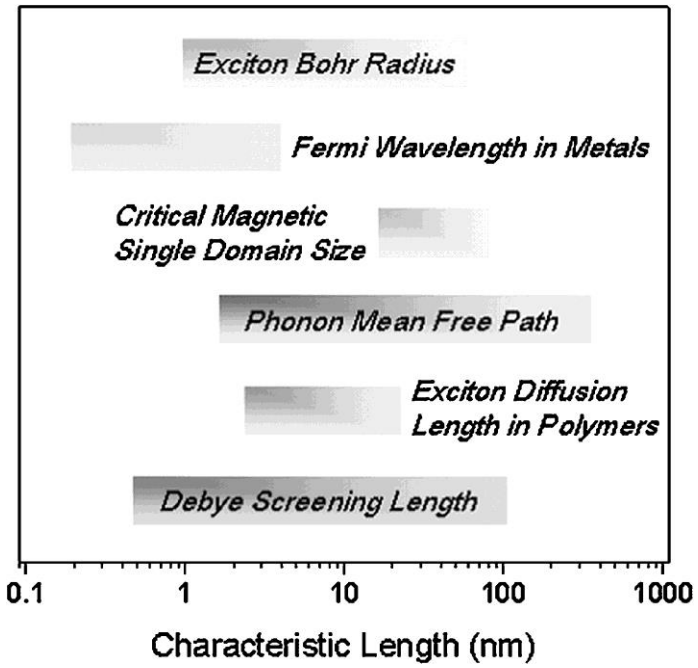

Figure 1.3: Characteristic length scales associated with various phenomena for semiconducting nanowires. The image has been adapted from reference 11.

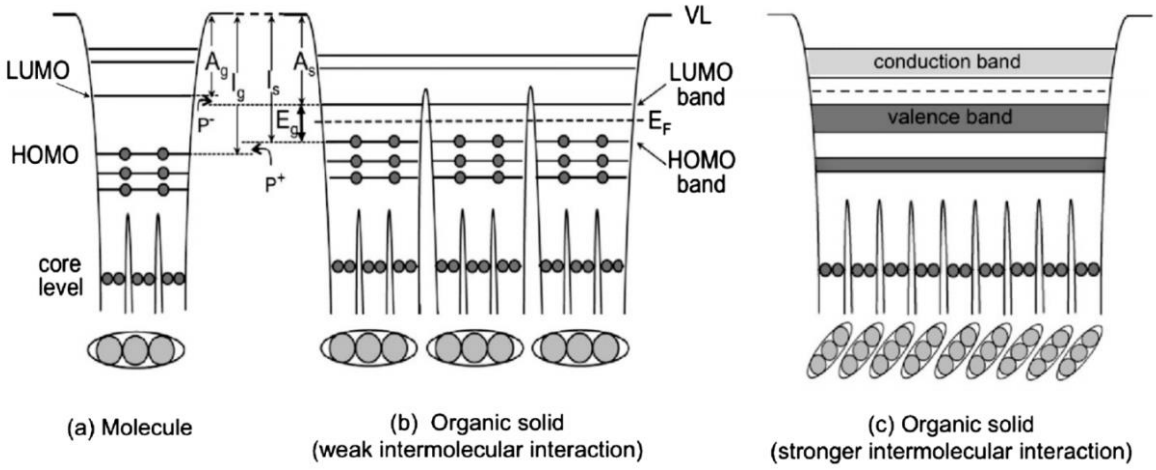

Figure 1.4: The evolution of electronic structure from a single organic molecule (A) to an organic solid (B and C). At the single molecule level (A), the HOMO and LUMO energy levels are well-defined. At the intermediate organic solid (B), there are multiple closely spaced energy levels. At the extended material level (C), the electronic structure takes a band-like characteristic. The image has been adapted from reference 12.

1.2 Inspiration from DNA

In order to gain access to this very specific size regime, we first look to DNA for inspiration. The DNA structure is essentially made up of a series of phosphate, sugar, and base units (Figure 1.5A) where the bases are planar molecules that stack along the helix axis (Figure 1.5B).[13, 14] However, another way to look at it is that it is a chemically and geometrically well-defined wire comprised of arbitrary organic building blocks. It is precisely this feature of DNA that we want to emulate in formulating a model system to study the fundamental charge transport phenomena and structure-function relationships found in organic electronic systems. Furthermore, not only can we draw from the structure of DNA, but also we can draw from the methodologies that have been developed to synthesize and study DNA.

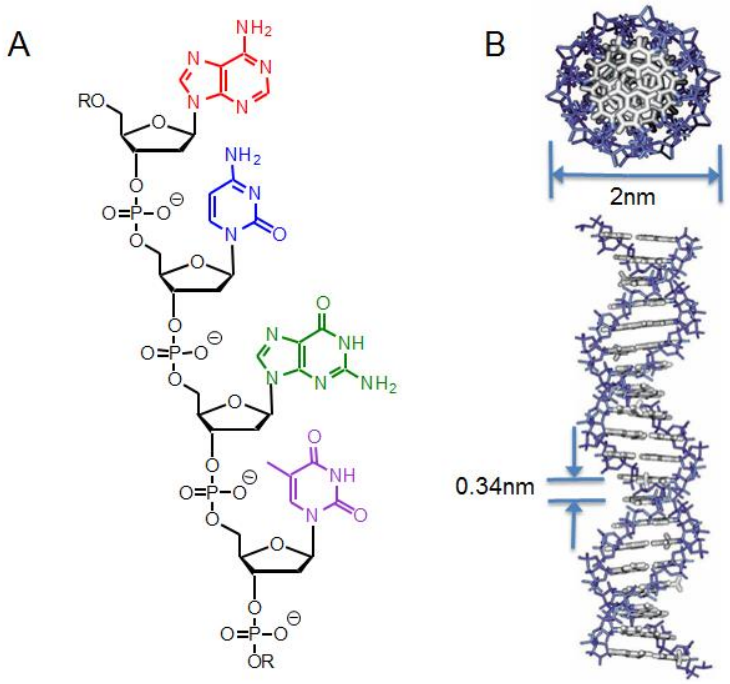

Figure 1.5: (A) DNA is comprised of a phosphate and sugar backbone holding together arbitrary combinations of guanine (red), cytosine (blue), adenine (green), and thymine (purple) bases. (B) The arrangement of the planar base pairs forms a one-dimensional π-stack down the center of the DNA. The image has been adapted from reference 14.

The well-established strategies for oligonucleotide synthesis provide a strong starting point for achieving our synthetic goals. One approach of particular interest is solid phase synthesis through the phosphoramidite method, which has been heavily developed to the point of automation (Scheme 1.1).[15] The first key component is a functionalized solid support, usually some type of controlled pore glass or resin (Figure 1.6A). The solid support features a dimethoxytrityl (DMT) protected hydroxyl group at the 5' end which can be deprotected to initiate the synthesis cycle. The next key component is the nucleoside phosphoramidite (Figure 1.6B) which includes the next desired base, a diisopropylamino group, a DMT protected hydroxyl group, and a 2-cyanoethyl protecting group. Introducing a mixture of the nucleoside phosphoramidite and a tetrazole activator to the deprotected solid support initiates the coupling step, yielding a support-bound phospite triester.[17] Next, a capping step is used to block any

remaining unreacted 5' hydroxyl groups. Lastly, an oxidation step converts the phosphite triester from the coupling step into a phosphotriester, with this resulting structure essentially being like the phosphate unit you would find in the DNA backbone but with a 2-cyanoethyl protecting group.[17] At this point the new DMT group on the new 5' hydroxyl end can be deprotected to restart the cycle and the next desired nucleoside base can be coupled. Alternatively, the cycle can be terminated and the synthesized oligonucleotide can be cleaved from the solid support with concentrated ammonium hydroxide. Subsequent heating of this mixture serves to remove any remaining protecting groups on the bases or phosphates. After evaporation of the aqueous solution, the oligonucleotide is ready to be purified, typically by high performance liquid chromatography (HPLC).

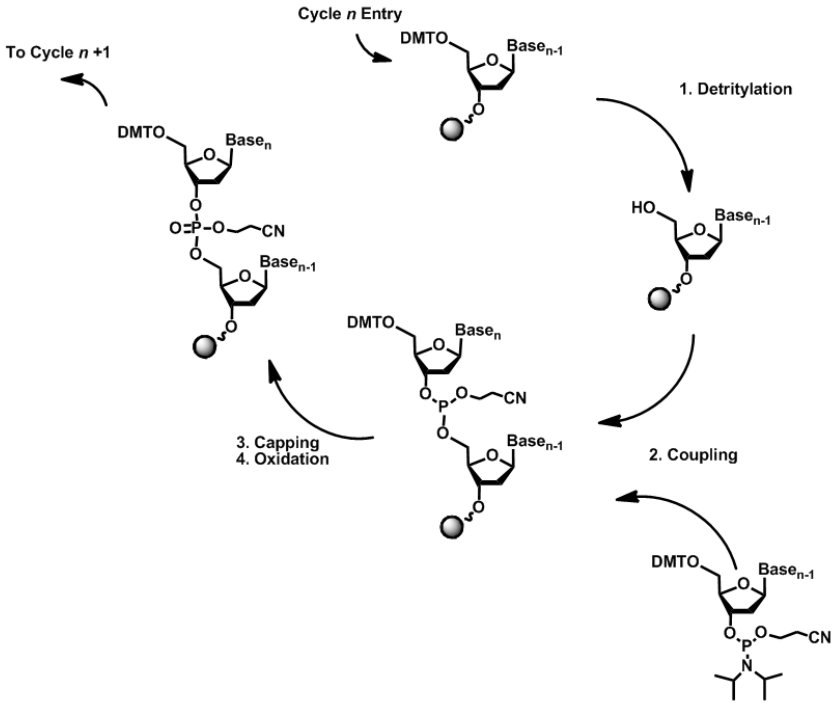

Scheme 1.1: Solid phase synthesis through the phosphoramidite method is a common automated technique used for synthesizing oligonucleotides. The cycle begins by detritylation (1) of a DMT protected oligonucleotide precursor then continues to coupling of the next nucleoside base (2), capping (3), and oxidation (4). After the oxidation step the cycle can either be terminated to move forward or repeated to add another nucleoside base.

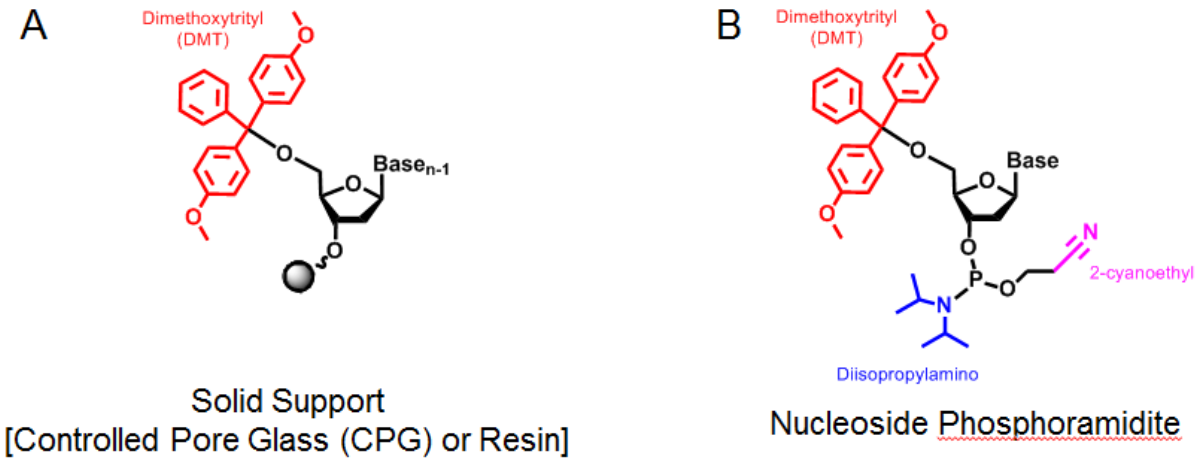

Figure 1.6: Some key components to solid phase synthesis through the phosphoramidite are the solid support (A) and the nucleoside phosphoramidites (B) that will be coupled to yield the desired oligonucleotide. The image has been adapted from reference 16.

In addition to the synthetic control offered by oligonucleotide chemistry, charge transport through DNA has been extensively measured using a variety of techniques.[18] These include photophysical studies, bridging of a carbon nanotube gap in a field effect transistor, break junction measurements, electrochemical measurements, and conducting atomic force microscopy (AFM) interrogation, to name a few (Figure 1.7).[18] If DNA and DNA-like structures are synthesized, the full array of DNA charge transport interrogation techniques would presumably be available as analytical tools to study the structure. With these DNA related methodologies to build from, we can effectively formulate a strategy on how to address the issues of poor synthetic control and limited analytical tools that have hindered the systematic study of charge transport phenomena and structure-function relationships in organic electronic materials.

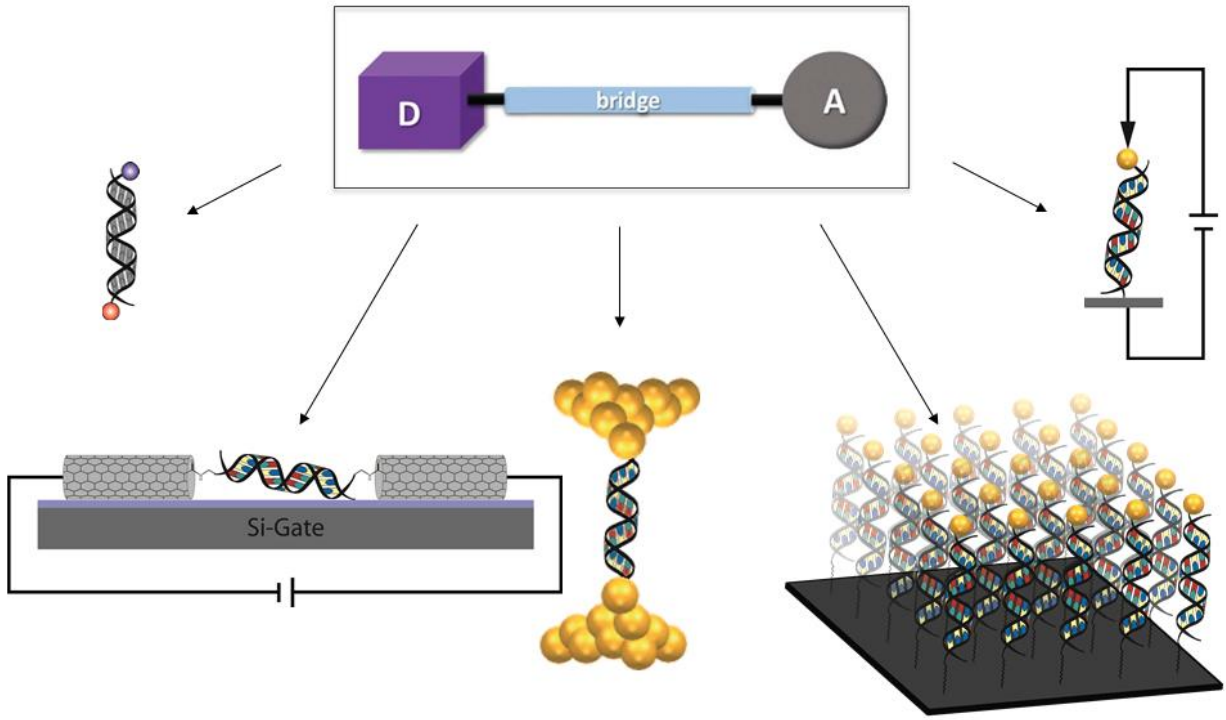

Figure 1.7: Charge transport in DNA has been measured using a variety of techniques that follow a donor-bridge-acceptor model. From left to right: DNA duplex with a donor and acceptor with charge transport promoted by photoactivation; DNA molecule bridging a carbon nanotube gap; break junction measurement of DNA; electrochemical device with a DNA modified electrode; conducting AFM tip on a gold nanoparticle attached to DNA. The image has been adapted from references 18 and 19.

1.3 Structure of Thesis

This thesis aims to outline the development of a novel strategy to systematically study the charge transport phenomena and emergent structure-function relationships in organic electronic materials. The strategy draws inspiration from the structure, synthesis, and study of DNA. We begin in Chapter 2 by demonstrating the level of control offered by DNA synthesis and analysis techniques. We precisely synthesize a specific nucleotide sequence that features the recognition site of a DNA-binding enzyme. We modify this DNA with a linker, allowing for predictable self-assembly onto a carbon nanotube field effect transistor (CNT FET) device. Lastly, we demonstrate electrical monitoring at these CNT FET devices, successfully showing high sensitivity to the DNA and enzyme interaction. In Chapter 3 we begin to look at perylene-

3,4,9,10-tetracarboxylic diimide (PTCDI), an organic semiconducting building block that we can incorporate into DNA. We used one, two, and three PTCDI building block systems to study PTCDI assembly dynamics and kinetics. We showcase both the ability to synthesize perylene-DNA hybrid systems as well as a novel computational framework to study these systems. In Chapter 4 we build upon the previous work by constructing a DNA-inspired organic semiconductor model system that allows us to probe the evolution in electronic structure with increasing number of PTCDI building blocks. Here, we show that our novel model system could hold relevance for understanding structure-function relationships in arbitrary organic electronic materials, nanoscale charge transfer phenomena at device-relevant organic/inorganic interfaces, and electrical conductivity in biological and bioinspired systems. In Chapter 5 a brief summary of the thesis is provided followed by potential future directions for the project.

1.4 References

1. Zhang, X.; Bäuerle, P.; Aida, T.; Skabara, P.; Kagan, C. *Organic Electronics for a Better Tomorrow: Innovation, Accessibility, Sustainability*; Chemical Science and Society Summit: San Francisco, California, **2012**.
2. Tang, C. W.; VanSlyke, S. A. *Appl. Phys. Lett.* **1987,** 51, 913-915.
3. Tang, C. W. *Appl. Phys. Lett.* **1986,** 48, 183-185.
4. Koezuka, H.; Tsumura, A.; Ando, T. *Synt. Met.* **1987,** 18, 699-704.
5. Kim, F. S.; Ren, G.; Jenekhe, S. A. *Chem. Mater.* **2011,** 23, 682-732.
6. Singh, R. *World Organic Electronics Market – Opportunities and Forecasts, 2013-2020*; Allied Market Research, **2020**.
7. Briseno, A. L. *et al.*, *Chem. Mater.* **2008**, 20, 4712-4719.
8. Low, K. Samsung Semiconductors. 10nm FinFET Added to Samsung Foundry's Process Roadmap. http://www.samsung.com/semiconductor/insights/article/21447 (Aug. 16, **2015**).
9. Vu, C. IBM. IBM Research Alliance Produces Industry's First 7nm Node Test Chips. http://www-03.ibm.com/press/us/en/pressrelease/47301.wss (Jul. 09, **2015).**
10. *International Technology Roadmap for Semiconductors 2013 Edition Executive Summary*. ITRS, **2013.**
11. Law, M.; Goldberger, J.; Yang, P. *Annu. Rev. Mater. Res.* **2004**, 34, 83-122.
12. Brütting, W.; Adachi, C. Eds. *Physics of Organic Semiconductors*, 2nd ed.; Wiley-VCH: Weinheim, Germany, **2012**.
13. Eley, D. D.; Spivey, D. I. *Trans. Faraday Soc.* **1962**, 58, 411-415.
14. Genereux, J. C.; Barton, J. K. *Chem Rev.* **2010**, 110, 1642-1662.
15. Beaucage, S. L.; Iyer, R. P. *Tetrahedron*. **1992**, 48, 2223-2311.
16. *Chemical Synthesis and Purification of Oligonucleotides*. Integrated DNA Technologies, **2011.**
17. Brown, T.; Brown Jr., T. Solid-Phase Oligonucleotide Synthesis. *Nucleic Acids Book*. ATDBio, **2005.**
18. Genereux, J. C.; Barton, J. K. *Nat. Chem.* **2009**, 1, 106-107.
19. Schubert, C.; Margraf, J. T.; Clark, T.; Guldi, D. M. *Chem. Soc. Rev.* **2015**, 988-998.

CHAPTER 2 Sequence Specific Detection of Restriction Enzymes at DNA-Modified Carbon Nanotube Field Effect Transistors

2.1 Abstract

Protein–DNA interactions play a central role in many cellular processes, and their misregulation has been implicated in a number of human diseases. Thus, there is a pressing need for the development of analytical strategies for interrogating the binding of proteins to DNA. Herein, we report the electrical monitoring of a prototypical DNA-binding protein, the PvuII restriction enzyme, at microfluidic-encapsulated, DNA-modified carbon nanotube field effect transistors. Our integrated platform enables the sensitive, sequence specific detection of PvuII at concentrations as low as 0.5 pM in a volume of 0.025 μL (corresponding to ~7500 proteins). These figures of merit compare favorably to state of the art values reported for alternative fluorescent and electrical assays. The overall detection strategy represents a step toward the massively parallel electrical monitoring, identification, and quantification of protein–DNA interactions at arrayed nanoscale devices.

2.2 Introduction

Protein–DNA interactions play a crucial role in the regulation of many cellular processes, including transcription, methylation, replication, recombination, and repair.[1-10] For example, DNA-binding proteins known as transcription factors control the flow of information from DNA to mRNA. These proteins are essential for numerous cellular functions, such as signaling, development, response to environmental stimuli, and apoptosis.[1-10] It is therefore not surprising that the misregulation of DNA-binding proteins has been linked to a wide range of human genetic diseases.[11-13] Consequently, a number of analytical techniques, including chromatin immunoprecipitation, electrophoretic mobility shift, DNA pull-down, microplate capture, and

fluorescent reporter assays, have been developed specifically for monitoring protein–DNA interactions.[2-10] The insight afforded by such techniques has led to not only a better understanding of cellular processes but also to improved point of care diagnostics.[2-10]

In recent years, electrical assays have emerged as attractive alternatives for monitoring the binding of proteins to DNA.[14-20] Electrical methodologies possess several inherent advantages, which include minimal perturbation of the target analyte, no requirement for labeling, rapid real-time kinetic analysis, and ease of multiplexing.[14-20] Moreover, electrical schemes are typically inexpensive and user-friendly due to small sample volumes, minimal processing and preparation of analytes, and simple data acquisition and interpretation techniques.[14-20] Consequently, electrical assays for the monitoring, identification, and quantification of protein–DNA interactions constitute important and promising targets for further research and development.

Carbon nanotube field effect transistors (CNT FETs) have shown particular promise for the high throughput electrical monitoring of protein–DNA interactions. CNT FETs are inherently size compatible with biomolecules, are straightforward to modify with analyte recognition elements, feature well-understood signal transduction/sensing mechanisms, and display excellent sensitivity and selectivity.[21-26] These advantages have made CNT FETs a popular option for a variety of bioanalytical applications, such as the detection of DNA hybridization in genomics assays.[21-26] However, despite the vast literature on CNT FET-based biosensors,[21-26] there have been relatively few reports of the electrical detection of DNA-binding proteins at individual CNT FETs, likely due to difficulties often associated with fabrication of the requisite DNA-modified devices.[27-29]

Herein, we describe an integrated CNT FET-based platform for the electrical interrogation of protein–DNA interactions. We first employ reliable lithographic protocols to fabricate arrayed, microfluidic-encapsulated CNT FETs. We next use a robust and high yield noncovalent approach to self-assemble sparse DNA monolayers at the CNT FETs. The resulting devices facilitate the sequence specific detection of picomolar concentrations of prototypical DNA-binding proteins (restriction enzymes) in small volumes. In their totality, our findings constitute an important step toward the massively parallel electrical monitoring of arbitrary DNA-binding proteins on a single substrate.

2.3 Experimental Section

2.3.1 Synthesis of Oligonucleotides

All oligonucleotides were synthesized according to established phosphoramidite-based protocols on an Applied Biosystems 394 DNA Synthesizer.[30-34] The phosphoramidites required for synthesis of the naturally occurring DNA bases were purchased from commercial sources (Azco Biotech, Inc.). The unnatural pyrene phosphoramidites required for the preparation of pyrene-modified DNA were synthesized according to previously reported procedures.[31]

2.3.2 Purification of Oligonucleotides

The oligonucleotides were purified using high performance liquid chromatography (HPLC) on an Agilent 1260 Infinity system with an Agilent reverse phase C18 column. They were eluted with a gradient evolved from 95% solvent A and 5% solvent B to 0% solvent A and 100% solvent B over 30 min at a flow rate of 1 mL/min (solvent A, 50 mM ammonium acetate, pH = 6 buffer; solvent B, acetonitrile). A typical HPLC chromatogram for pyrene-modified DNA

is shown in Figure S2.1. The pure oligonucleotides were desalted by ethanol precipitation and dried on a vacuum concentrator prior to subsequent characterization.

2.3.3 Characterization of Oligonucleotides

The identity of the oligonucleotides was confirmed with UV–visible spectroscopy and matrix assisted laser desorption/ionization time-of-flight (MALDI-TOF) mass spectrometry. The UV–visible measurements were performed on either a Cary 50 UV−vis spectrophotometer or a Shimadzu UV-2450 spectrophotometer, and a typical corresponding absorbance spectrum for a pyrene-modified oligonucleotide is shown in Figure S2.2. The mass spectrometry measurements were performed on an Applied Biosystems Sciex MALDI-TOF/TOF instrument, and a typical corresponding spectrum for a pyrene-modified oligonucleotide is shown in Figure S2.3.

2.3.4 Preparation of Duplex DNA

Duplex DNA was prepared by combining equimolar solutions of a pyrene-modified oligonucleotide with its complementary strand in Pierce PBS (0.1 M sodium phosphate, 0.15 M sodium chloride, pH = 7.2). The formation of duplexes was ensured by thermal annealing at 90°C, followed by slow cooling to room temperature.

2.3.5 Preparation of Silicon Substrates

The substrates required for device fabrication were cut from 4 in. silicon wafers with a 3000 Å oxide layer on both sides (International Wafer Service, Inc.). The wafers were sectioned into 2.25 cm^2 chips, which were cleaned with pirahna solution (1:3 hydrogen peroxide to sulfuric acid). The through-substrate microfluidic inlet/outlet channels were fabricated via standard

photolithographic techniques. In brief, the substrate was coated with Microposit S1813 Photoresist (Shipley, Inc.), with the desired through-hole pattern defined by UV irradiation through a photomask. After resist liftoff, the oxide was removed with Buffered Oxide Etch, 5:1 (J.T. Baker), and the through-substrate channels were defined with PSE-300F Preferential Silicon Etchant (Transene, Inc.). The resulting patterned substrates are shown in Figure S2.4.

2.3.6 Growth of Aligned Carbon Nanotubes

A sparse array of aligned single walled carbon nanotubes was grown on the surface of each patterned substrate via chemical vapor deposition (CVD).[28-29] In brief, an Fe–Co catalyst was synthesized according to established techniques[35] and applied to the patterned substrates. The substrates were placed in a home-built quartz tube carbon nanotube growth furnace and subjected to a continuous flow of an Ar/H_2 gas mixture while the temperature was gradually increased. Shortly before reaching a temperature of 890 °C, ethanol vapor was slowly introduced into the furnace by an Ar/H_2 carrier gas mixture. The carbon nanotubes were grown on the substrates via CVD under a stable laminar flow over a period of approximately an hour. Finally, the nanotube-covered substrates were brought to room temperature and removed from the furnace. The aligned carbon nanotubes are shown in Figure S2.4.

2.3.7 Fabrication of Electrical Contacts

Electrical contacts were fabricated via electron beam physical vapor deposition on a Temescal CV-8 evaporator. Shadow masks defining arrays of paired electrodes were first affixed onto the nanotube-covered substrates. A 4 nm chromium adhesion layer and a 40 nm gold layer

were then sequentially deposited through the shadow mask directly onto the carbon nanotubes. The electrode arrays are shown in Figure S2.4.

2.3.8 Fabrication of Microfluidic Components

The PDMS components required for the front and back side of the microfluidic housing were prepared according to known commercial procedures. In brief, master templates featuring the desired microfluidic patterns were fabricated by patterning wafers coated with SU-8 photoresist (Microchem, Inc.) through a chrome photomask. The SU-8 was then baked, developed, and cured according to the manufacturer's protocols. A degassed 10:1 silicone elastomer to curing agent solution (Dow Corning, Inc.) was poured over the templates, allowed to settle for 12 hours, and cured at 65 °C. The PDMS was sectioned into individual stamps and peeled off from the templates. The front and back side microfluidic housing components are shown in Figure S2.4.

2.3.9 Integration of the Microfluidic Housing

The device-covered substrates were encapsulated within the PDMS microfluidic housing. The front and back side PDMS stamps were pretreated with UV-ozone in a model 42 UVO-Cleaner (Jelight, Inc.) to improve their adhesive properties. The PDMS components were then directly bonded to the silicon substrates. The attached housing is shown in Figure S2.4.

2.3.10 Integration of Fluid Flow Tubing

The microfluidic-encapsulated substrates were integrated with fluid flow tubing. First, gold capillaries were inserted into each microfluidic channel on the back side PDMS stamp.

Next, the capillary tubing was sheathed with silicone tubing (VWR International, Inc.). The tubing was secured in place with epoxy to prevent leakage of the injected solutions.

2.3.11 Self-Assembly of DNA Monolayers

Pyrene-modified DNA duplexes were self-assembled at the graphitic sidewalls of carbon nanotubes according to established procedures.[30-34] In brief, the devices were incubated with 5 μM duplex DNA solutions in Pierce PBS (0.1 M sodium phosphate, 0.15 M sodium chloride, pH = 7.2) overnight at 4 °C. After DNA incubation, the carbon nanotubes were rinsed repeatedly by flowing fresh buffer containing no DNA over their surfaces. The transistors were electrically characterized before and after DNA modification in order to confirm successful self-assembly.

2.3.12 Physical Characterization

Throughout the fabrication process, the carbon nanotube field effect transistors and various microfluidic housing components were characterized with optical microscopy, scanning electron microscopy (SEM), and atomic force microscopy (AFM) as necessary. The optical images were obtained on an Axio Imager A1M Microscope (Carl Zeiss, Inc.) outfitted with an Epiplan 20× lens (NA = 0.4) and processed with the manufacturer's AxioVision AC4.5 software. The scanning electron microscopy images were obtained on a Hitachi S-4700 SEM. The atomic force microscopy images were obtained on an Asylum Research MFP-3D AFM and analyzed with the MFP3D software package.

2.3.13 Electrical Characterization of Carbon Nanotube Field Effect Transistors

The transistors were electrically characterized with a PM-5 Probe Station (Cascade Microtech, Inc.) outfitted with a 4156C Semiconductor Parameter Analyzer (Agilent, Inc.). The devices were first characterized in ambient conditions with standard back gating and sorted according to their electrical characteristics. For simplicity, only nanotubes displaying small-bandgap semiconducting behavior were used for the experiments reported here. All measurements in solution employed direct electrolytic gating via the solution-exposed sections of the silicon substrate.[36, 37]

2.3.14 Control of Fluid Flow

The injection of aqueous solutions was controlled with a manually programmable KDS 210 syringe pump (KD Scientific, Inc.). Unless specified otherwise, all experiments were performed in aqueous buffer, either with no flow or at a constant flow rate of 0.01 mL/h.

2.3.15 Electrical Monitoring of Restriction Enzyme Activity

The PvuII restriction enzyme (New England Biolabs, Inc.) was used as the detection target. In a typical experiment, the initial electrical characteristics of either a DNA-modified or a bare carbon nanotube field effect transistor were recorded in NEBuffer 4 (50 mM potassium acetate, 20 mM tris-acetate, 10 mM magnesium acetate, 1 mM DTT, pH = 7.9) (New England Biolabs, Inc.). Subsequently, a solution of PvuII in the same buffer was injected into the channel containing the DNA-modified or unmodified CNT-FET device, with the electrical characteristics recorded again. The measurements obtained in the absence and the presence of the enzyme were then compared as described below.

2.4 Results and Discussion

2.4.1 Design and Fabrication of a Microfluidic-Encapsulated Carbon Nanotube Field Effect Transistor Platform

For our electrical measurements, we designed and fabricated the integrated microfluidic-encapsulated platform shown in Figure 2.1. After cutting and cleaning the substrates, we etched through-substrate inlet/outlet channels for fluid flow within the silicon dioxide/silicon/silicon dioxide substrates. We then grew a sparse array of aligned single walled carbon nanotubes on the substrates via chemical vapor deposition. We in turn deposited paired gold electrodes onto the carbon nanotubes through a shadow mask, yielding an array of CNT FETs. The substrates were encapsulated in a microfluidic housing by lamination of prepatterned PDMS stamps onto both their front and back sides, with the through-substrate inlet/outlet channels connecting the two stamps. The back side PDMS stamp featured connections for the injection of biological solutions and channels for distribution of these solutions to and from the substrate. The front side PDMS stamp featured channels for fluid flow and square holes over the electrodes for making electrical contacts to the CNT FETs. Finally, fluid flow tubing was integrated with the PDMS stamps in order to interface the housing with a standard syringe pump and enable injection of aqueous solutions. The resulting devices, as illustrated in Figure 2.2, were individually electrically characterized prior to subsequent protein detection experiments.

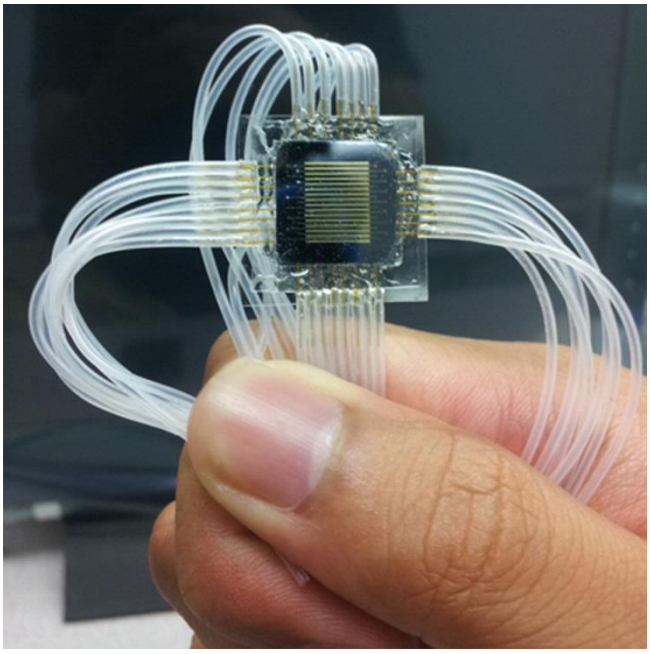

Figure 2.1: Picture of a completed hand-held chip, which has been integrated within a microfluidic housing and modified with fluid flow tubing.

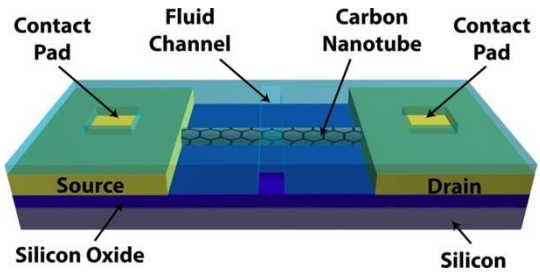

Figure 2.2: Illustration of a single microfluidic-encapsulated carbon nanotube field effect transistor. The device consists of a carbon nanotube contacted by source and drain electrodes separated by 50 μm. The aligned housing ensures that fluid flows over the device through a microfluidic channel that runs perpendicular to the carbon nanotube. The access holes in the microfluidic housing above the gold pads enable electrical interrogation of the individual transistor.

Here, it is important to note that the design of our microfluidic housing specifically incorporated several important advantages relevant for biological sensing. The housing featured a high degree of redundancy with 15 distinct microfluidic channels, each containing up to 50 functional CNT FETs. These devices could be electrically interrogated either individually or

simultaneously via a global electrolytic gate.[36-37] The independently addressable microfluidic channels enabled self-assembly of multiple distinct DNA sequences on a single substrate, facilitating direct comparison of experiments. In addition, the front side PDMS stamp protected the carbon nanotube/metal contacts from the buffer solutions, eliminating the possibility of artifacts associated with nonspecific adsorption at the electrodes.[38-40] These features all helped to ensure robust and reliable DNA self-assembly and protein detection experiments.

2.4.2 Self-Assembly of Duplex DNA at Carbon Nanotube Field Effect Transistors

We adapted well-known literature protocols for the noncovalent self-assembly of duplex DNA at our CNT FETs.[30-34, 41-44] Thus, we used our microfluidic housing to introduce DNA duplexes featuring a pyrene moiety at one terminus to pristine devices (Figure 2.3A). The duplex DNA was then allowed to assemble at the graphitic CNTs, with the pyrene serving as a noncovalent anchor (Figure 2.3 A).[41-44] Importantly, this approach avoided interruption of the conjugation of the CNT sidewalls, thereby preserving the electrical properties of our devices.[41-44] To leave room for protein binding during subsequent experiments, we employed a self-assembly buffer containing monovalent rather than multivalent cations, ensuring sparse DNA coverage (due to electrostatic repulsion among the DNA duplexes).[30, 32, 45-47] The overall modification strategy was facile and proceeded in high yield, as previously reported.[30-34, 41-44]

Figure 2.3B illustrates the electrical characteristics (current as a function of gate voltage at a constant source-drain bias) for a typical CNT FET before and after DNA self-assembly. The unmodified CNT FET displayed electrical characteristics typical for a small-bandgap semiconducting nanotube.[48] After modification with DNA, the minimum conductivity point shifted toward more positive gate biases by 0.15 (±0.05) V. This shift was presumably due to the

negative charge of the DNA backbone, which acted like a p-type dopant.[40, 49-53] Our observations qualitatively indicated that the device response was primarily governed by electrostatic effects associated with a change in the nanotube's surface charge density upon DNA adsorption.[40, 49-53]

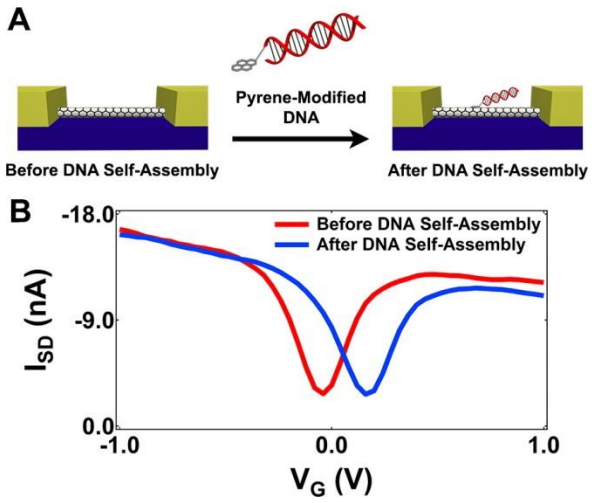

Figure 2.3: (A) Illustration of the self-assembly of pyrene-modified duplex DNA at a carbon nanotube field effect transistor. The pyrene group acts as an anchor, facilitating attachment of the DNA to the carbon nanotube sidewalls via noncovalent π-stacking interactions. (B) Comparison of the current versus voltage electrical characteristics of a carbon nanotube field effect transistor before (red) and after (blue) self-assembly of DNA. Note the shift of the curve toward more positive biases after DNA self-assembly, presumably due to the negative charge of the DNA backbone. The DNA sequence was pyrene-$(CH_2)_4$-P_i-5′-TGCGTCT*CAGCTG*AAGTCAC-3′ plus complement, where the PvuII restriction site is italicized. The experiment was performed in 0.1 M sodium phosphate, 0.15 M sodium chloride, pH = 7.2 buffer.

To gain insight into the orientation of the DNA at the CNT sidewalls, we examined our devices before and after DNA self-assembly with atomic force microscopy (Figure S2.5). Before DNA self-assembly, a typical CNT featured an average height of ~2.9 nm (Figure S2.5). However, after DNA self-assembly, the same CNT featured an average height of ~4.3 nm, corresponding to an increase of ~1.4 nm (Figure S2.5). This shallow height increase indicated that our DNA duplexes likely adopted a small angle with respect to the nanotube surface, leaving the anionic DNA backbone in close proximity to the nanotube, as previously postulated for

similar systems.[52] This orientation ensured that the DNA had a large effect on the electrical characteristics of our devices even at high electrolyte concentrations.

As a consistency check, we calculated the change in the minimum conductivity point (or threshold voltage) that would be expected after DNA modification. Thus, we applied a simple model developed by Artyukhin et al., which relates the threshold voltage shift (ΔV) and the change in the surface charge density ($\Delta\sigma_s$) via the equation $\Delta V = (\Delta\sigma_s\lambda_d)/(\varepsilon_w\varepsilon_0)$, where λ_d is Debye length, ε_w is the dielectric constant of water, and ε_0 is the permittivity of free space.[50-51] Assuming a likely sparse DNA density of 10 pmol/cm^2 (with a corresponding $\Delta\sigma_s$ of ~38.5 μC/cm^2)[30-34] and estimating a Debye length λ_d of ~0.5 nm for our self-assembly buffer, we calculated a threshold voltage shift of $\Delta V \approx 0.13$ V. The magnitude and direction of the shift were in reasonable agreement with our experimental observations.

We performed several experiments to gain additional insight into the observed device response. CNT FETs incubated with DNA lacking a pyrene anchor revealed a small off-state shift of −0.01 (±0.03) V because the DNA did not attach itself to the nanotube sidewalls (Figure S2.6). CNT FETs incubated with 1-pyrenebutanol also revealed a small off-state shift of −0.01 (±0.05) V due to the nonperturbative nature of pyrene's interaction with the nanotube sidewalls (Figure S2.7). In addition, attempts to modify CNT FETs with single-stranded DNA resulted in irreproducible changes in the device characteristics (data not shown). In their totality, the above observations were fully consistent with the self-assembly of pyrene-modified duplex DNA at our CNTs.

2.4.3 Electrical Monitoring of Restriction Enzyme Activity at Carbon Nanotube Field Effect Transistors

Having demonstrated the self-assembly of DNA at our CNT FETs, we used these devices for the detection of the sequence specific activity of the PvuII restriction endonuclease (Figure 2.4A). We specifically selected PvuII as a model DNA-binding enzyme for our studies because of its well-known crystal structure, thoroughly explored biochemical properties, and high binding affinity for its 5′-CAGCTG-3′ recognition site.[54-58] Figure 2.4B illustrates current–voltage characteristics for a typical CNT FET modified with DNA containing the 5′-CAGCTG-3′ restriction site in the presence and absence of a 0.5 pM concentration of PvuII. In the presence of PvuII, the minimum conductivity point of the CNT FET shifted by −0.14 (±0.03) V (in the opposite direction of the shift during DNA modification), presumably due to a reduction in the DNA surface charge density.[40, 49-53] We observed nearly identical changes in our device characteristics at higher PvuII concentrations but no changes in our device characteristics at lower PvuII concentrations, indicating a detection limit of 0.5 pM for our system. Our findings were consistent with enzymatic cleavage of the nanotube-bound DNA, corresponding to a change in the amount of negative charge and, thus, the degree of doping for the DNA-modified nanotube.[40, 49-53]

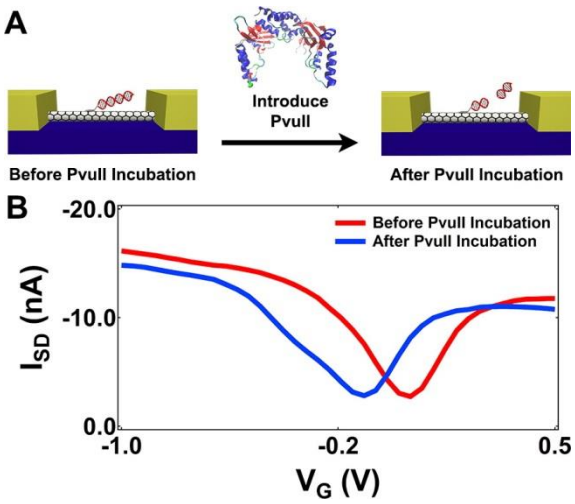

Figure 2.4: (A) Illustration of the activity of the PvuII restriction enzyme at the surface of a DNA-modified carbon nanotube field effect transistor, where the enzyme cuts the nanotube-bound DNA. (B) A comparison of the current versus voltage electrical characteristics of a carbon nanotube field effect transistor before (red) and after (blue) incubation with PvuII. Note the shift of the curve toward more negative biases after the DNA is cut, presumably due to a reduction in the amount of negative charge at the nanotube surface. The DNA sequence was pyrene-$(CH_2)_4$-P_i-5′-TGCGTCT*CAGCTG*AAGTCAC-3′ plus complement, where the PvuII restriction site is italicized. The experiment was performed in 50 mM potassium acetate, 20 mM tris-acetate, 10 mM magnesium acetate, 1 mM DTT, pH = 7.9 buffer at an enzyme concentration of 0.5 pM.

We next calculated the change in the minimum conductivity point due to restriction of the nanotube-bound DNA by again applying the model of Artyukhin et al.[50, 51] The duplexes were cut in the middle by PvuII, leading to a change in the DNA surface charge density of 19.5 μC/cm^2. Therefore, on the basis of this charge density change and a Debye length λ_d of ∼1.0 nm for our restriction buffer, we obtained a threshold voltage shift of $\Delta V \approx -0.13$ V. The magnitude and direction of the shift were again fully consistent with our experimental observations.

We performed several control experiments to demonstrate the highly specific electrical detection of PvuII activity. First, we modified CNT FETs with duplex DNA lacking the PvuII recognition site and exposed these devices to the restriction enzyme. We observed a small threshold voltage of −0.03 (±0.02) V consistent with some star activity by the enzyme (Figure 2.5 and Figure S2.8).[54-58] Second, we incubated CNT FET devices lacking a DNA monolayer with PvuII. We found a small threshold voltage of 0.04 (±0.04) V, indicating some nonspecific

adsorption of the net positively charged enzyme at the CNT FET (Figure 2.5 and Figure S2.9). Third, we incubated DNA-modified CNT FETs with bovine serum albumin (BSA), a protein that does not bind DNA. The presence of this enzyme had little effect on the device characteristics, in excellent agreement with previous findings (Figure S2.10).[38, 59] Taken together, these observations conclusively supported the fully electrical detection of sequence specific PvuII restriction activity at our DNA-modified devices.

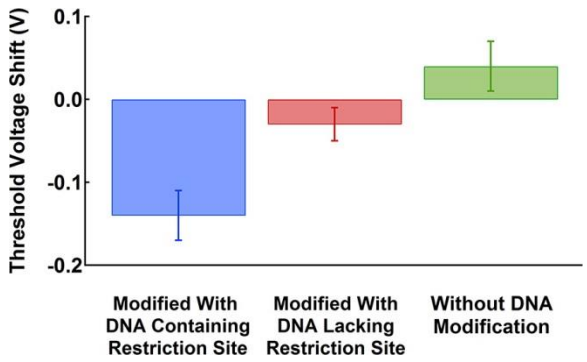

Figure 2.5: Illustration of the threshold voltage shift observed for carbon nanotube field effect transistors in the presence of PvuII with or without DNA modification. For a device modified with DNA containing the PvuII binding site, a shift of −0.14 V is observed in the presence of the PvuII restriction enzyme (blue bar). For a device modified with DNA lacking the PvuII binding site, a shift of −0.03 V is observed in the presence of PvuII (red bar). For a device that is not modified with DNA, a shift of 0.04 V is observed in the presence of PvuII (green bar). The experiments were performed in 50 mM potassium acetate, 20 mM tris-acetate, 10 mM magnesium acetate, 1 mM DTT, pH = 7.9 buffer at an enzyme concentration of 0.5 pM. The errors bars correspond to the standard deviation obtained for a minimum of three measurements.

2.5 Conclusion

We have demonstrated the electrical monitoring of protein–DNA interactions at DNA-modified CNT FETs. Our approach relies upon robust and reliable lithographic fabrication and biomolecular self-assembly protocols for the preparation of arrays of microfluidic-encapsulated, DNA-modified devices on a single substrate. Here, the CNT-confined DNA probe molecules function as exquisitely sensitive recognition elements for the transduction of biochemical events

into electrical signals, thereby providing direct information on the sequence specific activity of a prototypical DNA-binding protein (the PvuII restriction endonuclease). The signal transduction mechanism takes advantage of the sensitivity of CNT FETs to the electrostatic environment surrounding the nanotubes, enabling the detection of 0.5 pM concentrations of PvuII. This low concentration corresponds to the sequence-specific, electrical monitoring of ~7500 proteins within a sample volume of 0.025 μL. Such figures of merit compare favorably to state-of-the-art values reported not only for CNT-based systems[27-29] but also for alternative detection methodologies.[2-10] Notably, the signal transduction mechanism inherent to our devices indicates that their sensitivity can be further enhanced through simple optimization of the assay buffer. The detection strategy is also completely general, making it broadly applicable for monitoring any charged biomolecules that bind DNA. Moreover, given that our DNA-modified CNT FETs can be interrogated either individually or in massively parallel fashion, our integrated platform appears well suited for applications in multiplexed and/or portable lab-on-a-chip formats. Overall, our findings constitute a foundation for further development of CNT FET-based electrical assays for the monitoring, identification, and quantification of the interaction of not only proteins but also other charged analytes with DNA.

2.6 Supporting Information

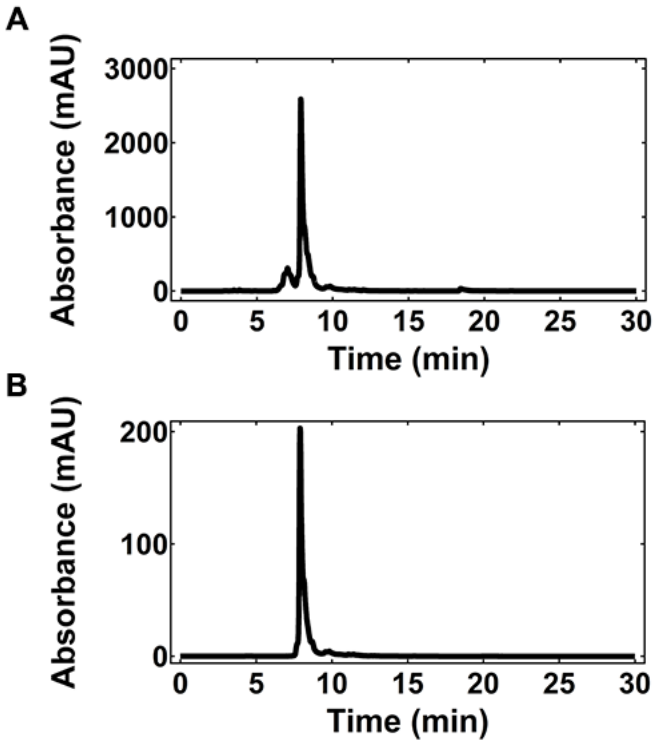

Figure S2.1: Typical high performance liquid chromatogram obtained for a pyrene-modified oligonucleotide. The absorbance was monitored at (A) 260 nm and (B) 350 nm. The oligonucleotide sequence was pyrene-$(CH_2)_4$-P_i-5'-TGCGTCTCAGTCGAAGTCAC-3'.

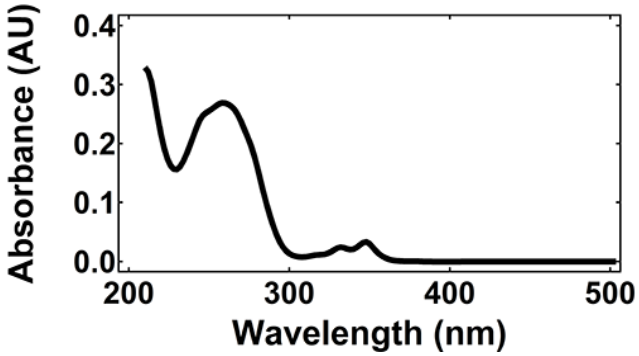

Figure S2.2: Typical UV-visible absorbance spectrum obtained for a pyrene-modified oligonucleotide. The peak at ~260 nm is characteristic of DNA and the peak at ~ 350 nm is characteristic of pyrene. The oligonucleotide sequence was pyrene-$(CH_2)_4$-P_i-5'-TGCGTCTCAGTCGAAGTCAC-3'.

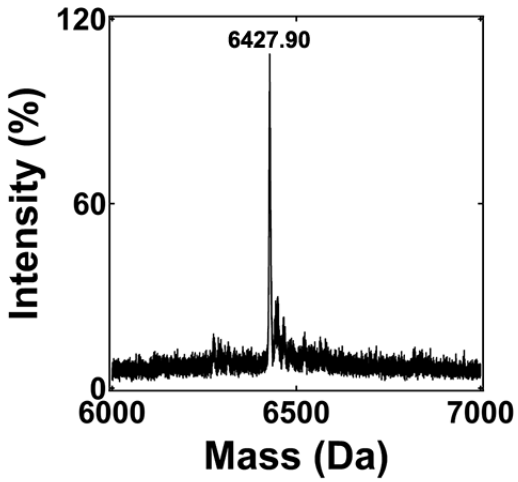

Figure S2.3: Typical matrix assisted laser desorption/ionization time of flight (MALDI-TOF) mass spectrometry spectrum obtained for pyrene-modified DNA. The observed mass of 6427.9 Da was in excellent agreement with the expected mass of 6429.3 Da. The oligonucleotide sequence was pyrene-$(CH_2)_4$-P_i-5'-TGCGTCTCAGTCGAAGTCAC-3'.

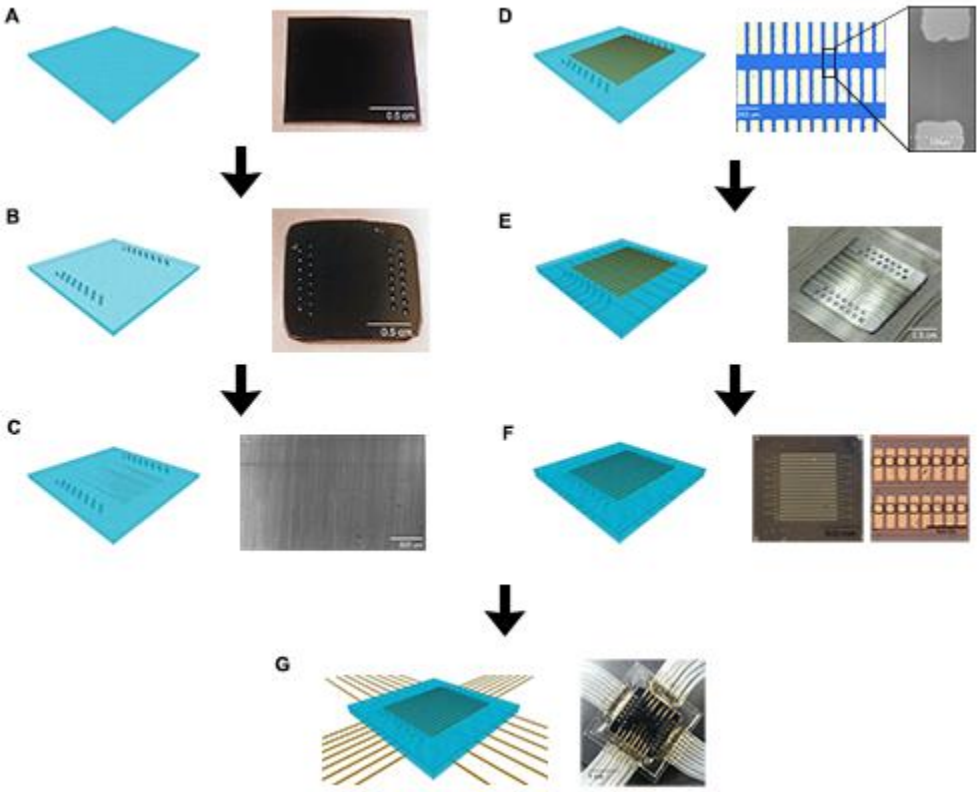

Figure S2.4: Illustration of the flow scheme employed for the fabrication of the microfluidic encapsulated carbon nanotube field effect transistor platform. (A) The first step consists of sectioning and cleaning of a silicon dioxide/silicon/silicon dioxide substrate. An illustration of the cut substrate is shown on the left, and an optical image of the substrate is shown on the right. (B) The second step consists of etching of through-holes for fluid flow in the substrate. An illustration of the etched substrate is shown on the left, and an optical image of the substrate is shown on the right. (C) The third step consists of growing a dense array of carbon nanotubes directly on the substrate surface through chemical vapor deposition (CVD). An illustration of an aligned nanotube array on the substrate surface is shown on the left, and a scanning electron microscope (SEM) image of the nanotube array is shown on the right. (D) The fourth step consists of the deposition of a gold electrode pattern directly on top of the carbon nanotubes, forming an array of carbon nanotube field effect transistors. An illustration of the electrode pattern is shown on the left. An optical image of the gold electrode pads and a scanning electron microscopy image of a single device are shown on the right. (E) The fifth step consists of binding a microfluidic housing to the bottom of the substrate, enabling the distribution of aqueous solutions to the devices. An illustration of the housing-covered substrate is shown on the left, and an optical image of the housing bound to the bottom of the substrate is shown on the right. (F) The sixth step consists of binding a microfluidic housing to the bottom of the substrate, facilitating the distribution of aqueous solutions to the devices and electrical testing of the devices. An illustration of the housing-covered substrate is shown on the left, and an optical image of the housing bound to the top of the substrate is shown on the right. (G) The seventh step consists of integrating tubing with the microfluidic housing, which enables the direct injection of aqueous solutions from a syringe pump. An illustration of the integrated tubing is shown on the left, and an optical image of the tubing attached to the PDMS housing is shown on the right.

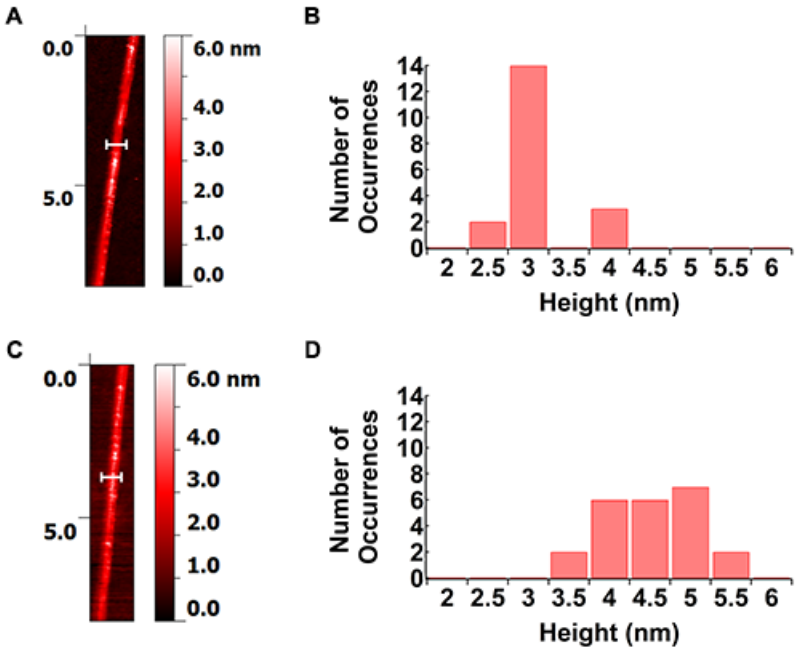

Figure S2.5: (A) Atomic force microscopy scan of a carbon nanotube before DNA self-assembly. (B) Histogram of height values obtained for the nanotube in (A). The average height was ~ 2.9 nm. (C) Atomic force microscopy scan of the same carbon nanotube from (A) after DNA self-assembly. (D) Histogram of height values obtained for the nanotube in (C). The average height was ~ 4.3 nm. Note the clear increase in height after DNA modification. For simplicity, the height values in the histograms were binned to the nearest ~0.5 nm.

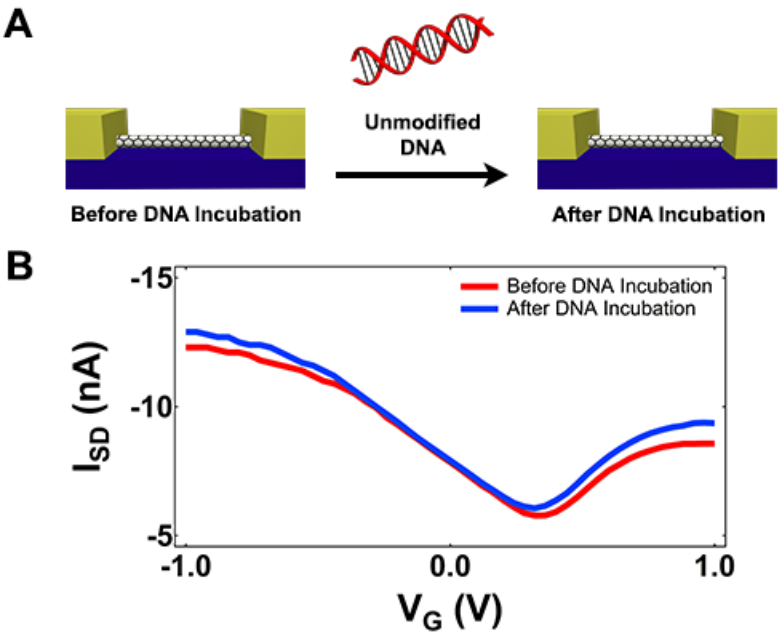

Figure S2.6: (A) Schematic illustration of the incubation of a carbon nanotube field effect transistor with DNA lacking a pyrene anchor. The DNA does not self-assemble at the nanotube surface. (B) A comparison of the current versus voltage electrical characteristics of a carbon nanotube field effect transistor before (red) and after (blue) incubation with DNA. Note that there is little change in the electrical characteristics of the device. The DNA sequence was 5'-TGCGTCTCAGTCGAAGTCAC-3' plus complement. The experiment was performed in 0.1 M sodium phosphate, 0.15 M sodium chloride, pH 7.2 buffer.

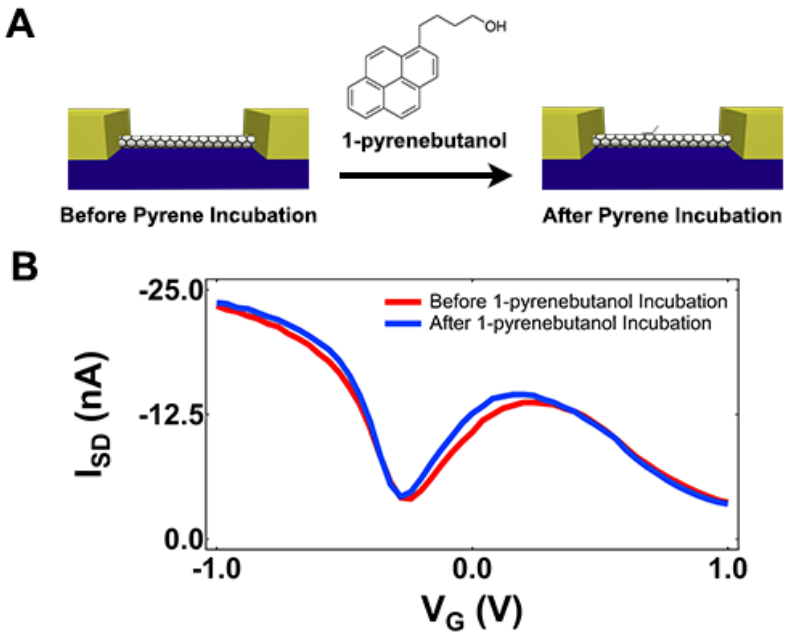

Figure S2.7: (A) Schematic illustration of the self-assembly of 1-pyrenebutanol at a carbon nanotube field effect transistor. (B) A comparison of the current versus voltage electrical characteristics of a carbon nanotube field effect transistor before (red) and after (blue) modification with 1-pyrenebutanol. Note that there is very little change in the electrical characteristics of the device, presumably due to the non-perturbative nature of pyrene's interaction with the nanotube. The experiment was performed in 0.1 M sodium phosphate, 0.15 M sodium chloride, pH 7.2 buffer.

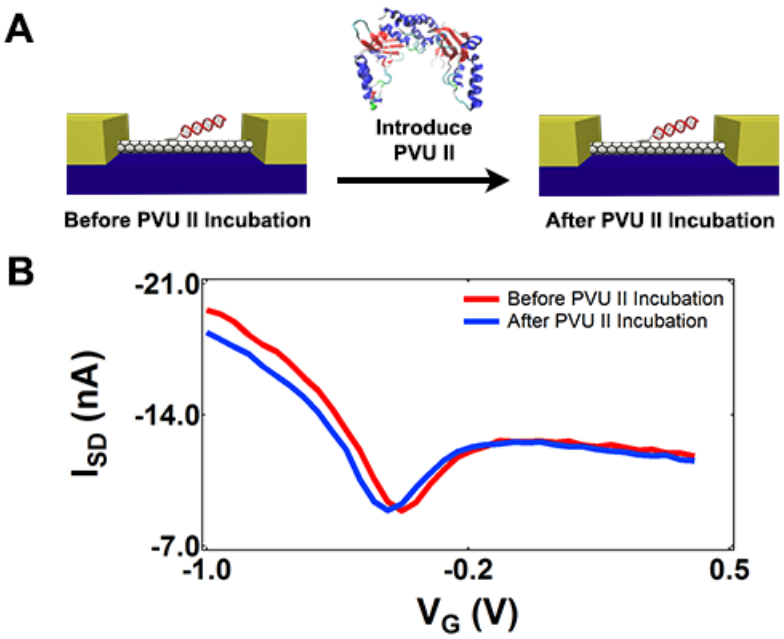

Figure S2.8: (A) Illustration of the activity of the PvuII restriction enzyme at the surface of a carbon nanotube field effect transistor modified with DNA lacking the enzyme's restriction site. Note that the enzyme does not cut the nanotube-bound DNA. (B) A comparison of the current versus voltage electrical characteristics of a carbon nanotube field effect transistor before (red) and after (blue) incubation with PvuII. Incubation of the device with PvuII has little effect on its electrical characteristics. The DNA sequence was pyrene-$(CH_2)_4$-P_i-5'-TAATTGGCGAAGTCTAGGAA-3' plus complement. The experiment was performed in 50 mM potassium acetate, 20 mM tris-acetate, 10 mM magnesium acetate, 1 mM DTT, pH 7.9 buffer at an enzyme concentration of 0.5 pM.

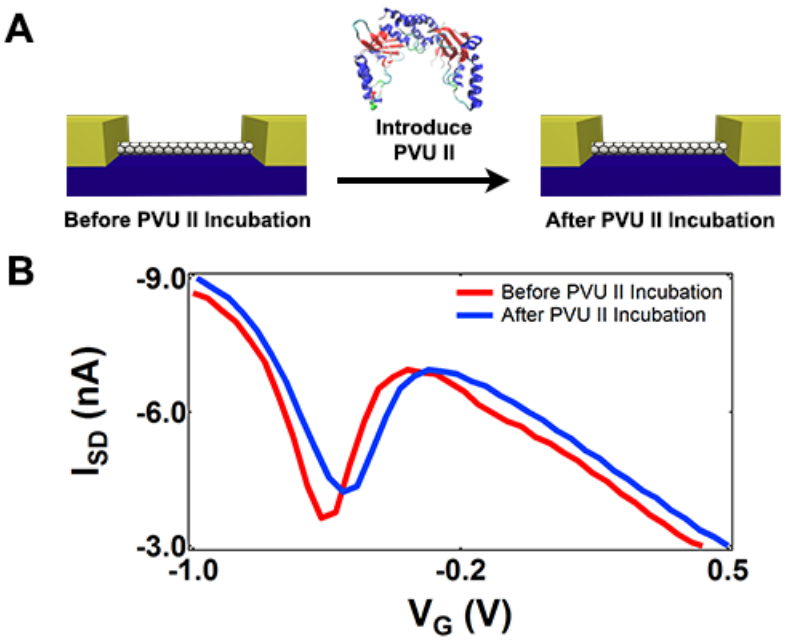

Figure S2.9: (A) Illustration of the activity of the PvuII restriction enzyme at the surface of a carbon nanotube field effect transistor that has not been modified with DNA. (B) A comparison of the current versus voltage electrical characteristics of a carbon nanotube field effect transistor before (red) and after (blue) incubation with PvuII. There is a slight change in the device electrical characteristics, presumably due to non-specific adsorption of the enzyme at the nanotube surface. The experiment was performed in 50 mM potassium acetate, 20 mM tris-acetate, 10 mM magnesium acetate, 1 mM DTT, pH 7.9 buffer at an enzyme concentration of 0.5 pM.

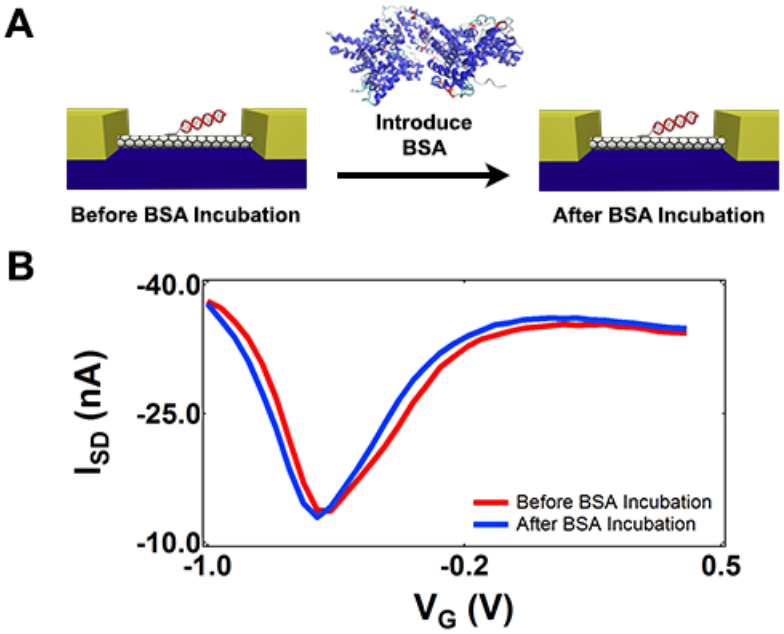

Figure S2.10: (A) Illustration of the incubation of a DNA-modified carbon nanotube field effect transistor with bovine serum albumin. The protein does not bind the DNA. (B) A comparison of the current versus voltage electrical characteristics of a carbon nanotube field effect transistor before (red) and after (blue) incubation with BSA. Incubation of the device with bovine serum albumin has little effect on its electrical characteristics. The DNA sequence was pyrene-$(CH_2)_4$-P_i-5'-TGCGTCT*CAGTCG*AAGTCAC-3' plus complement, where the PvuII restriction is italicized. The experiment was performed in 50 mM potassium acetate, 20 mM tris-acetate, 10 mM magnesium acetate, 1 mM DDT, pH 7.9 buffer at a protein concentration of 0.1 μM.

2.7 References

1. Alberts, B.; Johnson, A.; Lewis, J.; Raff, M.; Roberts, K.; Walter, P. *Molecular Biology of the Cell*, 4th ed; Garland Science: New York, **2002**.
2. Bulyk, M. L. Curr. Opin. *Biotechnol.* **2006**, 17, 422– 430
3. Geertz, M.; Maerkl, S. J. *Brief. Funct. Genomics* **2010**, 9, 362– 373
4. Stormo, G. D.; Zhao, Y. *Nat. Rev. Genet.* **2010**, 11, 751– 760
5. Hughes, T. R., Ed. *A Handbook of Transcription Factors*; Subcellular Biochemistry, Vol. 52; Springer Science+Business Media B.V.: Dordrecht, The Netherlands, **2011**.
6. Sikder, D.; Kodadek, T. *Curr. Opin. Chem. Biol.* **2005**, 9, 38– 45
7. Wang, J.; Lu, J.; Gu, G.; Liu, Y. J. *Endocrinol.* **2011**, 210, 15– 27
8. Xie, Z.; Hu, S.; Qian, J.; Blackshaw, S.; Zhu, H. *Cell. Mol. Life Sci.* **2011**, 68, 1657– 1668
9. Cai, Y.-H.; Huang, H. *Amino Acids* **2012**, 43, 1141– 1146
10. Dey, B.; Thukral, S.; Krishnan, S.; Chakrobarty, M.; Gupta, S.; Manghani, C.; Rani, V. *Mol. Cell. Biochem*. **2012**, 365, 279– 299
11. Darnell, J. E., Jr. *Nat. Rev. Cancer* **2002**, 2, 740– 749
12. Villard, J. *Swiss Med. Wkly*. **2004**, 134, 571– 579
13. Lee, T. I.; Young, R. A. *Cell* **2013**, 152, 1237– 1251
14. Patolsky, F.; Zheng, G.; Lieber, C. M. *Nanomedicine* **2006**, 1, 51– 65
15. Patolsky, F.; Zheng, G.; Lieber, C. M. *Nat. Protoc.* **2006**, 1, 1711– 1724
16. Wang, J. *Biosens. Bioelectron*. **2006**, 21, 1887– 1892
17. Grieshaber, D.; MacKenzie, R.; Vörös, J.; Reimhult, E. *Sensors* **2008**, 8, 1400– 1458
18. Sadik, O. A.; Aluoch, A. O.; Zhou, A. *Biosens. Bioelectron*. **2009**, 24, 2749– 2765
19. Feigel, I. M.; Vedala, H.; Star, A. *J. Mater. Chem*. **2011**, 21, 8940– 8954
20. Luo, X.; Davis, J. *J. Chem. Soc. Rev.* **2013**, 42, 5944– 5962
21. Gruner, G. *Anal. Bioanal. Chem*. **2006**, 384, 322– 335
22. Kim, S. N.; Rusling, J. F.; Papadimitrakopoulos, F. *Adv. Mater*. **2007**, 19, 3214– 3228
23. Allen, B. L.; Kichambare, P. D.; Star, A. *Adv. Mater*. **2007**, 19, 1439– 1451
24. Kauffman, D. R.; Star, A. *Chem. Soc. Rev.* **2008**, 37, 1197– 1206
25. Hu, P.; Zhang, J.; Li, L.; Wang, Z.; O'Neill, W.; Estrela, P. *Sensors* **2010**, 10, 5133– 5159
26. Guo, X. *Adv. Mater.* **2013**, 25, 3397– 3408
27. Liu, S.; Zhang, X.; Luo, W.; Wang, Z.; Guo, X.; Steigerwald, M. L.; Fang, X. *Angew. Chem., Int. Ed*. **2011**, 50, 2496– 2502
28. Wang, H.; Muren, N. B.; Ordinario, D.; Gorodetsky, A. A.; Barton, J. K.; Nuckolls, C. *Chem. Sci*. **2012**, 3, 62– 65
29. Guo, X.; Gorodetsky, A. A.; Hone, J.; Barton, J. K.; Nuckolls, C. *Nat. Nanotechnol*. **2008**, 3, 163– 167
30. Gorodetsky, A. A.; Dietrich, L. E. P.; Lee, P. E.; Demple, B.; Newman, D. K.; Barton, J. K. *Proc. Natl. Acad. Sci. U.S.A.* **2008**, 105, 3684– 3689
31. Gorodetsky, A. A.; Barton, J. K. *Langmuir* **2006**, 22, 7917– 7922
32. Gorodetsky, A. A.; Boal, A. K.; Barton, J. K. *J. Am. Chem. Soc.* **2006**, 128, 12082– 12083
33. Gorodetsky, A. A.; Green, O.; Yavin, E.; Barton, J. K. *Bioconjugate Chem.* **2007**, 18, 1434– 1441

34. Gorodetsky, A. A.; Barton, J. K. J. Am. Chem. Soc. **2007**, 129, 6074– 6075
35. Müller, A.; Das, S. K.; Kögerler, P.; Bögge, H.; Schmidtmann, M.; Trautwein, A. X.; Schünemann, V.; Krickemeyer, E.; Preetz, W. *Angew. Chem., Int. Ed.* **2000**, 39, 3413– 3417
36. Larrimore, L.; Nad, S.; Zhou, X.; Abruña, H.; McEuen, P. L. *Nano Lett.* **2006**, 6, 1329– 1333
37. Heller, I.; Chatoor, S.; Männik, J.; Zevenbergen, M. A. G.; Dekker, C.; Lemay, S. G. *J. Am. Chem. Soc.* **2010**, 132, 17149– 17156
38. Chen, R. J.; Choi, H. C.; Bansaruntip, S.; Yenilmez, E.; Tang, X.; Wang, Q.; Chang, Y.-L.; Dai, H. *J. Am. Chem. Soc.* **2004**, 126, 1563– 1568
39. Tang, X.; Bansaruntip, S.; Nakayama, N.; Yenilmez, E.; Chang, Y.-L.; Wang, Q. *Nano Lett.* **2006**, 6, 1632– 1636
40. Heller, I.; Janssens, A. M.; Männik, J.; Minot, E. D.; Lemay, S. G.; Dekker, C. *Nano Lett.* **2008**, 8, 591– 595
41. Besteman, K.; Lee, J.-O.; Wiertz, F. G. M.; Heering, H. A.; Dekker, C. *Nano Lett*. **2003**, 3, 727– 730
42. Taft, B. J.; Lazareck, A. D.; Withey, G. D.; Yin, A.; Xu, J. M.; Kelley, S. O. *J. Am. Chem. Soc.* **2004**, 126, 12750– 12751
43. Choi, Y.; Moody, I. S.; Sims, P. C.; Hunt, S. R.; Corso, B. L.; Perez, I.; Weiss, G. A.; Collins, P. G. *Science* **2012**, 335, 319– 324
44. Chen, R. J.; Zhang, Y.; Wang, D.; Dai, H. *J. Am. Chem. Soc.* **2001**, 123, 3838– 3839
45. Gorodetsky, A. A.; Hammond, W. J.; Hill, M. G.; Slowinski, K.; Barton, J. K. *Langmuir* **2008**, 24, 14282– 14288
46. Gorodetsky, A. A.; Ebrahim, A.; Barton, J. K. *J. Am. Chem. Soc.* **2008**, 130, 2924– 2925
47. Gorodetsky, A. A.; Buzzeo, M. C.; Barton, J. K. *Bioconjugate Chem.* **2008**, 19, 2285– 2296
48. Ilani, S.; McEuen, P. L. *Annu. Rev. Condens. Matter Phys.* **2010**, 1, 1– 25
49. Lerner, M. B.; Resczenski, J. M.; Amin, A.; Johnson, R. R.; Goldsmith, J. I.; Johnson, A. T. C. *J. Am. Chem. Soc.* **2012**, 134, 14318– 14321
50. Artyukhin, A. B.; Stadermann, M.; Friddle, R. W.; Stroeve, P.; Bakajin, O.; Noy, A. *Nano Lett.* **2006**, 6, 2080– 2085
51. Leyden, M. R.; Messinger, R. J.; Schuman, C.; Sharf, T.; Remcho, V. T.; Squires, T. M.; Minot, E. D. *Lab Chip* **2012**, 12, 954– 959
52. Sorgenfrei, S.; Chiu, C.-Y.; Johnston, M.; Nuckolls, C.; Shepard, K. L. *Nano Lett.* **2011**, 11, 3739– 3743
53. Choi, Y.; Olsen, T. J.; Sims, P. C.; Moody, I. S.; Corso, B. L.; Dang, M. N.; Weiss, G. A.; Collins, P. G. *Nano Lett*. **2013**, 13, 625– 631
54. Athanasiadis, A.; Vlassi, M.; Kotsifaki, D.; Tucker, P. A.; Wilson, K. S.; Kokkinidis, M. *Nat. Struct. Biol*. **1994**, 1, 469– 475
55. Pingoud, A.; Jeltsch, A. *Nucleic Acids Res*. **2001**, 29, 3705– 3727
56. Nastri, H. G.; Evans, P. D.; Walker, I. H.; Riggs, P. D. *J. Biol. Chem*. **1997**, 272, 25761– 25767
57. Xie, F.; Qureshi, S. H.; Papadakos, G. A.; Dupureur, C. M. *Biochemistry* **2008**, 47, 12540– 12550
58. Cheng, X.; Balendiran, K.; Schildkraut, I.; Anderson, J. E. *EMBO J*. **1994**, 13, 3927– 3935

59. Minot, E. D.; Janssens, A. M.; Heller, I.; Heering, H. A.; Dekker, C.; Lemay, S. G. *Appl. Phys. Lett.* **2007**, 91, 093507

CHAPTER 3 Molecular Dynamics Simulations of Perylenediimide DNA Base Surrogates

3.1 Abstract

Perylene-3,4,9,10-tetracarboxylic diimides (PTCDIs) are a well-known class of organic materials. Recently, these molecules have been incorporated within DNA as base surrogates, finding ready applications as probes of DNA structure and function. However, the assembly dynamics and kinetics of PTCDI DNA base surrogates have received little attention to date. Herein, we employ constant temperature molecular dynamics simulations to gain an improved understanding of the assembly of PTCDI dimers and trimers. We also use replica-exchange molecular dynamics simulations to elucidate the energetic landscape dictating the formation of stacked PTCDI structures. Our studies provide insight into the equilibrium configurations of multimeric PTCDIs and hold implications for the construction of DNA-inspired systems from perylene-derived organic semiconductor building blocks.

3.2 Introduction

Perylene-3,4,9,10-tetracarboxylic diimide (PTCDI or perylenediimide) derivatives constitute a well-known and extensively studied class of organic materials.[1-8] Due to their tunable coloration and excellent stability, PTCDIs have found ready applications as industrial dyes and pigments.[1, 2] Moreover, PTCDIs' favorable electrochemical, photophysical, and self-assembly properties have facilitated not only the fundamental study of charge transport phenomena but also the development of various organic electronic devices, such as transistors and solar cells.[3-8] Consequently, a number of synthetic methodologies have been developed for modulating the properties of PTCDIs.[2, 7, 8] For example, substitution of these molecules' aromatic core and imide positions provides a degree of control over their electronic properties

and self-assembly behavior, respectively.[8] Thus, given the various advantageous features of PTCDIs, it is not surprising that they have attracted much attention from both industry and academia for over 100 years.[1-8]

Due to the widespread interest in the properties and applications of PTCDIs, these molecules have been investigated via computational techniques within certain contexts.[5, 9-14] For example, various studies have used density functional theory to establish relationships between the solid state packing and emergent electronic functionality of various substituted PTCDIs.[5, 9-13] Moreover, a handful of reports have used molecular dynamics simulations to understand the aggregation and assembly dynamics of PTCDIs both in solution and in the solid state.[5, 11-14] These efforts have afforded fundamental insight that is valuable for the design of improved PTCDI-based materials.

Recently, Wagenknecht and co-workers have developed a new class of PTCDI derivatives for use as artificial DNA base surrogates.[15-20] Within the context of standard oligonucleotide synthesis, such derivatives are advantageous because they can be incorporated in arbitrary positions within the DNA base pair stack in high yield.[15-26] To date, these molecules have been used for a number of applications, including the assembly of higher-order DNA ensembles,[20-22] the photophysical investigation of DNA structure/function,[16, 17, 19] the study of charge transfer in DNA hairpins,[23-25] and the electrochemical interrogation of DNA monolayers.[26] However, the assembly dynamics and kinetics of PTCDI DNA base surrogates have not been extensively explored via computational techniques.[21, 22]

Herein, we present a molecular dynamics study of multimeric PTCDI DNA base surrogates. We first design, synthesize, and characterize model oligonucleotides featuring one, two, and three covalently attached PTCDI moieties. We then parametrize the oligonucleotides'

PTCDI subunits and formulate an atomistic model of these constructs. We subsequently employ constant-temperature molecular dynamics simulations to develop an improved understanding of the assembly kinetics of PTCDI dimers and trimers. We in turn perform replica exchange molecular dynamics simulations to obtain the energetic landscape associated with ensembles of our stacked PTCDI structures at equilibrium. Altogether, our findings may hold implications for the design of DNA-inspired systems and materials from not only PTCDIs but also other organic semiconductor building blocks.

3.3 Experimental Section

3.3.1 Preparation of the DNA Phosphoramidites

The phosphoramidites required for DNA synthesis were purchased from Glen Research, Inc., or Azco Biotech, Inc., and used as received. The perylenediimide phosphoramidites were synthesized and characterized according to established literature protocols.[26] The identity and purity of the perylenediimide phosphoramidites, as well as all intermediates required for their synthesis, were confirmed with ^{1}H NMR, ^{13}C NMR, ^{31}P NMR, and mass spectrometry.[26]

3.3.2 Synthesis, Purification, and Characterization of the Oligonucleotides

The PTDCI-modified oligonucleotides (Figure 3.1) were prepared according to standard commercial protocols recommended by Glen Research, Inc., for an Applied Biosystems (ABI) 394 DNA synthesizer. Extended coupling times were used for the incorporation of perylenediimide phosphoramidites, as previously described.[26] After synthesis, the oligonucleotides were cleaved from the solid support by treatment with aqueous ammonium hydroxide and purified with high performance liquid chromatography (HPLC) on an Agilent

1260 Infinity system. The oligonucleotides were eluted with a gradient evolved from 95% solvent A and 5% solvent B to 0% solvent A and 100% solvent B over 30 min at a flow rate of 1 mL/min (solvent A, 50 mM ammonium acetate, pH = 6 buffer; solvent B, acetonitrile) on Agilent reverse phase C4 or C8 columns (see Figure S3.1 for typical chromatograms). The UV–visible (UV−vis) absorption spectra of the oligonucleotides were obtained with an Agilent 1260 Infinity Series diode array detector during chromatographic purification. The MALDI-TOF mass spectra of the oligonucleotides were recorded on an Applied Biosystems Sciex MALDI-TOF/TOF 5800 series mass spectrometer in reflectron negative mode, using a 349 nm Nd:YAG laser as the illumination source and 3-hydroxypicolinic acid as the matrix (see Figure S3.2 for typical spectra).

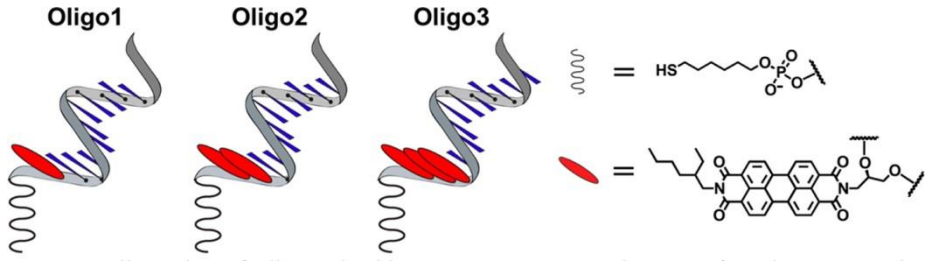

Figure 3.1: Illustration of oligonucleotides Oligo1, Oligo2, and Oligo3 containing 1, 2, and 3 PTCDI base surrogates (red ovals), respectively. The DNA sequences of these macromolecules were 5′-$(A)_{10}(P)_n$-S-3′, where the A, P, and S indicate the locations of the adenines, PTCDIs, and thiols, respectively, and *n* corresponds to the number of PTCDIs.

3.3.3 Parameterization of the Perylenediimide Base Surrogates

For the simulations, three separate residues containing terminal phosphate moieties were designed according to established literature protocols (Figure S3.3).[27] The chemical structures of the residues were exported as mol2 files from ChemDraw 13.0, and these structures were initially optimized using molecular mechanics in Gaussian 09.[28] The geometry optimization was

completed in Gaussian 09 with the Hartree–Fock method and the 6-31G(d) basis set, via the methodology previously reported for the Generalized AMBER Force Field (GAFF).[28, 29]

After convergence of the structures, the atomic point charges for the three residues were determined via the two-step Restricted Electrostatic Potential (RESP) method (Figure S3.4 and Table S1-3). The residues' electrostatic potentials were first calculated in Gaussian 09, and the Merz–Kollman scheme was used to correctly output the log file for AMBER's *antechamber*.[29] Next, atom typing was completed by *antechamber*, and the resulting charges were appended into mol2 files. The mol2 files were in turn imported into *xleap* by using the GAFF force field parameters. To form multimeric PTCDI constructs for the subsequent molecular dynamics simulations, the residues were appended in *xleap*,[29-31] with the redundant terminal phosphate moieties removed.[27] Note that charge constraints were enforced according to established literature precedent for parametrization of DNA residues in AMBER.[27]

3.3.4 Molecular Dynamics Simulations of the Perylenediimide Base Surrogate Stacking Kinetics

Molecular dynamics simulations of PTCDI stacking kinetics (20 total) were performed with GAFF in NAMD 2.9.[32, 33] The simulations employed the Generalized Born Implicit Solvent model (GBIS) and a monovalent salt concentration of 0.115 M.[32, 33] For each simulation, the starting configuration was obtained by turning off the attractive van der Waals interactions in the force field and setting the temperature to 500 K, thereby ensuring that all PTCDI moieties were completely separated from one another in an unstacked random open configuration. To initiate the simulation, the attractive van der Waals interactions were turned on and the initial temperature was set to 300 K. All of the simulations were performed at a constant temperature of 300 K for 20 ns, ensuring that steady state was reached. The simulations were analyzed by

monitoring the relative center of mass (COM) distances and offset angles for every pair of PTCDIs. The COM distances were calculated from the atomic coordinates and atomic mass of the individual PTCDIs. Here, the offset angles were obtained by constructing a vector from the nitrogen closest to the backbone to the nitrogen farthest from the backbone for the individual PTCDIs (Figure S3.5). The dot product of these vectors for every pair of PTCDIs defined the offset angles used for the analysis. The COM distances and offset angles indicated the relative separation and alignment of the PTCDIs, respectively. As an example, if the COM distance of two PTCDIs is ~3.4 Å and their offset angle is 0°, the two molecules are stacked and perfectly aligned on top of one another (Figure S3.6). The simulations also yielded the van der Waals and electrostatic interactions for each pair of PTCDIs. These interactions were monitored as a function of time to gain insight into the factors driving the self-assembly of PTCDI ensembles.

3.3.5 Replica-Exchange Molecular Dynamics Simulations of Perylenediimide Base Surrogate Assembly

Replica exchange molecular dynamics (REMD) simulations were performed to explore the energetic landscape of the oligonucleotides' stacked PTCDI subunits.[34] The simulations were run for 16 replicates distributed over a temperature range of 290 to 700 K. The simulation time was 320 ns per replica, corresponding to 80,000 total exchanges, with an exchange attempt every 4 ps. The simulations generated the equilibrium atomic structures for an ensemble of the PTCDI subunits. These structures were analyzed via the MBAR method, enabling calculation of the potential of mean force (PMF) for the stacked PTCDIs as a function of their COM distances and offset angles.[35] This analysis yielded the free energy landscapes of our constructs at 300 K.

3.4 Results and Discussion

We began our experiments by designing the series of model PTCDI-containing macromolecules shown in Figure 3.1 (Oligo1, Oligo2, and Oligo3). These macromolecules incorporated 1 to 3 PTCDI moieties, an alkanethiol functionality at their 3′ end, and a polyadenine tract at their 5′ end (the terminal modifications were included to mitigate intermolecular aggregation). Because bulky PTCDIs are typically placed either at terminal positions or opposite abasic sites within duplex DNA,[15-26] we specifically focused our efforts on the preparation and analysis of single stranded DNA. Indeed, upon binding the 3′ polyadenine tract of our constructs, the complementary strands would be expected to exhibit a relatively small effect on the rapid assembly dynamics and kinetics of the terminal PTCDI DNA base surrogates. Overall, Oligo1, Oligo2, and Oligo3 represented reasonable general analogues for the diverse class of perylene-modified oligonucleotides previously investigated with photophysical techniques in solution[16, 17, 19] and electrochemical techniques at solid substrates.[26]

We characterized Oligo1, Oligo2, and Oligo3 with UV–vis spectroscopy (Figure 3.2), observing a clear evolution in the molecules' spectra as the number of PTCDI moieties increased. For Oligo1, the spectrum of DNA1 was indicative of a single, isolated PTCDI, with three characteristic absorption peaks of successively increasing intensity at 466, 496, and 534 nm (Figure 3.2). However, the situation was markedly different for Oligo2 and Oligo3. Although the absorption peaks maintained similar positions, the spectra were broadened, with the absorption peaks at 498 nm for Oligo2 and 497 nm for Oligo3 now exhibiting the largest relative intensities. This type of evolution in our constructs' UV−vis spectra was indicative of strong pi–pi stacking interactions between the adjacent PTCDIs.[2-8, 36]

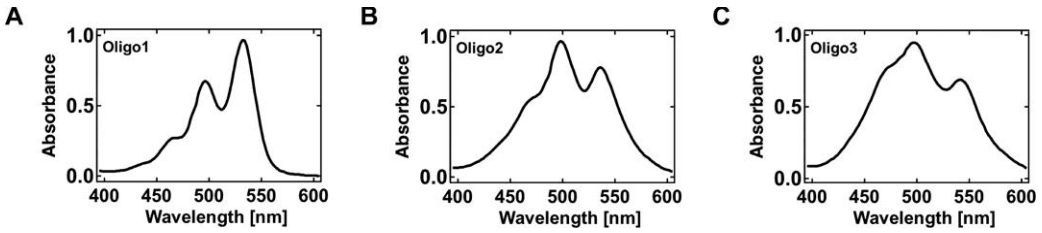

Figure 3.2: Normalized UV–vis absorption spectra obtained for Oligo1, Oligo2, and Oligo3 containing 1, 2, and 3 PTCDIs, respectively. Note the change in the relative intensities of the absorption peaks for Oligo2 and Oligo3 compared to Oligo1.

With our model constructs in hand, we proceeded to perform constant temperature molecular dynamics simulations for the PTCDI subunits of Oligo2 and Oligo3 (Figure 3.3). For simplicity, we only considered the structures shown in Figure 3.3 (denoted as P1, P2, and P3), removing the alkyl tails on the PTCDIs, the 3′ alkanethiol functionalities, the 5′ polyadenine tracts, and the terminal phosphate groups (when appropriate). We leveraged established literature protocols previously developed for oligonucleotides and DNA to parametrize the PTCDI moieties with the Generalized AMBER Force Field, facilitating the computational analysis.[29-31] Here, through our simulations, we anticipated gaining insight into both the kinetics of self-assembly and the ultimate geometries for P2 and P3.

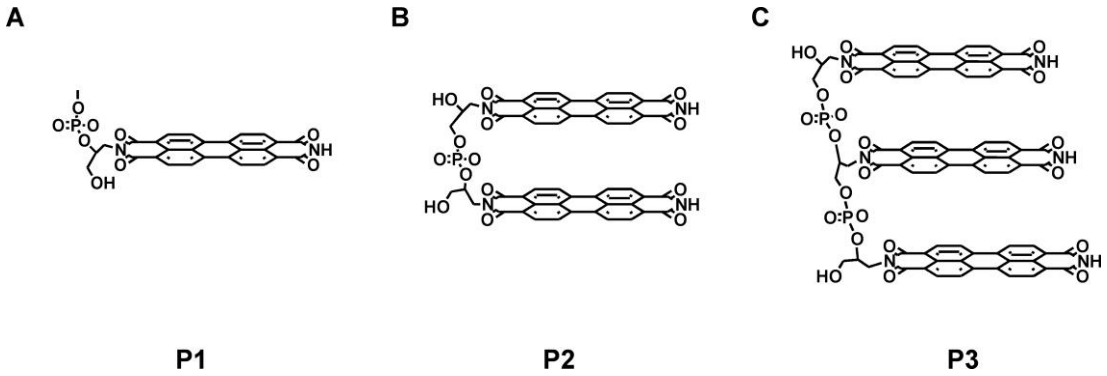

Figure 3.3: Chemical structures of the PTCDI subunits used for the molecular dynamics simulations. The subunits are labeled as P1, P2, and P3, and they correspond to Oligo1, Oligo2, and Oligo3, respectively.

We initially investigated the kinetics of self-assembly for the two PTCDI moieties of P2, as illustrated for a typical simulation in Figure 3.4. At t = 0.051 ns, the two PTCDIs maintained a random open configuration (Figure 3.4A), with a COM distance of 18.34 Å (Figure 3.4E) and an offset angle of 125.7° (Figure 3.4F). After 1.718 ns, the top PTCDI had started to flip (Figure 3.4B), leading to a slight decrease in the COM distance to 14.34 Å (Figure 3.4E) and a reduction in the offset angle to 68.28° (Figure 3.4F). After 1.912 ns, the top PTCDI had begun to orient itself toward the bottom PTCDI (Figure 3.4C), leading to a further decrease in the COM distance (Figure 3.4E) and an additional reduction in the offset angle (Figure 3.4F). Finally, after 2.419 ns, the two PTCDIs had collapsed to a stacked state (Figure 3.4D), with an average COM distance of 4.6 Å (Figure 3.4E) and an average offset angle of 15.51° (Figure 3.4F). Here, although the two PTCDIs remain stacked for the remainder of the ∼20 ns simulation, their COM distances and offset angles varied by ∼0.44 Å and ∼7.83°, respectively. Such geometric variability likely resulted from thermal fluctuations, hinting at some dynamic character for the final configuration. Nonetheless, the final stacked dimer was highly reproducible, with nearly identical results obtained for ten independent repetitions.

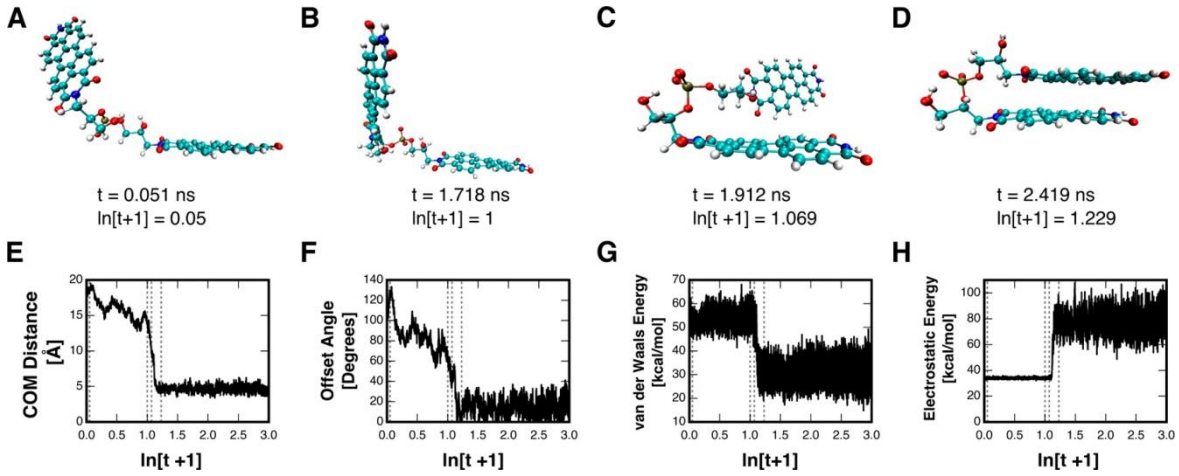

Figure 3.4: Snapshots of P2 during a molecular dynamics simulation at times of (A) t = 0.051 ns, (B) t = 1.718 ns, (C) t = 1.912 ns, and (D) t = 2.419 ns. The sequence demonstrates the transition of P2 from an open random configuration to a stacked configuration. (E) The evolution of the centers of mass (COM) distance between the two PTCDIs of P2 as a function of time. (F) The evolution of the offset angle between the two PTCDIs of P2 as a function of time. (G) The evolution of the van der Waals energy of P2 as a function of time. (H) The evolution of the electrostatic energy of the PTCDIs' carbonyl oxygens distal to the alkane phosphate backbone as a function of time. The four vertical dashed lines in E, F, G, and H correspond to the times used for the snapshots in A, B, C, and D. The simulations were performed at a constant temperature of 300 K.

To gain additional insight into the self-assembly of P2's PTCDI moieties, we analyzed the energetics driving this process. When the two PTCDIs collapsed to a stacked configuration between ~1.9 ns and ~2.4 ns (Figure 3.4E,F), there was a sharp decrease in the van der Waals energy of the system, due to pi–pi interactions between the molecules' aromatic cores (Figure 3.4G), and a sharp increase in the electrostatic energy, due to repulsion between the PTCDIs' carbonyl groups located distal to the alkane phosphate backbone (Figure 3.4H). The competition between these two sets of interactions appeared to dictate the final arrangement of the system, where there was substantial overlap between the perylene cores but a misalignment of the carbonyl groups (Figure 3.4D).

We next investigated the kinetics of self-assembly for the three PTCDI moieties of P3. In our experiments, we observed that the formation of P3's final arrangement required a two-step mechanism. First, two of the PTCDIs formed a dimer analogous to the one found for the final

configuration of P2. Second, the remaining third PTCDI stacked with this dimer to form a trimer. Although our simulations revealed multiple possibilities for the PTCDIs' stacking order (Figure 3.5 and Figures S3.7 and S3.8), this general mechanism was highly reproducible, with similar results obtained for ten independent simulations.

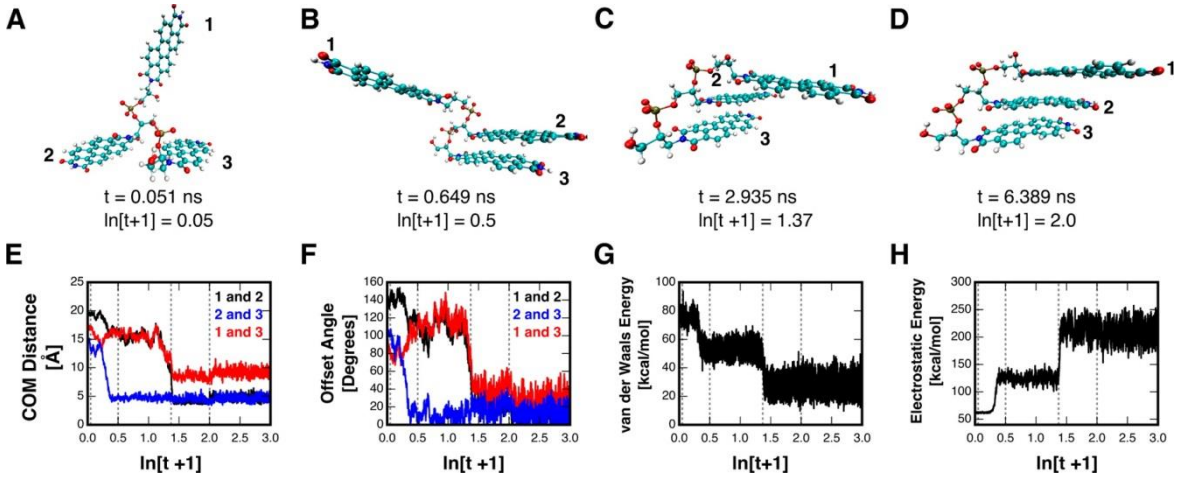

Figure 3.5: Snapshots of P3 during a molecular dynamics simulation at times of (A) t = 0.051 ns, (B) t = 0.649 ns, (C) t = 2.935 ns, and (D) t = 6.389 ns. The constituent PTCDIs of P3 are labeled as **1**, **2**, and **3**. The sequence demonstrates the transition of P3 from an open random configuration to a stacked configuration. (E) The evolution of the centers of mass (COM) distance between PTCDIs **1** and **2** (black curve), PTCDIs **2** and **3** (blue curve), and PTCDIs **1** and **3** (red curve) as a function of time. (F) The evolution of the offset angle between PTCDIs **1** and **2** (black curve), PTCDIs **2** and **3** (blue curve), and PTCDIs **1** and **3** (red curve) as a function of time. (G) The evolution of the van der Waals energy of P3 as a function of time. (H) The evolution of the electrostatic energy of the PTCDIs' carbonyl oxygens distal to the alkane phosphate backbone as a function of time. The four vertical dashed lines in E, F, G, and H correspond to the times used for the snapshots in A, B, C, and D. The simulations were performed at a constant temperature of 300 K.

As an example, Figure 3.5 shows a typical P3 stacking kinetics simulation, which demonstrates the aforementioned multistep mechanism and the most likely assembly pathway. At t = 0.051 ns, the three constituent PTCDIs (denoted as **1**, **2**, and **3**) were unstacked with a random open configuration (Figure 3.5A). Initially, as illustrated by the snapshot at t = 0.649 ns (Figure 3.5B), **2** and **3** formed a dimer during the first step of the stacking mechanism. There was a corresponding sharp drop from 13.34 to 5.02 Å in the COM distance (Figure 3.5E) and from

100.61° to 1.30° in the offset angle (Figure 3.5F) between **2** and **3**. In turn, as illustrated by the snapshot at t = 2.935 ns (Figure 3.5C), **1** stacked on top of the dimer to form a trimer during the second step of the stacking mechanism. For this step, there was a sharp drop from 9.09 to 5.61 Å in the COM distance (Figure 3.5E) and from 63.26° to 13.76° in the offset angle (Figure 3.5F) between **1** and **2**. There also was an accompanying drop from 10.92 to 9.29 Å in the COM distance (Figure 3.5E) and from 73.07° to 30.45° in the offset angle (Figure 3.5F) between **1** and **3**. Although the three PTCDIs remained in a stacked arrangement for the remainder of the ∼20 ns simulation, as illustrated by the snapshot at t = 6.389 ns (Figure 3.5D), we again observed variability in their relative COM distances and offset angles (Figure 3.5E,F), indicating some dynamic character for the final configuration.

To further understand the self-assembly of P3's PTCDI moieties, we analyzed the energetics dictating the overall process. In the first step of the mechanism, the formation of the dimer was driven by a sharp decrease in the van der Waals energy of the system, due to pi–pi interactions between the molecules' aromatic cores (Figure 3.5G), and a sharp increase in the electrostatic energy, due to repulsion between the PTCDIs' carbonyl groups located distal to the alkane phosphate backbone (Figure 3.5H), as also observed for P2 above (Figure 3.4G,H). In the second step of the mechanism, a similar interplay of favorable and unfavorable interactions appeared to drive formation of the trimer, as indicated by similar changes in the van der Waals and electrostatic energies (Figure 3.5G,H). These competing interactions ensured that the three constituent PTCDIs of P3 adopted a twisted arrangement in the final equilibrium configuration, where they were stacked but offset with respect to one another (Figure 3.5D).

We proceeded to perform REMD simulations for P2 and P3. Relative to constant temperature simulations, REMD simulations are advantageous because they minimize the possibility of kinetic traps.[34] Moreover, replica exchange simulations enable direct calculation of the potential of mean force (PMF), facilitating comparisons between the relative free energies of different equilibrium structures.[35] Here, through such simulations, we anticipated gaining insight into the distinct configurations possible for P2 and P3 over a broad temperature window.

We performed REMD simulations for P2, obtaining equilibrium structures such as the one illustrated in Figure 3.6A,B. These configurations spanned a range of COM distance and average offset angle combinations, corresponding to various PMF values (Figure 3.6C). As a general rule, the low free energy structures found for P2 featured COM distances between 4.2 and 5.2 Å and offset angles between 3° and 22°. For example, the lowest energy equilibrium structure shown in Figure 3.6A,B featured a COM distance of 4.53 Å and an offset angle of 14.61°, in excellent agreement with the kinetic simulations above. Notably, configurations with COM distances of >∼7 Å possessed large free energies, underscoring the PTCDIs' known propensity for stacking.[2-8] However, configurations with COM distances of ∼3.4 Å and offset angles close to 0° still possessed large free energies, indicating that perfect overlap of the two PTCDIs was not favored. Overall, these simulations provided additional insight into the preferred equilibrium arrangement of the PTCDI moieties of P2.

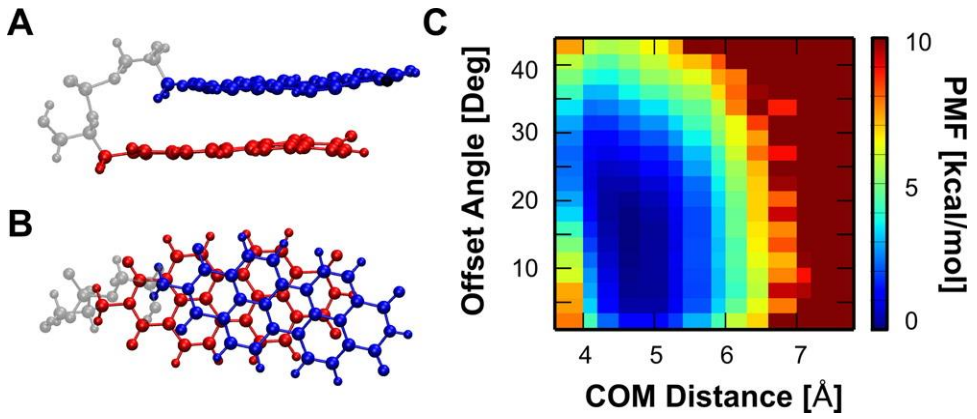

Figure 3.6: Snapshots of the lowest energy equilibrium structure observed for P2 from (A) a side view and (B) a top view. The backbone is colored gray, and the two PTCDIs are colored red and blue. (C) The potential of mean force (PMF) in kcal/mol as a function of both the centers of mass (COM) distance and the offset angle between the two PTCDIs of P2, as obtained from a replica exchange simulation at 300 K.

We subsequently performed REMD simulations for P3, obtaining equilibrium structures such as the one illustrated in Figure 3.7A,B. These simulations again yielded an ensemble of possible P3 configurations, which we analyzed by comparing the relative orientations of the three constituent PTCDIs (denoted as **1**, **2**, and **3**). The possible COM distance and offset angle combinations obtained for **1** and **2**, along with their corresponding PMF values, are illustrated in Figure 3.7C, and the possible COM distance and offset angle combinations obtained for **2** and **3**, along with their corresponding PMF values, are illustrated in Figure 3.7D. As observed for P2, the equilibrium structures with the lowest free energies featured COM distances between 4.2 and 5.2 Å and offset angles between 3° and 22°. For example, the lowest energy equilibrium structure shown in Figure 3.7C,D featured a COM distance of 4.86 Å and an offset angle of 6.01° for **1** and **2**, as well as a COM distance of 5.24 Å and an offset angle of 4.5° for **2** and **3**. Although the three PTCDIs comprising this structure adopted a stacked arrangement, they did not overlap perfectly and were slightly offset with respect to one another. These findings were again in agreement with the kinetics simulations and afforded an improved understanding of the energetic landscape dictating the self-assembly of P3.

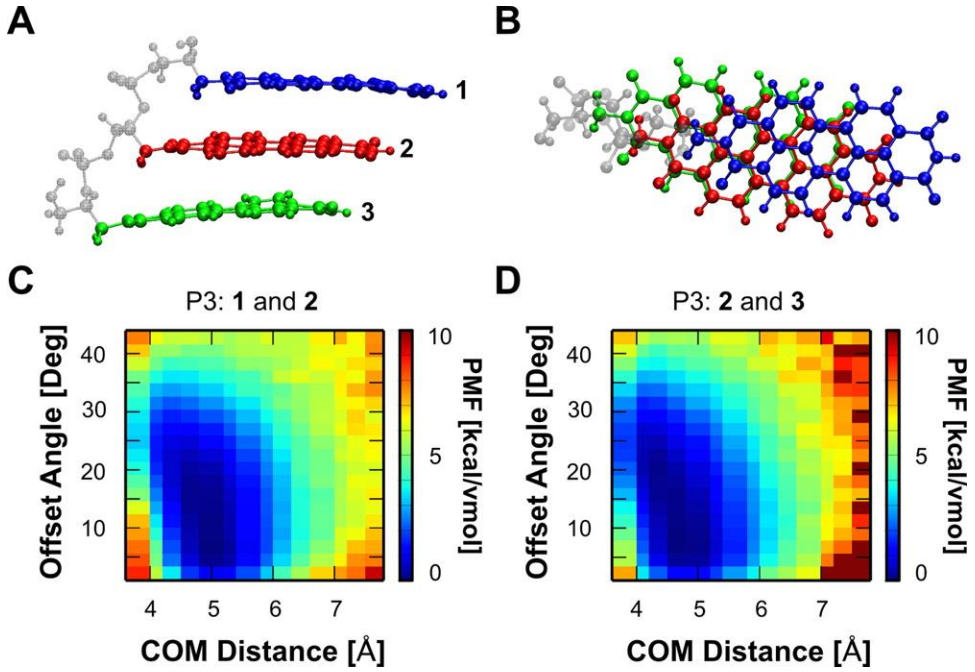

Figure 3.7: Snapshots of the lowest energy equilibrium structure observed for P3 from (A) a side view and (B) a top view. The backbone is colored gray, and PTCDIs **1**, **2**, and **3** are colored blue, red, and green, respectively. (C) The potential of mean force (PMF) in kcal/mol as a function of both the centers of mass (COM) distance and the offset angle between PTCDIs **1** and **2** of P3, as obtained from a replica exchange simulation at 300 K. (D) The potential of mean force (PMF) in kcal/mol as a function of both the center of mass (COM) distance and the offset angle between PTCDIs **2** and **3** of P3, as obtained from a replica exchange simulation at 300 K.

Finally, our REMD simulations indicated that the PTCDI moieties comprising the P2 and P3 equilibrium structures were nonplanar on short time scales (Figure 3.6A,B and Figure 3.7A,B). To gain insight into the origin of this effect, we compared the distortion from planarity found for the stacked, interacting PTCDIs of P2 and P3 with the distortion from planarity found for the independent PTCDI of P1. For this comparison, we defined a bend angle between two vectors from the center to the edge of the PTCDIs (Figure S3.9). The PTCDI of P1 featured a range of bend angles between 153.27° and 179.92°, with an average value of 174.66 ± 3.67° (Figure S3.9). Interestingly, we found that the PTCDIs of P2 and P3 all featured nearly identical bending angle distributions (Figures S3.10 and S3.11). Given that the average distortions were

small and not dependent on stacking interactions, we postulated that the observed deviations from planarity were likely due to thermal fluctuations. These findings further underscored the rich dynamics of stacked PTCDIs, which warrant additional exploration.

3.5 Conclusion

In summary, we have used constant temperature and replica exchange molecular dynamics simulations to investigate the self-assembly of covalently linked perylene-3,4,9,10-tetracarboxylic diimide DNA base surrogates. Together, our computational analyses yielded insight not readily apparent from experimental methodologies and were significant for several reasons. First, to the best of our knowledge, the stacking kinetics of PTCDI DNA base surrogates have received little attention from a computational perspective, especially with regard to investigating the process in its entirety. Second, our simulations have allowed for observation of the assembly kinetics in atomistic detail, revealing that the underlying mechanism is quite complex and may encompass multiple distinct pathways. Third, our studies have unveiled the energetics of multimeric PTCDI ensembles, indicating that a complex interplay of attractive van der Waals and repulsive electrostatic interactions dictates their assembly and final structures. Fourth, the simulations demonstrate that the observed equilibrium structures are not fully static and possess some dynamic character, as evidenced by fluctuations in the relative positions and planarity of the stacked PTCDIs. Fifth, the presented computational framework is quite general and can be readily extended to the study of more complex sequence- and length-variable systems consisting of covalently linked pi-conjugated organic semiconductor building blocks. Overall, our studies constitute a foundation for the rational design and construction of precisely defined one-dimensional nanowires that draw inspiration from the structure of DNA.

3.6 Supporting Information

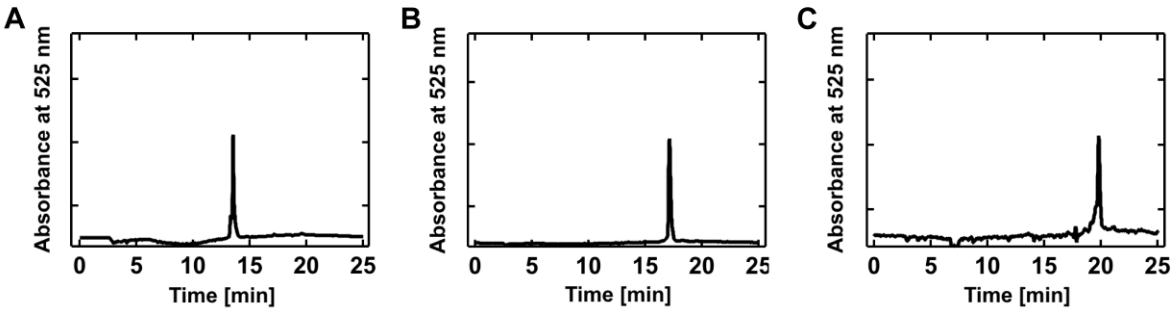

Figure S3.1: Typical HPLC chromatograms corresponding to the purification of A) Oligo1, B) Oligo2, and C) Oligo3. The DNA sequences of these macromolecules were 5'-$(A)_{10}(P)_n$-*S*-3', where the *A*, *P*, and *S* indicate the locations of the adenines, PTCDIs, and thiols, respectively, and *n* corresponds to the number of PTCDIs.

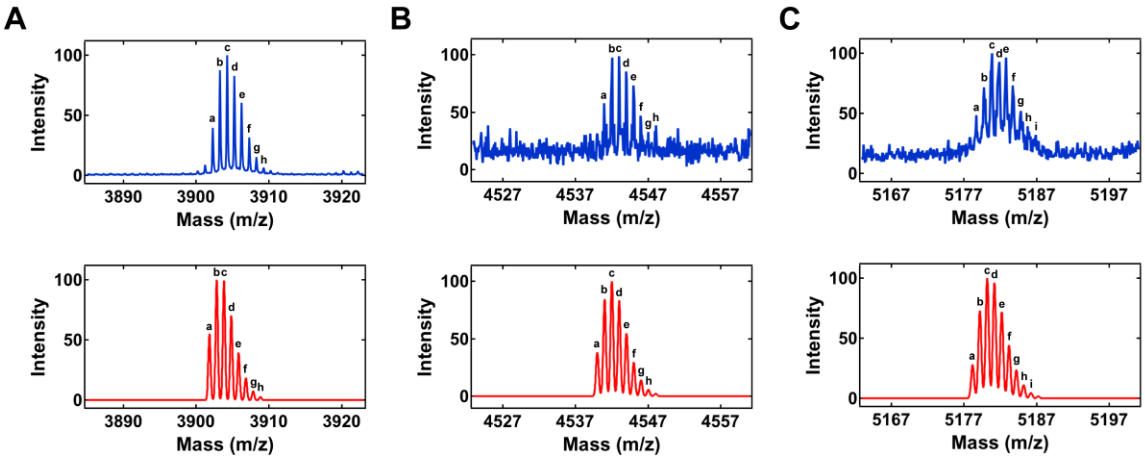

Figure S3.2: Experimental (top, blue) and simulated (bottom, red) MALDI TOF spectra corresponding to A) Oligo1, B) Oligo2, and C) Oligo3. The peaks in the experimental and simulated traces that correspond to one another are labeled with the same letter. The simulated spectra were obtained using AB Sciex Data Explorer. Note that the observed and expected masses are in good agreement. The DNA sequences of these macromolecules were 5'-$(A)_{10}(P)_n$-*S*-3', where the *A*, *P*, and *S* indicate the locations of the adenines, PTCDIs, and thiols, respectively, and *n* corresponds to the number of PTCDIs.

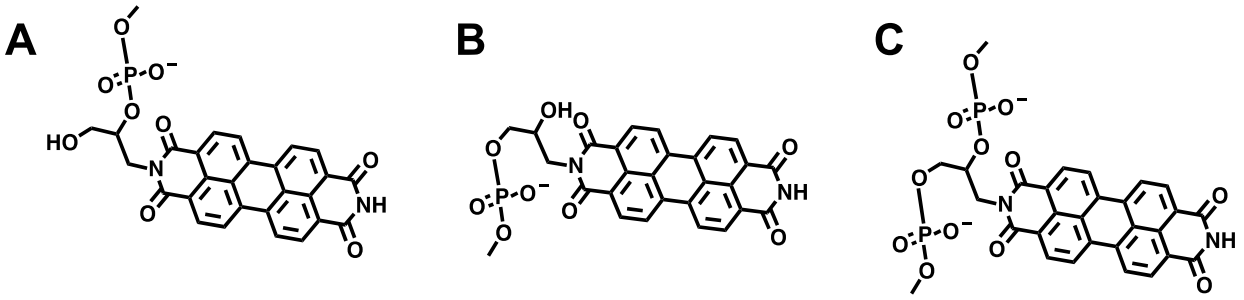

Figure S3.3: The chemical structure of the three PTCDI residues (along with the corresponding phosphate groups) that were designed and parameterized for the molecular dynamics simulations. The illustrations show A) the 5' terminal residue of **P2** and **P3**, B) the 3' terminal residue of **P2** and **P3,** and C) the middle residue of **P3**. When two residues are joined, one of the redundant phosphate groups will be removed to leave a single phosphate between the joined PTCDIs.

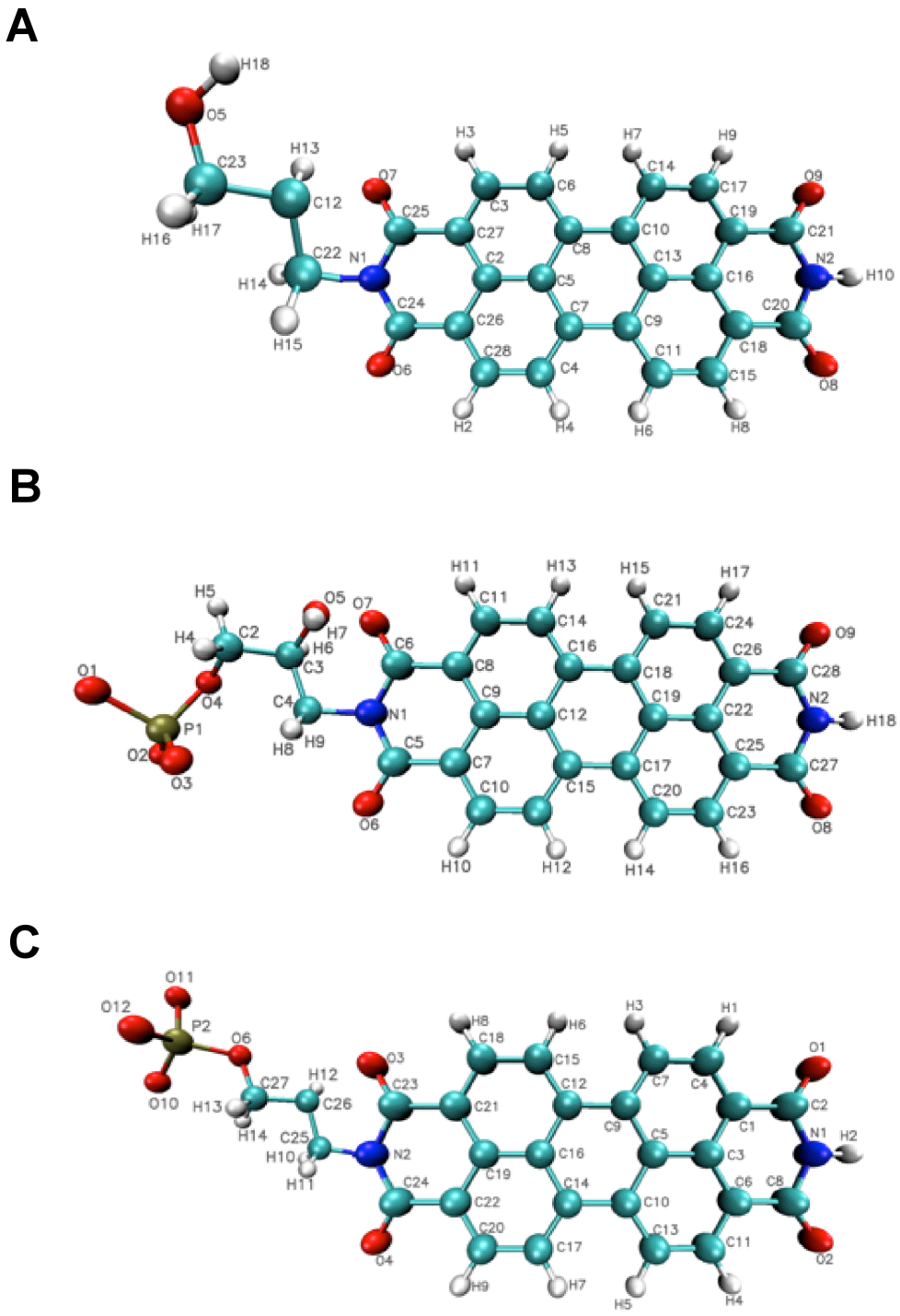

Figure S3.4: The structures of the three residues that were used to construct the multimeric PTCDI subunits for the molecular dynamics simulations. The illustrations show A) the 5' terminal residue of P2 and P3, B) the 3' terminal residue of P2 and P3, and C) the middle residue of P3. Note that some of the phosphate groups have been omitted for clarity. The labels on the atoms correspond to the atomic charges that are listed in Supporting Tables 3.1,3.2, and 3.3.

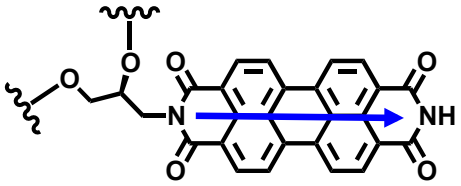

Figure S3.5: Illustration of the PTCDI DNA base surrogate. The blue line indicates the vector connecting the nitrogen closest to the backbone to the nitrogen furthest away from the backbone. The vector was used for analysis of the stacking of adjacent PTCDIs.

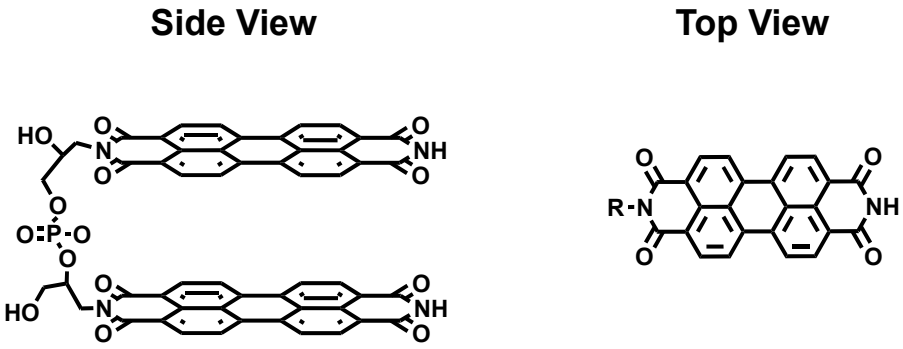

Figure S3.6: The side view (left) and top view (right) of the chemical structure of P2, where the two constituent PTCDIs feature a COM distance of ~ 3.4 Å and an offset angle of 0°. The top view, where the backbone has been removed for clarity, shows that the PTCDI moieties perfectly overlap in this scenario.

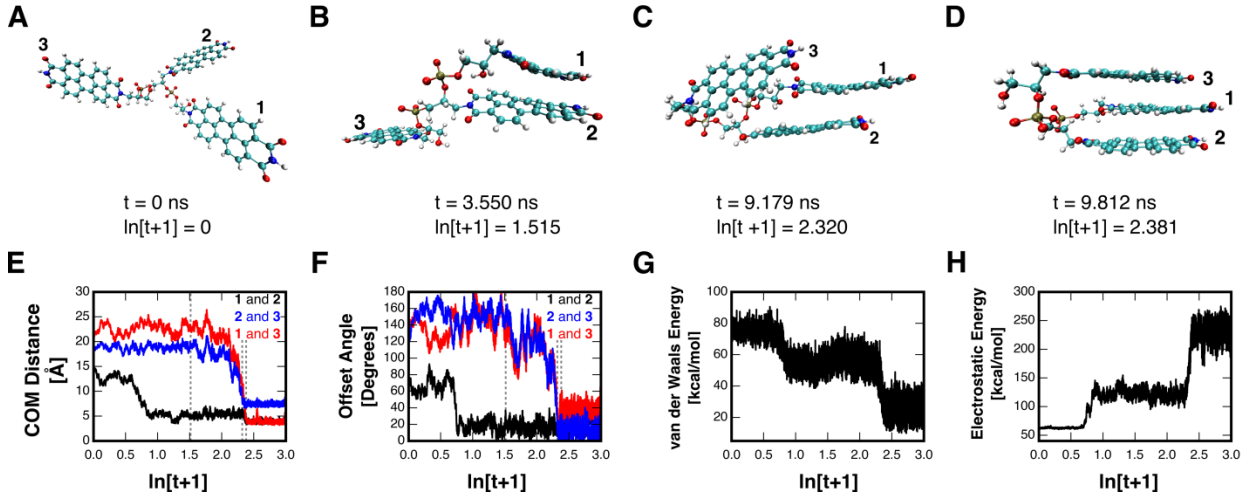

Figure S3.7: Assembly of P3 into a stacked configuration through a possible alternative pathway, as observed during molecular dynamics simulations. Note that this pathway is not physically likely when the PTCDIs are iteratively incorporated in an oligonucleotide. Snapshots of P3 at times of A) t = 0 ns, B) t = 3.550 ns, C) t = 9.179 ns, and D) t = 9.812 ns. The constituent PTCDIs of P3 are labeled as 1, 2, and 3. The sequence demonstrates the transition of P3 from an open random to a stacked configuration. E) The evolution of the centers of mass (COM) distance between PTCDIs 1 and 2 (black curve), PTCDIs 2 and 3 (blue curve), and PTCDIs 1 and 3 (red curve) as a function of time. (F) The evolution of the offset angle between PTCDIs 1 and 2 (black curve), PTCDIs 2 and 3 (blue curve), and PTCDIs 1 and 3 (red curve) as a function of time. G) The evolution of the van der Waals energy of P3 as a function of time. H) The evolution of the electrostatic energy of the PTCDIs' carbonyl oxygens distal to the alkane phosphate backbone as a function of time. The four vertical dashed lines in (E) and (F) correspond to the times used for the snapshots in A), B), C), and D). The simulations were performed at a constant temperature of 300 K.

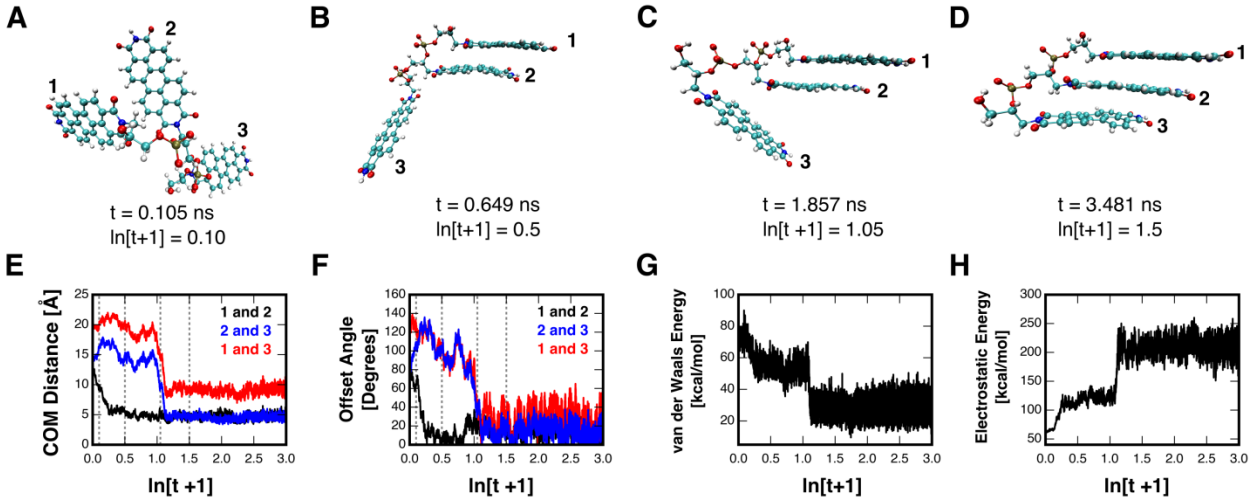

Figure S3.8: Assembly of P3 into a stacked configuration through another possible alternative pathway, as observed during molecular dynamics simulations. Snapshots of P3 at times of A) t = 0.105 ns, B) t = 0.649 ns, C) t = 1.857 ns, and D) t = 3.481 ns. The constituent PTCDIs of P3 are labeled as 1, 2, and 3. The sequence demonstrates the transition of P3 from an open random to a stacked configuration. E) The evolution of the centers of mass (COM) distance between PTCDIs 1 and 2 (black curve), PTCDIs 2 and 3 (blue curve), and PTCDIs 1 and 3 (red curve) as a function of time. (F) The evolution of the offset angle between PTCDIs 1 and 2 (black curve), PTCDIs 2 and 3 (blue curve), and PTCDIs 1 and 3 (red curve) as a function of time. G) The evolution of the van der Waals energy of P3 as a function of time. H) The evolution of the electrostatic energy of the PTCDIs' carbonyl oxygens distal to the alkane phosphate backbone as a function of time. The four vertical dashed lines in (E) and (F) correspond to the times used for the snapshots in A), B), C), and D). The simulations were performed at a constant temperature of 300 K.

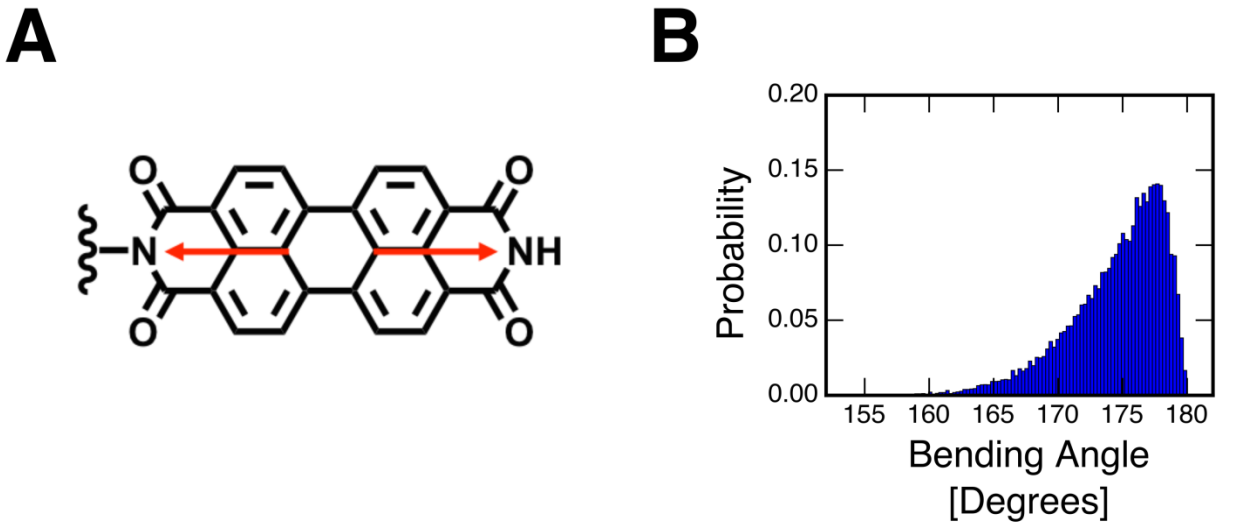

Figure S3.9: A) Structure of an isolated PTCDI moiety, where the vectors used to calculate the angle of bending are illustrated in red. B) The bending angle distribution of an individual PTCDI, the structure of which is shown in Figure S3.3A.

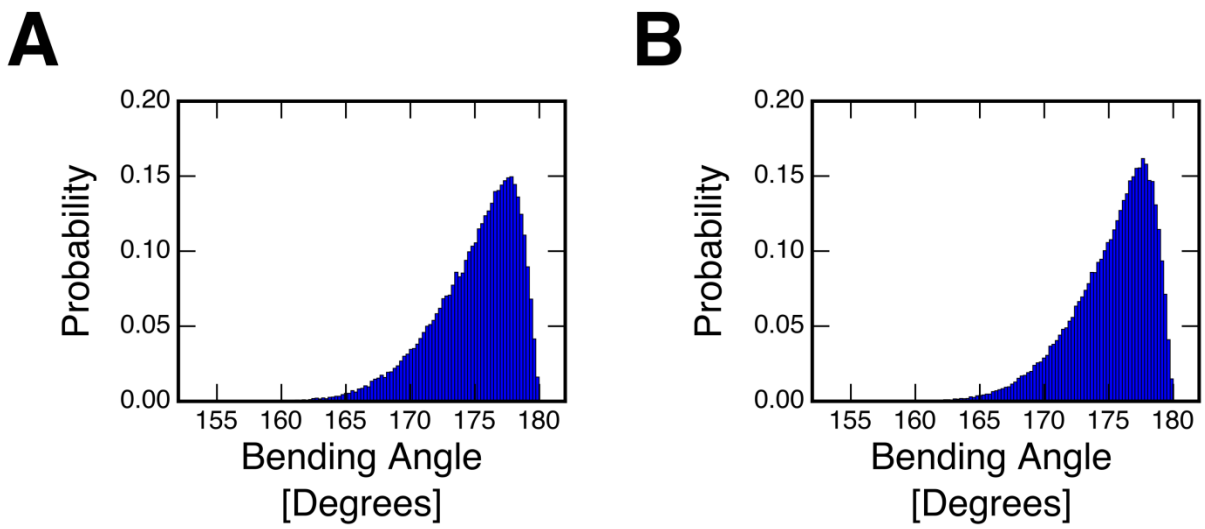

Figure S3.10: The bending angle distribution found for the A) 3' and B) 5' PTCDIs of P2. The data was obtained from the last 10 % of the conformation of a replica exchange simulation at 300 K.

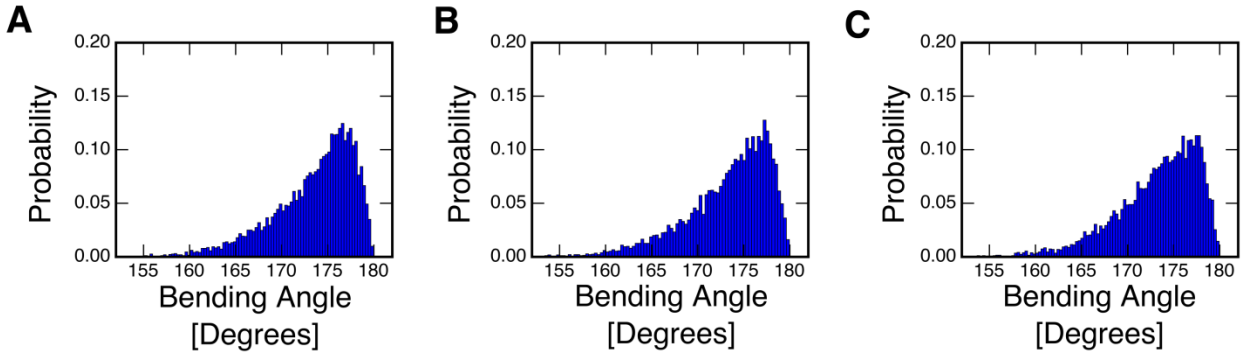

Figure S3.11: The bending angle distribution found for the A) 3' terminal B), middle, and C) 5' terminal PTCDIs of P3. The data was obtained from the last 10% of the conformations of a replica exchange simulation at 300 K.

Table S3.1: The atomic charges of the 3' terminal residue illustrated in Figure S3.4A.

Atom Number	Atom Name	AMBER Atom Type	Effective Charge
1	C2	ca	-0.0888
2	C3	ca	-0.0456
3	C4	ca	-0.2124
4	C5	ca	0.0511
5	C6	ca	-0.2124
6	C7	ca	0.0347
7	C8	ca	0.0347
8	C9	ca	0.0521
9	C10	ca	0.0521
10	C11	ca	-0.225
11	C12	c3	0.6377
12	C13	ca	0.071
13	C14	ca	-0.225
14	C15	ca	-0.0994
15	C16	ca	-0.0742
16	C17	ca	-0.0994
17	C18	ca	-0.0317
18	C19	ca	-0.0317
19	C20	c	0.5344
20	C21	c	0.5344
21	C22	c3	-0.1032
22	C23	c3	-0.0666
23	C24	c	0.4016
24	C25	c	0.4016
25	C26	ca	-0.0078
26	C27	ca	-0.0078
27	C28	ca	-0.0456
28	H2	ha	0.1488
29	H3	ha	0.1488
30	H4	ha	0.1535
31	H5	ha	0.1535
32	H6	ha	0.1636

33	H7	ha	0.1636
34	H8	ha	0.1626
35	H9	ha	0.1626
36	H10	hn	0.3092
37	H13	h1	-0.0746
38	H14	h1	0.0296
39	H15	h1	0.0296
40	H16	h1	0.0642
41	H17	h1	0.0642
42	H18	ho	0.4396
43	N1	n	-0.0169
44	N2	n	-0.4008
45	O5	oh	-0.6549
46	O6	o	-0.5047
47	O7	o	-0.5047
48	O8	o	-0.5559
49	O9	o	-0.5559

Table S3.2: The atomic charges of the 5' terminal residue illustrated in Supporting Figure S3.4B.

Atom Number	Atom Name	AMBER Atom Type	Effective Charge
1	O1	os	-0.5232
2	P1	p5	1.1659
3	O2	o	-0.7761
4	O3	o	-0.7761
5	O4	os	-0.4954
6	C2	c3	0.1667
7	C3	c3	-0.0883
8	O5	oh	-0.6318
9	C4	c3	-0.2541
10	N1	n	-0.071
11	C5	c	0.4532
12	C6	c	0.4532
13	C7	ca	-0.0127
14	O6	o	-0.5055
15	C8	ca	-0.0127
16	O7	o	-0.5055
17	C9	ca	-0.0391
18	C10	ca	-0.0924
19	C11	ca	-0.0924
20	C12	ca	0.0699
21	C13	ca	-0.2137
22	C14	ca	-0.2137
23	C15	ca	0.0235
24	C16	ca	0.0235
25	C17	ca	0.0416
26	C18	ca	0.0416
27	C19	ca	0.0841
28	C20	ca	-0.2295
29	C21	ca	-0.2295
30	C22	ca	-0.0552
31	C23	ca	-0.102
32	C24	ca	-0.102

33	C25	ca	-0.0117
34	C26	ca	-0.0117
35	C27	c	0.4712
36	C28	c	0.4712
37	O8	o	-0.5398
38	N2	n	-0.3174
39	O9	o	-0.5398
40	H4	h1	0.0494
41	H5	h1	0.0494
42	H6	h1	0.2217
43	H7	ho	0.4422
44	H8	h1	0.1949
45	H9	h1	0.1949
46	H10	ha	0.1547
47	H11	ha	0.1547
48	H12	ha	0.1631
49	H13	ha	0.1631
50	H14	ha	0.1641
51	H15	ha	0.1641
52	H16	ha	0.1674
53	H17	ha	0.1674
54	H18	hn	0.292

Table S3.3: The atomic charges of the middle residue illustrated in Figure S3.4C.

Atom Number	Atom Name	AMBER Atom Type	Effective Charge
1	C1	ca	-0.0409
2	C2	c	0.5298
3	C3	ca	-0.0773
4	C4	ca	-0.108
5	N1	n	-0.3968
6	O1	o	-0.5729
7	C5	ca	0.0699
8	C6	ca	-0.0409
9	C7	ca	-0.2334
10	C8	c	0.5298
11	C9	ca	0.0646
12	C10	ca	0.0646
13	C11	ca	-0.108
14	O2	o	-0.5729
15	C12	ca	0.0245
16	C13	ca	-0.2334
17	C14	ca	0.0245
18	C15	ca	-0.202
19	C16	ca	0.0376
20	C17	ca	-0.202
21	C18	ca	-0.0978
22	C19	ca	-0.0294
23	C20	ca	-0.0978
24	C21	ca	0.0322
25	C22	ca	0.0322
26	C23	c	0.4872
27	C24	c	0.4872
28	N2	n	-0.2338
29	O3	o	-0.525
30	O4	o	-0.525
31	C25	c3	-0.0469
32	C26	c3	0.6987

33	C27	c3	0.0421
34	O6	os	-0.5232
35	P2	p5	1.1659
36	O10	o	-0.7761
37	O11	o	-0.7761
38	O12	os	-0.4954
39	H1	ha	0.1611
40	H2	hn	0.3022
41	H3	ha	0.1543
42	H4	ha	0.1611
43	H5	ha	0.1543
44	H6	ha	0.1521
45	H7	ha	0.1521
46	H8	ha	0.1538
47	H9	ha	0.1538
48	H10	h1	0.0268
49	H11	h1	0.0268
50	H12	h1	-0.0409
51	H13	h1	0.0222
52	H14	h1	0.0222

3.7 References

1. Herbst, W.; Hunger, K. *Industrial Organic Pigments: Production, Properties, Applications*, 2nd ed.; Wiley: Weinheim, **1997**.
2. Würthner, F. *Chem. Commun*. **2004**, 1564– 1579
3. Li, C.; Wonneberger, H. *Adv. Mater*. **2012**, 24, 613– 636
4. Görl, D.; Zhang, X.; Würthner, F. *Angew. Chem., Int. Ed*. **2012**, 51, 6328– 6348
5. Geng, Y.; Li, H.-B.; Wu, S.-X.; Su, Z.-M. *J. Mater. Chem*. **2012**, 22, 20840– 20851
6. Kozma, E.; Catellani, M. *Dyes Pigm*. **2013**, 98, 160– 179
7. Jung, B. J.; Tremblay, N. J.; Yeh, M.-L.; Katz, H. E. *Chem. Mater*. **2011**, 23, 568– 582
8. Huang, C.; Barlow, S.; Marder, S. R. *J. Org. Chem*. **2011**, 76, 2386– 2407
9. Vura-Weis, J.; Ratner, M. A.; Wasielewski, M. R. *J. Am. Chem. Soc*. **2010**, 132, 1738– 1739
10. Delgado, M. C. R.; Kim, E.-G.; da Silva Filho, D. A.; Bredas, J.-L. *J. Am. Chem. Soc*. **2010**, 132, 3375– 3387
11. Marcon, V.; Breiby, D. W.; Pisula, W.; Dahl, J.; Kirkpatrick, J.; Patwardhan, S.; Grozema, F.; Andrienko, D. *J. Am. Chem. Soc*. **2009**, 131, 11426– 11432
12. May, F.; Marcon, V.; Hansen, M. R.; Grozema, F.; Andrienko, D. *J. Mater. Chem*. **2011**, 21, 9538– 9545
13. Idé, J.; Méreau, R.; Ducasse, L.; Castet, F.; Olivier, Y.; Martinelli, N.; Cornil, J.; Beljonne, D. *J. Phys. Chem. B* **2011**, 115, 5593– 5603
14. Teklebrhan, R. B.; Ge, L.; Bhattacharjee, S.; Xu, Z.; Sjöblom, J. *J. Phys. Chem. B* **2012**, 116, 5907– 5918
15. Wagner, C.; Wagenknecht, H.-A. *Org. Lett*. **2006**, 8, 4191– 4194
16. Baumstark, D.; Wagenknecht, H.-A. *Chem. - Eur. J*. **2008**, 14, 6640– 6645
17. Baumstark, D.; Wagenknecht, H.-A. *Angew. Chem., Int. Ed*. **2008**, 47, 2612– 2614
18. Menacher, F.; Wagenknecht, H.-A. *Eur. J. Org. Chem*. **2011**, 24, 4564– 4570
19. Menacher, F.; Wagenknecht, H.-A. *Photochem. Photobiol. Sci.* **2011**, 10, 1275– 1278
20. Menacher, F.; Stepanenko, V.; Würthner, F.; Wagenknecht, H.- A. *Chem. - Eur. J*. **2011**, 17, 6683– 6688
21. Zheng, Y.; Long, H.; Schatz, G. C.; Lewis, F. D. *Chem. Commun*. **2005**, 38, 4795– 4797
22. Hariharan, M.; Zheng, Y.; Long, H.; Zeidan, T. A.; Schatz, G. C.; Vura-Weis, J.; Wasielewski, M. R.; Zuo, X.; Tiede, D. M.; Lewis, F. D. *J. Am. Chem. Soc.* **2009**, 131, 5920– 5929
23. Zeidan, T. A.; Carmieli, R.; Kelley, R. F.; Wilson, T. M.; Lewis, F. D.; Wasielewski, M. R. *J. Am. Chem. Soc*. **2008**, 130, 13945– 13955
24. Carmieli, R.; Zeidan, T. A.; Kelley, R. F.; Mi, Q.; Lewis, F. D.; Wasielewski, M. R. *J. Phys. Chem. A* **2009**, 113, 4691– 4700
25. Wilson, T. M.; Zeidan, T. A.; Hariharan, M.; Lewis, F. D.; Wasielewski, M. R. *Angew. Chem., Int. Ed*. **2010**, 49, 2385– 2388
26. Wohlgamuth, C. H.; McWilliams, M.; Mazaheripour, A.; Burke, A.; Lin, K.-Y.; Doan, L.; Slinker, J. P.; Gorodetsky, A. A. *J. Phys. Chem. C* **2014**, 118, 29084– 29090
27. Cieplak, P.; Cornell, W. D.; Bayly, C.; Kollman, P. A. *J. Comput. Chem*. **1995**, 16, 1357– 1377

28. Frisch, M. J.; Trucks, G. W.; Schlegel, H. B.; Scuseria, G. E.; Robb, M. A.; Cheeseman, J. R.; Scalmani, G.; Barone, V.; Mennucci, B.; Petersson, G. A.; et al. Gaussian 09, Revision A.1; Gaussian, Inc.: Wallingford, CT, **2009**.
29. Wang, J.; Wolf, R. M.; Caldwell, J. W.; Kollman, P. A.; Case, D. A. *J. Comput. Chem*. **2004**, 25, 1157– 1174
30. Jakalian, A.; Bush, B. L.; Jack, D. B.; Bayly, C. I. *J. Comput. Chem*. **2000**, 21, 132– 146
31. Jakalian, A.; Jack, D. B.; Bayly, C. I. *J. Comput. Chem*. **2002**, 23, 1623– 1641
32. Darden, T. A.; Cheatham, T. E., III; Simmerling, C. L.; Wang, J.; Duke, R. E.; Luo, R.; Walker, R. C.; Zhang, W.; Merz, K. M.; Roberts, B. et al. Amber 12; University of California: San Francisco, CA, **2012**.
33. Phillips, J. C.; Braun, R.; Wang, W.; Gumbart, J.; Tajkhorshid, E.; Villa, E.; Chipot, C.; Skeel, R. D.; Kalé, L.; Schulten, K. *J. Comput. Chem*. **2005**, 26, 1781– 1802
34. Sugita, Y.; Okamoto, Y. *Chem. Phys. Lett*. **1999**, 314, 141– 151
35. Shirts, M. R.; Chodera, J. D. *J. Chem. Phys*. **2008**, 129, 124105– 124118
36. Clark, A. E.; Qin, C.; Li, A. D. Q. *J. Am. Chem. Soc*. **2007**, 129, 7586– 7595

CHAPTER 4 Consequences of Electronic Structure Evolution for Bioinspired Perylenediimide Ensembles

4.1 Abstract

Carbon-based materials have undergone remarkable advances within the past two decades and are viewed as successors to silicon in miniaturized electronic devices. Thus, considerable research effort has been devoted to elucidating structure-function relationships and charge transport phenomena for organic semiconductors. However, the construction and experimental evaluation of precisely defined model systems, which emulate the properties of aromatic, π-stacked organic semiconductors at the nanoscale, remains as an important unmet challenge. Herein, we address this challenge through the rational design, preparation, and characterization of a novel and unprecedented class of DNA-inspired organic semiconductor model systems. We find that these systems exhibit an evolution in their electronic structure, which is accompanied by unexpected and surprising changes in their core-level exciton dissociation times. Our findings hold broad general relevance for understanding structure-function relationships in arbitrary organic electronic materials, nanoscale charge transfer phenomena at device-relevant organic/inorganic interfaces, and electrical conductivity in biological and bioinspired systems.

4.2 Introduction

Organic semiconductors have been touted as the next generation of electronic materials, with the potential to replace more traditional inorganic variants, and as such, they have witnessed tremendous advances within the past two decades.[1-15] As an example, the performance of organic transistors has improved dramatically, with state-of-the-art carrier mobilities greater than 10

$cm^2/V•s$ exceeding ones of approximately 1 $cm^2/V•s$ reported for amorphous silicon.[1, 2] At the same time, the efficiencies of organic photovoltaic cells have jumped from values of ~ 2 – 3 % to commercially relevant values of 10 % or greater.[3, 4] These once tantalizing advances have been driven in large part by the development of an improved fundamental understanding of structure-function relationships and fundamental charge transport phenomena in a broad range of organic semiconductors.[1-15] However, despite this progress, the rational and predictive molecular engineering of π-stacked organic semiconductors for specific functionality remains difficult and elusive.

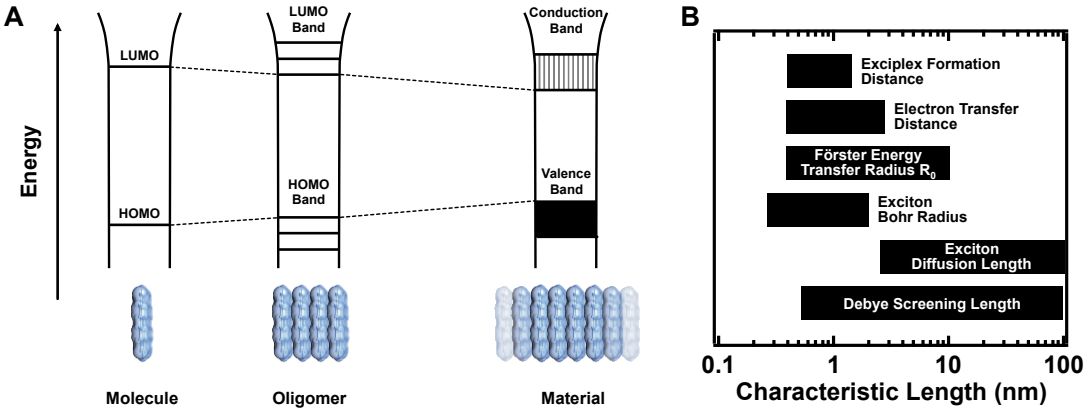

Figure 4.1: Consequences of electronic structure evolution for organic semiconductors. (A) Energy diagram depicting the change in electronic structure that accompanies the transition of a molecule into an extended material. The initial molecule (left) features well-defined HOMO and LUMO energy levels, the oligomer (middle) features multiple closely spaced energy levels, and the extended material (right) features a band-like electronic structure. (B) The characteristic length scales associated various phenomena in organic semiconductor nanostructures. The image has been adapted from reference 11.

The difficulties inherent to the *a priori* rational design of superior organic semiconductors can be visualized by considering the evolution in electronic structure accompanying the transition of an isolated molecule into an extended solid.[8-15] The transition is illustrated for a prototypical one-dimensional organic semiconductor in Figure 4.1A. For this

material, the initial isolated molecular building block features distinct lowest unoccupied molecular orbital (LUMO) and highest occupied molecular orbital (HOMO) energy levels (Figure 4.1A, left). As multimeric ensembles are formed from the isolated molecules, non-covalent intermolecular interactions and wave function overlap induce the formation of multiple closely spaced energy levels (Fig. 4.1A, middle). Eventually, the incorporation of additional building blocks furnishes a semi-infinite one-dimensional chain with a band-like electronic structure, where the effective valence and conduction bands possess a finite width (Figure 4.1A, right). For each of the distinct length scales associated with these three regimes, organic semiconductors often possess radically different behavior and properties[8-15], making it nearly impossible to establish and refine a set of design guidelines that predict functionality in any specific context.

From the perspective of rational organic semiconductor design, the intermediate multimeric ensembles hold particular relevance because the associated size regime of ~ 1 to ~ 5 nm encompasses many phenomena that ultimately determine device functionality (exciplex formation, electron transfer Förster energy transfer, exciton generation, and exciton Bohr radius, among others).[11] Indeed, the study of such ensembles has remained notoriously difficult for several reasons.[1-15] First, traditional self-assembly or fabrication techniques are poorly suited for the preparation of general model systems where the length and molecular building block sequence are well defined. Second, the weak short-range non-covalent interactions that govern the properties of such systems are notoriously difficult to enforce and control reliably, with even subtle changes in the interactions yielding dramatic and unexpected effects. Third, the intermediate regime cannot be readily isolated and studied at the crucial device-relevant material interfaces, especially with the requisite chemical, temporal, and spatial resolution. Thus, a

general methodology for the construction and experimental evaluation of precisely defined constructs, which emulate the properties of organic semiconductors at the crucial intermediate size regime, remains as an important unmet grand challenge.

Herein, we address this challenge and describe the rational design, preparation, and characterization of a novel and unprecedented class of rationally designed organic semiconductor ensembles. First, we use classic automated oligonucleotide chemistry protocols to synthesize a series of DNA-like model systems from soluble perylene-3,4,9,10-tetracarboxylic diimide (PTCDI)-based phosphoramidite building blocks. We characterize these macromolecules with UV-visible absorbance spectroscopy and mass spectrometry, as well as explore their likely solution-phase conformations with molecular dynamics simulations. We next self-assemble our constructs into monolayers and interrogate their electronic properties with a synergistic combination of X-ray spectroscopy, electrochemistry, and density functional theory. We subsequently investigate the monolayers with resonant photoemission spectroscopy, quantifying our constructs' intrinsic core-level exciton dissociation times at solid substrates. These measurements indicate an unexpected and surprising trend in the dissociation times, which would be difficult to predict *a priori.* In its totality, the presented general methodology may provide unprecedented opportunities for fundamentally understanding structure-function relationships and charge transport phenomena in a broad range of organic, biological, and bioinspired systems.

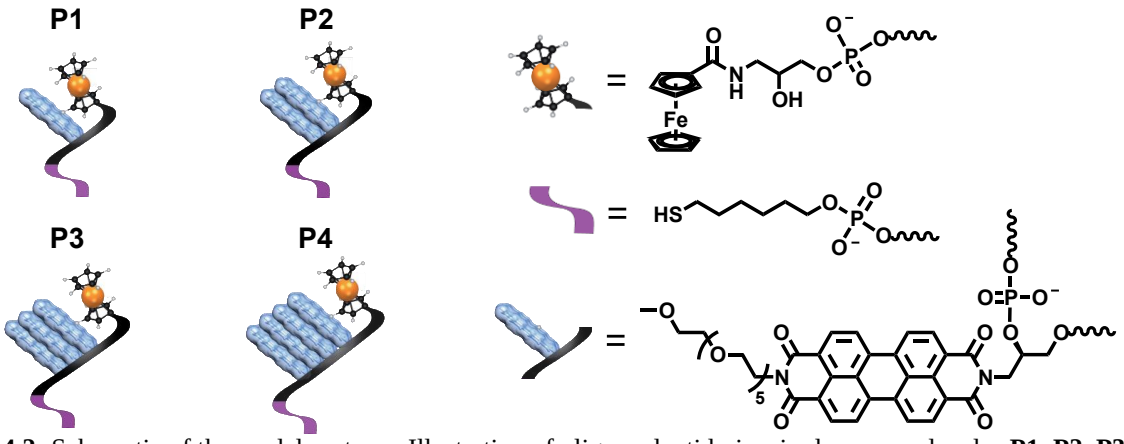

Figure 4.2: Schematic of the model systems. Illustration of oligonucleotide-inspired macromolecules **P1**, **P2**, **P3**, and **P4**, which feature terminal thiol and ferrocene moieties, as well as tracts of one, two, three, or four PTCDIs, respectively.

4.3 Experimental

4.3.1 Materials

All chemical reagents were purchased from Acros Organics, Sigma-Aldrich, or Combi-Blocks. The solvents were obtained from Fisher Scientific and used as received, unless otherwise noted. Flash chromatography was performed using SiliCycle Silica Flash F60 silica gel. The chemical reagents and commercial phosphoramidites required for the synthetic of the PTCDI-based macromolecules were purchased from either Glen Research, Inc. or FIVEphoton Biochemicals and used as received.

4.3.2 Characterization of the Small Molecule Precursors

All intermediates and products for the phosphoramidite synthesis were characterized with nuclear magnetic resonance (NMR) spectroscopy and mass spectrometry. The electrospray mass spectrometry (ESI MS) data were obtained at the University of California, Irvine Mass Spectrometry Facility on a Waters LCT Premier electrospray time-of-flight instrument. The ^{1}H NMR spectra were obtained on either a Bruker DRX500 or an AVANCE600 instrument. The ^{13}C

NMR spectra were obtained on a Bruker DRX500 outfitted with a CryoProbe (Bruker TCI 500 MHz, 5 mm diameter tubes). The ^{31}P NMR spectra were acquired on a Bruker AVANCE instrument. Chemical shifts were reported in ppm for ^{1}H, ^{13}C, and ^{31}P NMR. The chemical shifts for the NMR data were referenced as follows: for samples in $CDCl_3$, the ^{1}H NMR was referenced to tetramethylsilane (TMS) at 0.00, and the ^{13}C NMR was referenced to $CDCl_3$ at 77.23; for samples in CD_3OD, the ^{13}C NMR was referenced to the solvent peak at 49.00; for samples in CD_2Cl_2, the ^{1}H NMR was referenced to the solvent peak at 5.32, and the ^{13}C NMR was referenced to the solvent peak at 54.00. The chemical shifts for the ^{31}P NMR spectra were corrected and referenced by using ^{1}H NMR according to the 2008 IUPAC recommendations.[61] The data are labeled as follows: chemical shift, multiplicity (s = singlet, d = doublet, t = triplet, q = quartet, quint = quintet, m = multiplet, br s = broad singlet), the coupling constants (in Hertz), and the integration value.

4.3.3 Synthesis, Purification, and Characterization of the PTCDI-Based Macromolecules

The macromolecules **P1**, **P2**, **P3**, and **P4** were synthesized on solid support according to standard commercial protocols recommended by Glen Research, Inc. for an Applied Biosystems (ABI) 394 DNA synthesizer. The synthesis cycle was modified to omit the capping step and to use extended coupling times for the incorporation of both the thiol modifier C6 S-S phosphoramidites and perylenediimide phosphoramidites, as previously described.[22, 23] After synthesis, the macromolecules were cleaved from the support by treatment with aqueous ammonium hydroxide and purified *via* reverse phase high performance liquid chromatography (HPLC) on an Agilent 1260 Infinity system. The macromolecules were eluted with a gradient evolved from 40% solvent A and 60% solvent B to 0% solvent A and 100% solvent B over 120

min at a flow rate of 1 mL/min (solvent A, 50 mM ammonium acetate, pH = 6 buffer; solvent B, methanol) on Agilent ZORBAX Stable Bond Phenyl columns (see Figure S4.1 for representative chromatograms). The UV−visible (UV−vis) absorption spectra of the macromolecules were obtained with an Agilent 1260 Infinity Series diode array detector during chromatographic purification (see Figure S4.2 for representative spectra). The MALDI-TOF mass spectra of the macromolecules were obtained on an Applied Biosystems Sciex MALDI-TOF/TOF 5800 series mass spectrometer in reflectron negative mode, using a 349 nm Nd:YAG laser as the illumination source (see Figure S4.3 for representative spectra).

4.3.4 Molecular Dynamics Simulations for the PTCDI-Based Macromolecules

The molecular dynamics simulations for macromolecules **P1**, **P2**, **P3**, and **P4** were performed with GAFF in NAMD 2.9. The simulations employed the Generalized Born Implicit Solvent model (GBIS) and a monovalent salt concentration of 0.115 M. For the simulations, the subunits of **P1**, **P2**, **P3**, and **P4**, as illustrated in Figure S4.4, were parametrized according to established literature protocols[23] and were in turn used for the molecular dynamics simulations. For each simulation, the starting configuration was obtained by turning off the attractive van der Waals interactions in the force field and setting the temperature to 500 K, thereby ensuring that all PTCDI moieties were completely separated from one another in an unstacked random open configuration. To initiate the simulation, the attractive van der Waals interactions were turned on and the initial temperature was set to 300 K. All of the simulations were performed at a constant temperature of 300 K for 20 ns, ensuring that steady state was reached. The simulations were analyzed by monitoring the relative center of mass (COM) distances and offset angles for every pair of PTCDIs.[23] The COM distances were calculated from the atomic coordinates and atomic

mass of the individual PTCDIs. Here, the offset angles were obtained by constructing a vector from the nitrogen closest to the backbone to the nitrogen farthest from the backbone for the individual PTCDIs. The dot product of these vectors for every pair of PTCDIs defined the offset angles used for the analysis. The COM distances and offset angles indicated the relative separation and alignment of the PTCDIs, respectively.

4.3.5 Density-Functional Theory Calculations for the PTCDI-Based Macromolecules

Ground state density functional theory calculations for the subunits of macromolecules **P1**, **P2**, **P3**, and **P4** (Figure S4.4) were performed in Gaussian 09.[42] The averaged structures from the molecular dynamics simulations were used for the subunit geometries. The atomic orbitals were expanded in the cc-pVTZ and 6-31G(d,p) basis sets, and the ground state calculations were performed with all combinations of the aforementioned basis sets, as well as the CAM-B3LYP,[41] B3LYP, and LC-wPBE functionals. The reported trends in the HOMO/LUMO energies and molecular orbitals were observed for all combinations of functionals and basis sets. The molecular orbitals were obtained in Gaussian 09 for the HOMO, HOMO-1, HOMO-2, HOMO-3, LUMO, LUMO+1, LUMO+2, and LUMO+3 of each PTCDI-based macromolecule. The isosurface plots were rendered in VESTA.[62]

4.3.6 Self-Assembly of Mixed Monolayers from the PTCDI-Based Macromolecules and Multilayers from the Small Molecules

Monolayers from macromolecules **P1**, **P2**, **P3**, and **P4** were formed on polycrystalline gold rod electrodes (Ø = 2 mm; CH Instruments) or on 80 nm gold (111) films evaporated onto Si (100) substrates (International Wafer Service). The macromolecules were self-assembled from

methanol over a period of 16 to 24 hours. The monolayers were in turn backfilled with mercaptohexanol over a period of 5 to 70 minutes, displacing non-specifically bound macromolecules. The PTCDI multilayers were prepared by dropcasting PTCDI **S1** (Figure S4.13) onto gold-coated Si (100) substrates. The monolayers and multilayers were used immediately for electrochemical or spectroscopic measurements.

4.3.7 Electrochemistry of Mixed Monolayers from the PTCDI-Based Macromolecules

Cyclic voltammetry (CV) experiments were performed in a standard three-electrode electrochemical cell with a CHI832C Electrochemical Analyzer (CH Instruments). In a typical experiment, a gold rod electrode (CH Instruments) modified with the relevant mixed monolayer served as the working electrode, a coiled platinum wire (ThermoFisher) served as the counter electrode, and a commercial Ag/AgCl electrode (1 M KCl, CH Instruments) served as the reference electrode. The electrochemical measurements were performed under an inert argon atmosphere in aqueous 0.1 M sodium perchlorate, 2.5 mM sodium phosphate, pH = 7 buffer.

4.3.8 X-ray Spectroscopy of PTCDI-Based Mixed Monolayers and Multilayers

X-ray spectroscopy experiments were performed at the ALOISA beamline of the Elettra Synchrotron in Trieste, Italy in an ultra-high vacuum end station. During the experiments, the sample temperature was maintained at –60 °C, and the measurement and sample preparation chamber pressures were maintained at 10^{-11} mbar and 10^{-10} mbar, respectively. The mixed monolayers and multilayers were characterized using X-ray photoelectron spectroscopy (XPS), near edge X-ray absorption fine structure spectroscopy (NEXAFS) and resonant photoemission spectroscopy (RPES). The XPS measurements were performed at a grazing-incidence angle of 4°

using X-rays with an energy of 140 – 650 eV, a resolution ΔE = 60-200 meV, and an electric field vector perpendicular to the surface (P-polarization). The emitted photoelectrons were collected with a hemispherical electron analyzer positioned normal to the sample at an acceptance angle of 2° and a pass energy of E_p = 10–20 eV (resolution $\Delta E/E_p$ = 1%). The energy scale for the XPS spectra was calibrated by aligning the Au $4f_{7/2}$ peak of the Au substrate to a binding energy of 84 eV relative to the Fermi level. The NEXAFS measurements were performed in Partial Electron Yield mode at a grazing-incidence angle of 6° and with the high pass kinetic energy filter set to 250 eV. The resulting spectra were normalized with respect to the beam current measured on the gold coating of the last refocusing mirror. The RPES experiments were performed by taking XPS scans (0 to 50 eV binding energy, E_p = 40 eV) at a series of incident photon energies across the entire range of the carbon K-edge ionization threshold (278 eV to 310 eV). The surface was oriented at a grazing-incidence angle of 4˚ and in P-polarization, with the electron analyzer positioned at 55° from the surface normal. The data obtained for all of the measurements was processed according to established literature procedures.[44-53]

4.4 Results and Discussion

We began our studies by drawing inspiration from the structure of DNA and rationally designing the series of model systems illustrated in Figure 4.2. These macromolecules consisted of length-variable tracts of π-conjugated PTCDI building blocks appended to an alkane phosphodiester backbone, as well as alkanethiol and ferrocene functionalities at opposing termini. As the key building block for our constructs, we specifically chose the classic PTCDI moiety because its electronic properties, electrochemical behavior, intermolecular interactions, and self-assembly characteristics have all been extensively explored.[16-18] Moreover, PTCDIs

have shown excellent chemical modularity and have even been integrated within DNA as multi-functional fluorescent and electrochemical probes.[9-23] Here, within the context of our overall design, the alkanethiols were included to facilitate binding to gold surfaces for the controlled formation of ordered self-assembled monolayers,[24-26] and the ferrocene redox probes were included to serve as an internal standard for electrochemical measurements.[27] We hypothesized that such modular, multi-functional constructs could be readily studied with a suite of complementary spectroscopic and electrochemical measurements.

As the first step in the preparation of our target constructs, we synthesized the new soluble PTCDI phosphoramidite **3** illustrated in Scheme 4.1A.[19-23] This building block specifically incorporated a polyethylene glycol (PEG) imide substituent to mitigate the solubility and aggregation issues that plague perylenediimide derivatives. In brief, we first obtained bisimide **2** by refluxing perylene-3,4,9,10-tetracarboxylic dianhydride with (S)-3-amino-1,2-propanediol and aminohexaethylene glycol monomethyl ether **1**. We next coupled the free hydroxyl group of **2** to a chlorophosphoramidite, furnishing **3**. Importantly, unlike analogous PTCDI phosphoramidites,[19-23] **3** was readily soluble in neat acetonitrile at high concentrations, facilitating the subsequent construction of the desired macromolecules on an automated DNA synthesizer.

We next prepared and purified the four macromolecules in Figure 4.2, denoted as **P1**, **P2**, **P3**, and **P4** (and labeled according to the number of PTCDI moieties) *via* oligonucleotide synthesis techniques (Scheme 4.1B).[28, 29] Specifically, we used an automated oligonucleotide synthesizer to sequentially couple one to four PTCDI building blocks, as well as a thiol phosphoramidite, to a ferrocene-modified controlled pore glass solid support. We subsequently cleaved our materials from the solid support and purified them with high performance liquid

chromatography (HPLC) under semi-aqueous conditions used for natural oligonucleotides (Figure S4.1). The resulting constructs were further characterized with UV-visible spectroscopy and matrix assisted laser desorption/ionization time-of-flight (MALDI-TOF) mass spectrometry (Figures S4.2 and S4.3). Here, we note that this straightforward and rapid procedure was only made possible by the enhanced solubility of the rationally designed PTCDI phosphoramidite **3**. Overall, our approach uniquely leveraged classic biochemistry protocols to furnish a series of unprecedented, sequence-variable organic semiconductor model systems that would not be accessible through any other means.

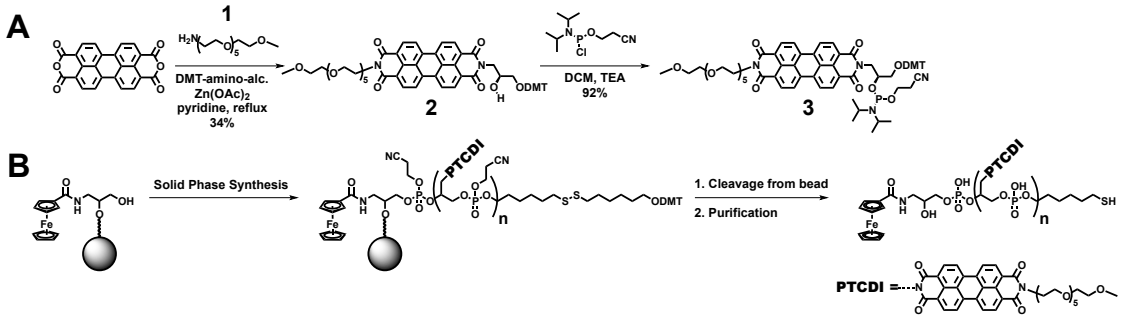

Scheme 4.1: Synthesis of the model systems (A) Synthesis of phosphoramidite **3**. (B) Automated synthesis of macromolecules **P1**-**P4**.

With our macromolecules in hand, we sought to gain insight into their molecular conformations by performing molecular dynamics simulations for **P1**, **P2**, **P3**, and **P4**. To capture our molecules' likely geometries, we employed previously reported literature protocols and investigated the assembly of only the constructs' PTCDI-containing substructures (without the alkanethiol and ferrocene functionalities) (Figure S4.4).[23] The simulations revealed that the most thermodynamically stable and lowest free energy conformations featured strong interactions between the PTCDI moieties of **P2**, **P3**, and **P4** (Figure 4.3). Here, to maximize $\pi-\pi$ interactions between the PTCDIs' aromatic cores and minimize the electrostatic repulsion

between the PTCDIs' carbonyl groups, **P2**, **P3**, and **P4** appeared to adopt a twisted arrangement, where the constituent PTCDIs were stacked but offset with respect to each another (Figure 4.3). By analyzing these structures, we found that **P2** featured an average center of mass distance of ~ 4.9 Å and an average offset angle of 10.4°, **P3** featured an average center of mass distance of ~ 4.6 Å and an average offset angle of ~16.8°, and **P4** featured an average center of mass distance of ~ 4.7 Å and an average offset angle of ~ 13.0°. The observed structural arrangement was in excellent agreement with our previous findings for DNA-integrated PTCDIs[23] and effectively mimicked the complex behavior and packing found for various PTCDI derivatives in the solid state.[18]

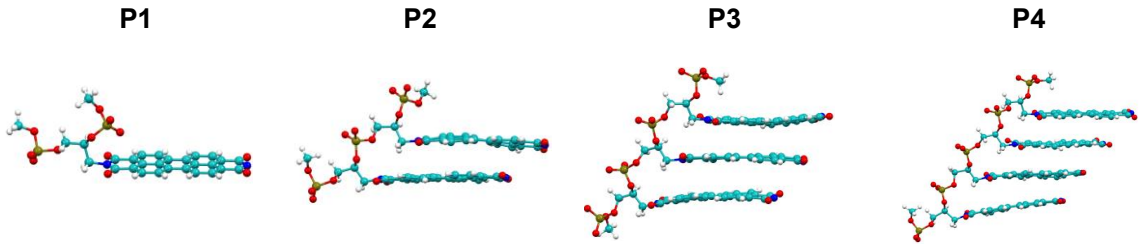

Figure 4.3: Equilibrium conformations of the model systems. Snapshots of the PTCDI-containing subunits of **P1, P2, P3,** and **P4**, as taken from molecular dynamics simulations after reaching steady state. The snapshots reveal that the PTCDIs adopt a stacked arrangement.

To facilitate the subsequent experiments, we self-assembled monolayers from **P1**, **P2**, **P3**, and **P4**, as illustrated for **P1** in Figre 4.4. This approach was advantageous because it enabled direct correlation and comparison of electrochemical and X-ray spectroscopic measurements within a single unified context. Here, to form the monolayers, we incubated clean gold substrates with solutions of our thiol-modified constructs, allowing for formation of covalent S-Au bonds.[24-26] The substrates were in turn treated with mercaptohexanol to displace non-specifically bound species and help enforce an upright orientation for the covalently bound

macromolecules.[25, 30, 31] The resulting mixed monolayers, which were effectively comprised of arrayed and columnar one-dimensional organic semiconductor stacks, were poised for direct characterization with spectroscopic and electrochemical techniques.

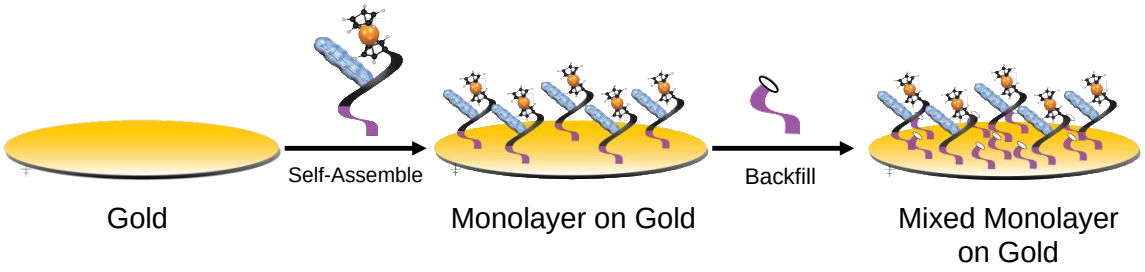

Figure 4.4: Self-assembly of the monolayers**.** Illustration of the procedure required to form a self-assembled mixed monolayer on gold from **P1.**

We initially investigated our monolayers with X-ray photoemission spectroscopy (XPS), a surface-sensitive technique that can map the occupied energetic states of a material and distinguish the chemical environments of the material's constituent atoms.[32, 33] As a specific example, the chemical structure and concomitant typical XPS spectrum for a **P1** mixed monolayer are illustrated in Figure 4.5A and Figure 4.5B. The spectrum showed clear signals at energies of 133.9 eV, 286.0 eV, 400.4 eV, and 533.0 eV, corresponding to the phosphorus 2p region, the carbon 1s region, the nitrogen 1s region, and the oxygen 1s region, respectively. Notably, the peaks' locations were in good agreement with previous reports for analogous chemical functionalities in DNA monolayers, and their relative intensities and line shapes were consistent with the mixed monolayers' presumed stoichiometry and chemical environments.[34-36] Indeed, the carbon 1s region featured multiple distinct peaks at energies of 285.2 eV, 286.7 eV, and 288.2 eV, as expected, corresponding to the distinct chemical environments of the alkyl, aromatic, and carbonyl carbon atoms present in the monolayer.[32, 33, 37] In analogous fashion, the

oxygen 1s peak was asymmetric, due to the presence of both sp^2- and sp^3-bonded oxygen atoms in the monolayer. Importantly, a similar analysis for **P2**, **P3**, and **P4** yielded nearly identical results, as shown in Figures S4.5-S4.7. In their entirety, our measurements confirmed the successful formation of self-assembled monolayers, which featured specific and well-defined chemical compositions, from **P1**, **P2**, **P3**, and **P4**.

We proceeded to examine our monolayers with near edge X-ray absorption fine structure spectroscopy (NEXAFS), a surface-sensitive technique that elucidates the electronic characteristics and molecular orientation of surface-confined species.[37-39] As a specific example, typical partial electron yield spectra, which were obtained with the incident electric field parallel (S-polarization) and perpendicular (P-polarization) to the surface, are illustrated in Figure 4.5C for a **P1** mixed monolayer. Given that these carbon K edge spectra closely matched theoretical predictions for PTCDI-based materials[40], we were readily able to assign all of the observed signals. For our analysis, we primarily focused on the two characteristic doublets in the 284 eV to 286 eV energy range, which correspond to carbon 1s$\rightarrow\pi^*$ transitions localized on the PTCDIs' aromatic core and are associated with the LUMO and LUMO+1 orbitals.[40] By evaluating the dependence of these signals' intensity on the polarization of the electric field (the dichroism), we directly obtained the average orientation of the PTCDIs within our monolayers. Here, our analysis indicated that the **P1** macromolecule possessed an average tilt angle of ~ 61° ± 2° with respect to the substrate surface. Moreover, by repeating the same process for our other macromolecules, we discovered that **P2**, **P3**, and **P4** featured nearly identical substrate-relative orientations, with average angles of ~ 61°, ~ 60°, and ~ 60°, respectively (Figures S4.5-S4.7). These findings were in reasonable agreement with literature precedent, as tilt angles of ~ 45-60° and ~ 62-85° have been reported for mixed mercaptohexanol/DNA[30, 31] and alkyl monolayers[24,

[26], respectively. Altogether, our measurements indicated that **P1**, **P2**, **P3**, and **P4** featured the same average ensemble orientations within our self-assembled monolayers.

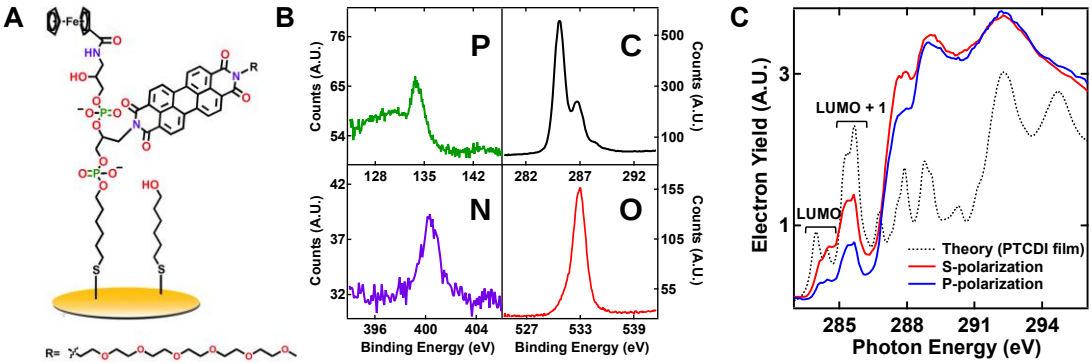

Figure 4.5: X-ray spectroscopy of the P1 monolayer. (A) Chemical structure of the **P1** monolayer formed on gold. The atoms are colored to correspond to the signals in **B**. (B) Typical phosphorous 2p, carbon 1s, nitrogen 1s, and oxygen 1s XPS spectra obtained for the **P1** monolayer, with the color of the traces correlated to the colored atoms in **A**. (C) Carbon K-edge NEXAFS spectra of the **P1** monolayer measured with the electric field polarized parallel (S-polarization, red) and perpendicular (P-polarization, blue) to the gold surface. The predicted theoretical spectrum is also shown (dashed line). The regions that correspond to the LUMO and LUMO+1 are indicated with square brackets. The substrate-relative orientation of the PTCDIs within the monolayer was calculated from the difference in signal intensity (dichroism) between the bracketed peaks for the red and blue traces.

Having evaluated our monolayers' chemical and structural compositions, we in turn interrogated their electrochemical properties with cyclic voltammetry (CV), a technique that facilitates tandem evaluation of the redox, electronic, and physical characteristics of surface-confined species.[27] Figure 4.6 shows a direct comparison of the typical cyclic voltammograms obtained for monolayers from **P1**, **P2**, **P3**, and **P4**. Within the accessible potential window, we observed quasi-reversible or reversible redox couples at –0.43 V vs. Ag/AgCl for **P1**; –0.39 V and –0.67 V vs. Ag/AgCl for **P2**; –0.36 V and –0.59 V vs. Ag/AgCl for **P3**; and –0.34 V, –0.50 V, and –0.68 V vs. Ag/AgCl for **P4**. Based on literature precedent for the redox activity of PTCDIs[16, 17], as well as our previous studies of PTCDI-modified DNA monolayers[22], we attributed these redox couples to reduction of our constructs' LUMO and other energetically similar orbitals. Interestingly, due to the appearance of new and distinct redox states, we inferred that the electronic properties of our constructs were complex and not dictated solely by the number of incorporated PTCDIs.

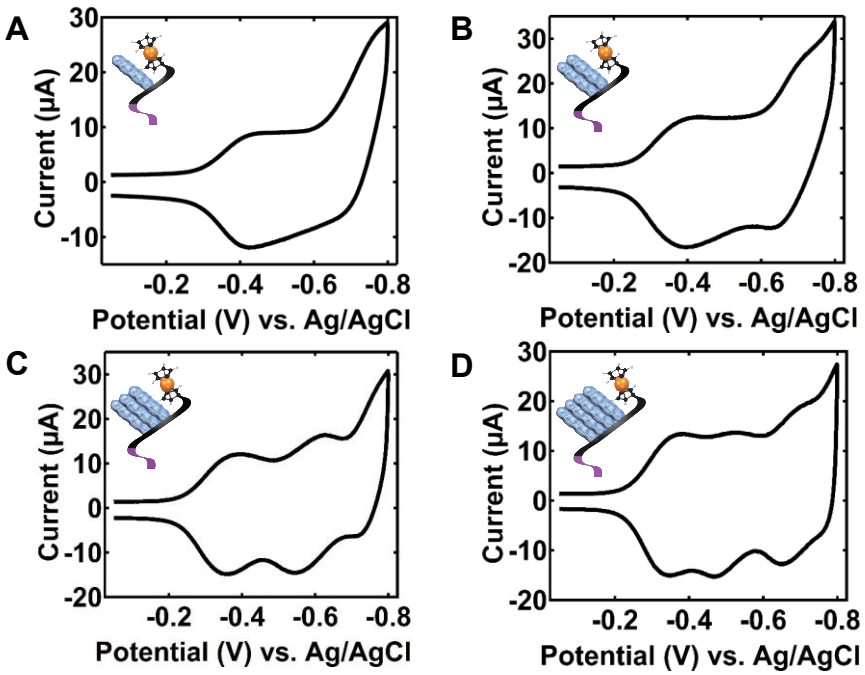

Figure 4.6: Electrochemistry of the monolayers. Typical cyclic voltammetry (CV) for mixed monolayers from (A) **P1,** (B) **P2,** (C) **P3,** and (D) **P4** monolayers obtained at a scan rate of 5 V/s.

To interpret our electrochemical findings, we performed density functional theory (DFT) calculations. Here, we employed the long-range-corrected CAM-B3LYP functional[41], which provides improved accuracy for large systems, within the Gaussian 09 package[42]. For these calculations, we used the equilibrium geometries obtained from the molecular dynamics simulations to generate molecular orbital isosurface plots for **P1**, **P2**, **P3**, and **P4**, as illustrated for the LUMO and LUMO+1 orbitals in Figure 4.7 (the corresponding HOMO plots are illustrated in Figure S4.8). We were surprised to discover that the orbitals featured contributions from every constituent PTCDI, with the electron density delocalized over either the entirety (**P1**, **P2**, and **P3**) or majority (**P4**) of our constructs' aromatic cores. These observations clearly demonstrated that the PTCDI subunits of **P1**, **P2**, **P3**, and **P4** were not electronically independent of one another due to the presence of strong through-space intramolecular coupling, in analogy to the model case of Figure 4.1A. Together with the electrochemical measurements, the simulations suggested that our macromolecules were more than the sum of their PTCDI subunits and effectively resembled single electroactive units.

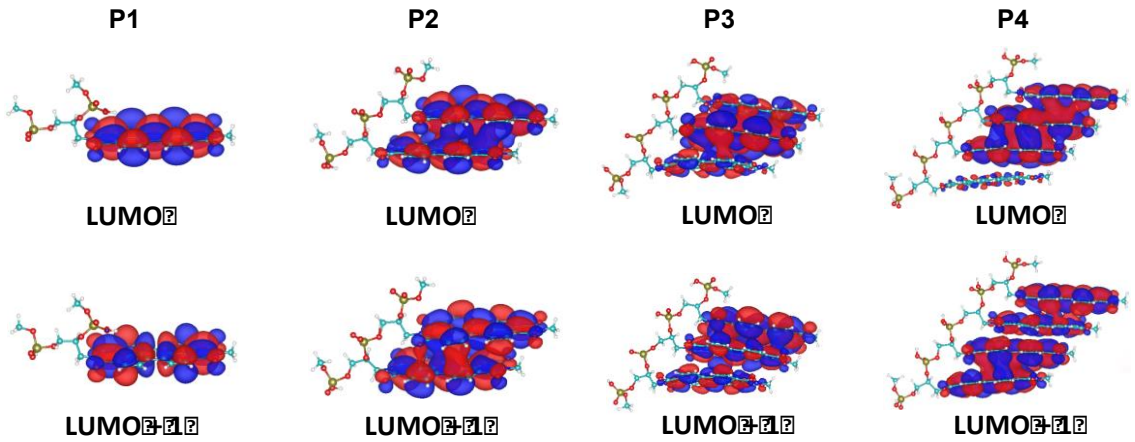

Figure 4.7: Molecular orbitals of the model systems. Isosurface plots for the LUMO and LUMO+1 of **P1, P2, P3,** and **P4**. The isosurface values for all of the plots have been set to 0.01 |e|/Å^3.

We continued our analysis by comparing the ground state unoccupied orbital energies for **P1**, **P2**, **P3**, and **P4** obtained from the calculations and experimental measurements (Figure 4.8). Figure 4.8A shows the theoretically predicted energies for our macromolecules as a function of the number of constituent PTCDIs. The theoretical calculations predict LUMO energies of –2.66 eV, –3.01 eV, –3.36 eV, and –3.36 eV for **P1**, **P2**, **P3**, and **P4**, respectively, and LUMO+1 energies of –2.85 eV, –3.17 eV, and –3.08 eV for **P2**, **P3**, and **P4**, respectively. In analogous fashion, Figure 4.8B shows the experimentally measured energies for our macromolecules as a function of the number of constituent PTCDIs. By using the pendant ferrocene as an internal standard[27, 43], we obtained reliable values for the LUMO energies of –4.09 eV, –4.15 eV, –4.19 eV, and –4.22 eV for **P1**, **P2**, **P3**, and **P4**, respectively, and LUMO+1 energies of –3.87 eV, –3.96 eV, and –4.07 eV for **P2**, **P3**, and **P4**, respectively. Here, the magnitudes of the experimentally determined energies were not in perfect agreement with the theoretically determined values, presumably due to the limited accuracy of the DFT-CAMB3LYP approximation and the exclusion of solvent and substrate effects in the simulations. Nonetheless, both the theoretical and experimental measurements exhibited similar trends and confirmed that an increase in the number of PTCDI subunits (upon moving from **P1** to **P4**) induced a general lowering of the LUMO and led to the appearance of distinct new energetic states. Together, our measurements and analysis demonstrated that we were directly observing the evolution of electronic structure for a stacked one-dimensional organic semiconductor, exactly as illustrated in Figure 4.1A.

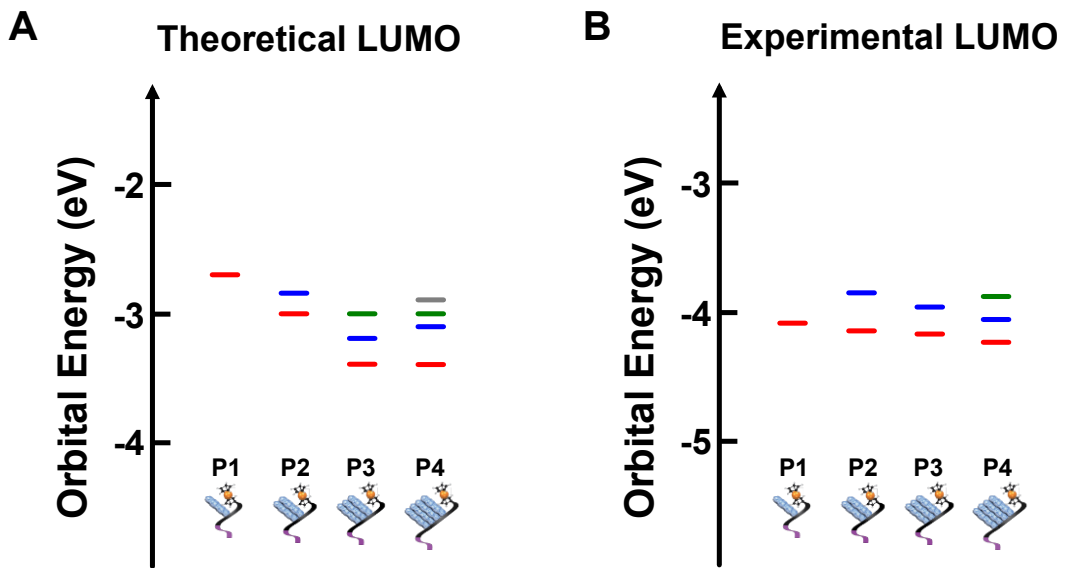

Figure 4.8: The partial orbital energy diagram for the model systems. (A) The theoretically determined orbital energy diagram for the lowest unoccupied orbitals of **P1, P2, P3,** and **P4**. (B) The experimentally determined orbital energy diagram for the lowest unoccupied orbitals of **P1, P2, P3,** and **P4**.

We proceeded to demonstrate the unique advantages afforded by our chemically well-defined model systems, i.e. the ability to access the intermediate regime where the evolution in both the electronic structure and numerous crucial associated spectroscopic properties occurs.[11] For this purpose, we employed synchrotron-based resonant photoemission spectroscopy (RPES).[44-49] In a typical incarnation of this technique, X-ray radiation promotes an atomically localized core electron to a LUMO orbital, producing an excited electron and a core-hole (Figure 4.9A, left). Subsequently, the excited electron relaxes *via* multiple processes, including ones known as participator decay (Figure 4.9A, middle) and exciton dissociation (Figure 4.9A, right). In the participator decay process, the core-excited electron participates in the core-hole decay and another electron from the HOMO is emitted (Figure 4.9A, middle), yielding a resonantly enhanced peak that is degenerate with but distinguishable from the direct photoemission process. In the exciton dissociation process, the core-excited electron can delocalize from the LUMO into the substrate or general surrounding electronic environment (Figure 4.9A, right), quenching the

intensity of the participator decay signal. When resonant photoemission measurements are performed for chemically similar systems that are well and poorly coupled to their surroundings, the exciton dissociation times and, thus, charge transfer dynamics can be readily and directly quantified. Here, we note that RPES possesses exquisite elemental and orbital specificity, providing direct access to nearly arbitrary atomic sites and molecular orbitals.[44-49] Moreover, the technique's use of the intrinsic core-hole lifetime as an internal reference "clock" (CHC) yields femtosecond (or even sub-femtosecond) temporal resolution[44-49], as demonstrated with measurements of charge transfer dynamics for cyclophanes and shape-complementary donor/acceptor pairs[50, 51]. Thus, RPES is highly advantageous for the study of charge transfer dynamics at surface-confined organic semiconductors.

We first performed RPES measurements for self-assembled monolayers from **P1**, **P2**, **P3**, and **P4,** as well as a PTCDI multilayer control (Figure S4.13). As an example, the resulting intensity as a function of both photon energy and electron binding energy plot for **P1**, which has been normalized to the incident photon flux, is shown in Figure 4.9B (a wider photon energy range is included as Figure S4.9). To facilitate our analysis, non-resonant background signals from direct photoemission have been specifically subtracted, allowing for unambiguous interpretation of the remaining HOMO participator decay signals.[52, 53] For photon energies between 284 eV and 286 eV, we observed a peak at a binding energy of 3.4 eV and a broad hump across the general Auger decay energy range. Based on the NEXAFS spectra in Figure 5C and literature precedent for PTCDIs[52, 53], we unambiguously attributed the sharp peak to HOMO participator decay of a carbon 1s core electron that had been promoted to the LUMO and LUMO+1 orbitals, with the broad hump corresponding to various Auger background processes. Importantly, when we repeated the same analysis for **P2**, **P3**, **P4**, and the PTCDI multilayer

control, we observed very similar characteristic signals, which could be assigned in analogous fashion (Figure S4.10-S4.13). These findings indicated that we could directly measure core-level exciton dissociation times for our macromolecules, facilitating direct unambiguous comparisons of their intrinsic charge transfer dynamics under identical conditions.

We next used our two-dimensional resonant photoemission plots for **P1**, **P2**, **P3**, and **P4** to determine the molecules' respective core-level exciton dissociation times. We initially evaluated the resonant photoemission signals obtained for **P1** at an excitation energy of 285.4 eV, which corresponded to the promotion of a carbon 1s core electron to the LUMO+1 (see the white dashed line in Figure 4.9B and red trace in Figure 4.5C). The sharp increase in intensity at a binding energy of 3.4 eV resulted from the participator decay of the promoted electron (see the red trace in Figure 4.9C). To quantify the exciton dissociation times, we employed our PTCDI multilayer as a reference, for which the constituent molecules were poorly coupled to their surroundings and the participator decay signal at 3.4 eV was larger than the signal found for **P1** (see the gray trace in Figure 4.9C). By comparing the intensities of the participator decay signals for **P1** and the PTCDI multilayer (Figure 4.9C), we obtained a quenching ratio and used established procedures to convert it into a dissociation time *via* the equation[44]

$$\tau_{CT} = \tau_{CH} \frac{I_{coupled}}{I_{isolated} - I_{coupled}} \quad (1)$$

where τ_{CH} = 6 fs is the reported core-hole lifetime for carbon 1s, $I_{isolated}$ is the integrated participator intensity for an isolated molecular system (such as the PTCDI multilayer standard), and $I_{coupled}$ is the participator intensity for the **P1** monolayer.[44] By assuming that all aromatic carbon atoms are equally coupled to their surroundings, we calculated that **P1**'s average exciton

dissociation time was 11.5 ± 1.5 fs. Overall, the above findings were fully consistent with literature reports for aromatic molecules adsorbed on metal substrates[48-53] and provided a definitive quantitative measure of charge transfer dynamics in **P1** monolayers.

We in turn analyzed the two-dimensional resonant photoemission plots for **P2**, **P3**, and **P4** to determine their intrinsic exciton dissociation times (Figures S4.10-S4.12). For these three macromolecules, we again evaluated the resonant photoemission signals at 3.4 eV (see the blue, green, and black traces in Figure 4.9C). By comparing the intensities of the participator decay signals for **P2**, **P3**, and **P4** to the PTCDI multilayer, we obtained quenching ratios and extracted average core-level exciton dissociation times of 8.4 ± 1.0 fs for **P2**, 5.2 ± 0.5 fs for **P3**, and 5.7 ± 0.6 fs for **P4** from the equation above. Our data showed that the exciton dissociation times decreased as the number of PTCDI building blocks in our constructs increased (Figure 4.9D), with a significant difference between the lifetimes found for monomeric **P1** and multimeric **P4**.

Here, we note that the measured trend in the core-level exciton dissociation times was quite surprising. Indeed, the larger **P2**, **P3**, and **P4** model systems are distal from the surface and thus, relative to **P1**, should be more poorly coupled with the surrounding electronic environment. Consequently, the exciton dissociation times might be expected to increase, rather than decrease, upon moving from **P1** to **P4**.[48-53] Given the similar surface-relative orientations and chemical compositions of **P1**, **P2**, **P3**, and **P4**, the observed unexpected trend likely stemmed from the fact that our model systems featured an intramolecular interaction-induced change in their properties and resembled single electronic units, as exemplified by delocalization of the LUMO and LUMO+1 for **P1**, **P2**, **P3**, and **P4** (Figure 4.7). Such findings directly underscored the utility of the presented methodology for accessing otherwise difficult-to-capture functional consequences of electronic structure evolution in organic semiconductors.

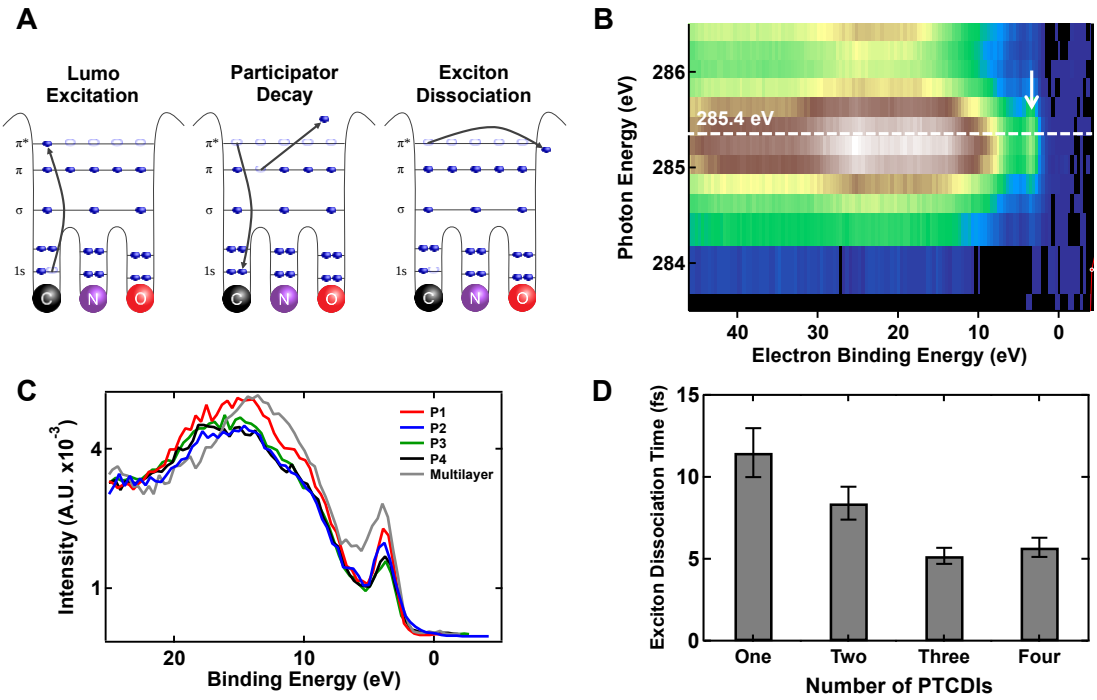

Figure 4.9: Resonant photoemission spectroscopy of the model systems. (A) Illustration of (left) the promotion of a core electron to the LUMO, (middle) the participator decay process, and (right) the exciton dissociation process. (B) Resonant photoemission spectroscopy (RPES) intensity map obtained for a **P1** monolayer, where the photon energy range of 284 to 286 eV encompasses the LUMO- and LUMO+1-associated signals. The white dashed line at an energy of 285.4 eV corresponds to the line profiles in **C**. (C) The normalized resonant participator intensity profile for the **P1** (red)**, P2** (blue)**, P3** (green)**, P4** (black) monolayers, as well as the PTCDI multilayer (grey). The data was extracted from the resonant photoemission intensity maps obtained for the four model systems and the multilayer at photon energies of 285.4 eV. (D) The exciton dissociation times obtained extracted from the quenching of the signal at 3.4 eV for **P1, P2, P3, P4** in part **C**. Note that the exciton dissociation times decrease as the number of PTCDI building blocks increases.

We have presented a powerful synthetic strategy for the investigation of disordered electronic materials, and in particular, organic semiconductors. For such materials, the precise arrangement of individual small molecular building blocks with well-defined intermolecular interactions has often proven difficult to control within traditional synthetic or self-assembly contexts; many studies must rely on the tedious (and often fortuitous) growth of X-ray quality single crystals for fundamental studies. Our bioinspired approach deftly sidesteps such challenges by enabling the rational construction of well-defined, one-dimensional ensembles comprised of PTCDIs covalently appended to a phosphodiester backbone. Indeed, to the best of

our knowledge, the described sequence-controlled model systems are completely unprecedented in the literature, and our methodology represents a key step forward from a synthetic perspective. In principle, this strategy could provide exceptional opportunities for the rational design and preparation of other exciting organic semiconductor constructs from nearly arbitrary building blocks.

The described designer model systems facilitate the study of the intermediate size regime where small molecules start to evolve into materials (Figure 4.1A). Indeed, in contrast to the properties of inorganic semiconductors, which are dictated by covalent interactions and long-range periodicity, the properties of organic semiconductors are determined primarily by weaker, short-range non-covalent intermolecular interactions. At length scales of ~ 1 to ~ 5 nm, such complex interactions are particularly influential and even subtle molecular-level changes result in dramatic, and often unexpected, structural and functional consequences. Here, by evaluating a series of well-defined macromolecules, we access this crucial intermediate size regime with precise chemical control and capture the evolution of electronic structure for stacked PTCDIs with both experimental and computational techniques. For these model systems, we surprisingly find that the core-level exciton dissociation time decreases, rather than increases, with the number of incorporated PTCDIs (Figure 4.9C). This unexpected finding demonstrates that our approach is particularly useful for elucidating definitive structure-function relationships in the intermediate size regime and, thus, for ultimately informing the bottom-up design of bulk electronic properties in organic semiconductors.

The use of self-assembled monolayers from our model systems facilitates the interrogation of charge transfer phenomena at organic/inorganic interfaces. These phenomena, which include exciplex formation, electron transfer, Förster energy transfer, exciton generation,

and exciton Bohr radius, among others (Figure 4.1B), often dictate the performance of devices such as organic transistors and solar cells. However, they remain challenging to probe experimentally with excellent chemical, temporal, and spatial resolution, especially at well-defined and device-relevant material interfaces. By forming monolayers from our constructs and leveraging the advantages of resonant photoemission spectroscopy, we specifically access and quantify the change in charge transfer dynamics within a device-relevant context (Figure 4.9). Given that core-level excitons share common features with valence-level excitons for organic semiconductors[54], our findings are likely to shed insight into interface-associated charge transfer dynamics for a wide range of organic semiconductor-based devices.

Finally, our measurements are interesting to consider from the perspective of the DNA conductivity field[55-57]. Due to their phosphodiester backbone and aromatic building block spacing, our model systems share clear and common features with DNA. Thus, it is appropriate to directly compare our resonant photoemission spectroscopy measurements to analogous ones performed for single-stranded and duplex DNA. The exciton dissociation times of ~ 6 to ~ 12 fs found for our constructs are virtually identical to charge transfer times of ~ 6 fs found for DNA[58, 59], which is quite remarkable. This comparison supports the classic notion that DNA is similar to one-dimensional aromatic crystals[58] and further underscores the broad, general relevance of our findings for a wide range of materials.

4.5 Conclusion

In summary, we prepared several characteristic representatives of a novel class of chemically well-defined PTCDI-based organic semiconductor ensembles. We then confirmed the identity and likely geometry of these macromolecules with biochemical techniques and

molecular dynamics simulations. We in turn characterized the evolution of these model systems' electronic properties through a combination of electrochemical measurements, X-ray spectroscopy experiments, and density functional theory simulations. Subsequently, we evaluated intrinsic charge transfer dynamics for our constructs with resonant photoemission spectroscopy, finding unexpected and surprising changes in their core-level exciton dissociation times. Altogether, our studies hold broad general relevance for fundamentally understanding structure-function relationships in arbitrary organic materials, nanoscale charge transfer phenomena at device-relevant organic/inorganic interfaces, and conductivity in biological and bioinspired systems.

4.6 Supporting Information

4.6.1 Analytical Data for the Perylenediimide Phosphoramidite Precursor (2) and Symmetric PEGylated Perylenediimide (S1).

The product was synthesized according to Scheme 1 in the main text by using established literature protocols[22,23] to afford 820 mg (41%) of **2** as a dark red solid. During the purification, 377 mg (21%) of side product **S1** (Figure S4.13) was also collected as a dark red solid.

(2) ^{1}H NMR (500 MHz, CD_2Cl_2) δ 8.37 (dd, *J* = 18.2, 7.9 Hz, 4H), 8.16 (t, *J* = 8.5 Hz, 4H), 7.54 – 7.49 (m, 2H), 7.40 – 7.35 (m, 4H), 7.33 – 7.27 (m, 2H), 7.25 – 7.17 (m, 1H), 6.89 – 6.78 (m, 4H), 4.56 (dd, *J* = 14.4, 9.7 Hz, 1H), 4.39 (dt, *J* = 7.2, 3.7 Hz, 2H), 4.29 – 4.24 (m, 2H), 3.85 – 3.81 (m, 2H), 3.76 (d, *J* = 1.2 Hz, 6H), 3.72 – 3.67 (m, 2H), 3.62 – 3.51 (m, 16H), 3.49 – 3.46 (m, 2H), 3.31 (s, 5H), 3.18 (d, *J* = 6.5 Hz, 1H). ^{13}C NMR (126 MHz, CD_2Cl_2) δ 163.7, 163.1, 159.0, 145.5, 136.4, 133.8, 133.6, 131.0, 130.8, 130.5, 128.8, 128.7, 128.5, 128.2, 127.1, 125.4, 123.0, 113.4, 86.4, 72.2, 70.8, 70.7, 70.5, 69.6, 68.1, 66.3, 59.0, 55.6, 44.3, 39.8, 30.1. ESI MS Found 1067.36 (M + Na).

(S1) ^{1}H NMR (500 MHz, CD_2Cl_2) δ 8.24 (d, *J* = 7.9 Hz, 4H), 7.99 (d, *J* = 8.1 Hz, 4H), 4.37 (t, *J* = 6.2 Hz, 4H), 3.83 (t, *J* = 6.1 Hz, 4H), 3.71 (dd, *J* = 5.7, 3.7 Hz, 4H), 3.66 – 3.54 (m, 32H), 3.50 – 3.46 (m, 4H), 3.32 (s, 6H). ^{13}C NMR (126 MHz, CD_2Cl_2) δ 163.4, 134.2, 131.2, 129.1, 125.9, 123.3, 123.2, 72.4, 71.1, 71.1, 71.0, 71.0, 70.9, 70.8, 68.4, 59.2, 39.9. ESI MS Found 969.36 (M + Na).

4.6.2 Analytical Data for the PTCDI Phosphoramidite (3).

The product was synthesized according to Scheme 1 in the main text by using established literature protocols[22,23] to afford 438 mg (92%) of **3** as a dark red solid. This product contained a mixture of diastereomers. ^{1}H NMR (600 MHz, CD_2Cl_2) δ 8.70 – 8.34 (m, 8H), 7.61 – 7.05 (m, 9H), 6.86 – 6.67 (m, 4H), 4.67 – 4.50 (m, 1H), 4.45 – 4.39 (m, 2H), 4.36 – 4.21 (m, 1H), 3.82 (t, *J* = 6.5 Hz, 2H), 3.75 (d, *J* = 2.3 Hz, 1H), 3.73 (s, 2H), 3.70 (d, *J* = 5.0 Hz, 3H), 3.69 – 3.65 (m, 3H), 3.65 (s, 2H), 3.61 – 3.46 (m, 21H), 3.32 (d, *J* = 1.6 Hz, 3H), 3.24 – 3.02 (m, 1H), 2.42 (td, *J* = 6.7, 3.7 Hz, 1H), 2.33 (t, *J* = 6.6 Hz, 1H), 1.05 (dd, *J* = 11.9, 6.8 Hz, 6H), 0.98 (dd, *J* = 12.9, 6.8 Hz, 6H). ^{13}C NMR (126 MHz, CD_2Cl_2) δ 163.7, 163.6, 163.6, 159.1, 159.0, 159.0, 158.9, 145.6, 145.5, 136.7, 136.6, 136.4, 136.4, 134.7, 134.6, 134.6, 134.4, 131.5, 131.3, 130.7, 130.5, 130.5, 129.5, 129.5, 128.7, 128.4, 128.3, 128.2, 127.1, 126.6, 126.5, 123.7, 123.6, 123.5, 123.5, 123.4, 123.3, 118.3, 118.1, 113.6, 113.5, 113.5, 113.4, 113.4, 86.7, 86.7, 72.4, 71.2, 71.1, 71.0, 70.9, 70.8, 70.2, 68.4, 66.2, 59.2, 59.0, 58.9, 58.8, 58.6, 55.7, 55.7, 55.6, 55.6, 45.8, 45.8, 43.7, 43.6, 43.5, 43.4, 39.9, 24.9, 24.8, 24.8, 24.7, 24.7, 23.2, 23.2, 20.7, 20.6, 20.5, 20.4. ^{31}P NMR (243 MHz, CD_2Cl_2) δ 149.7 (d, *J* = 15.9 Hz). ESI MS Found 1267.52 (M + Na).

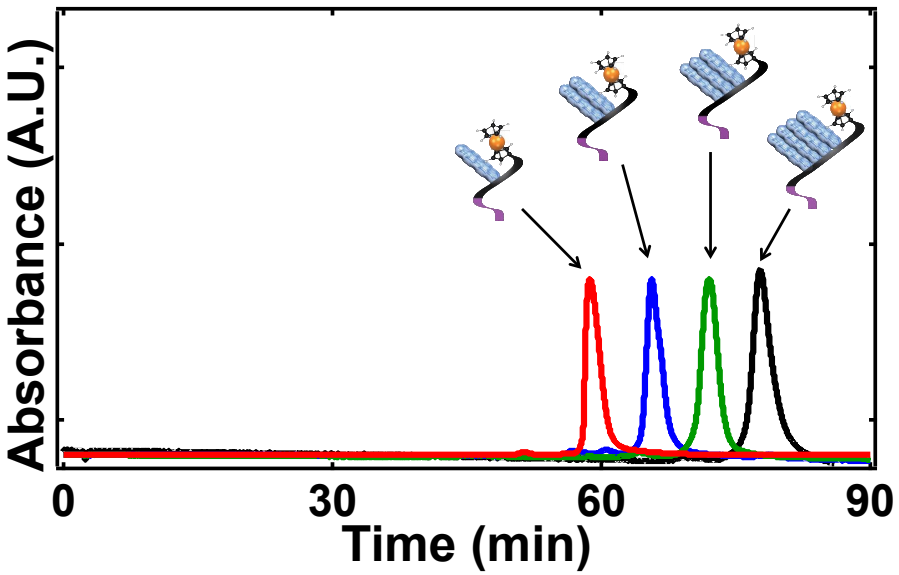

Figure S4.1: High-performance liquid chromatography of the model systems. Typical HPLC chromatograms for macromolecules **P1**, **P2**, **P3**, and **P4**.

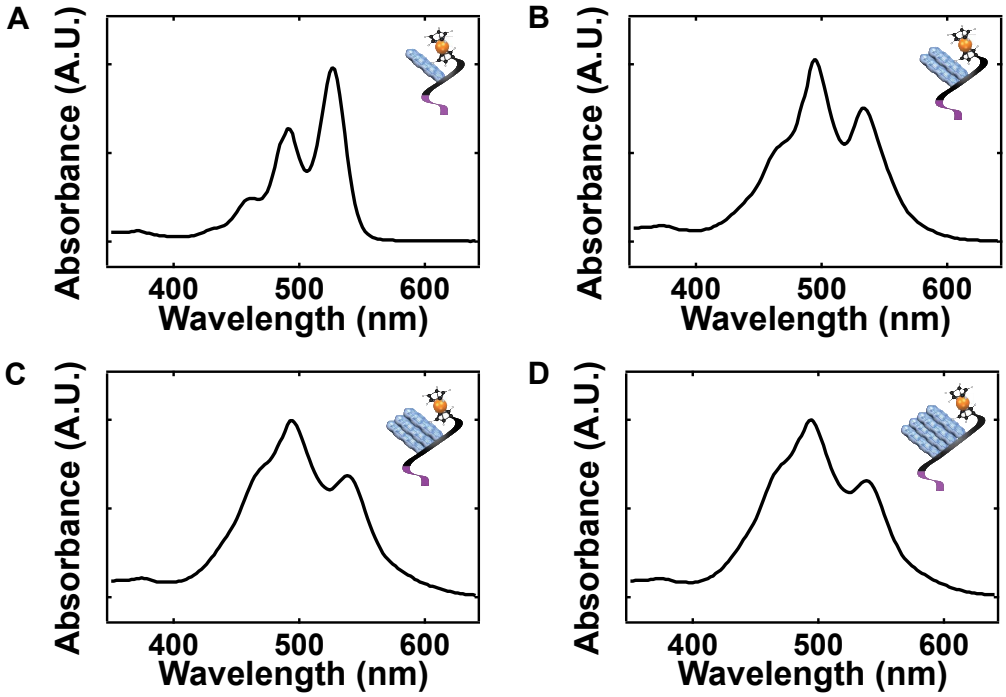

Figure S4.2: UV-vis spectroscopy of the model systems. Normalized UV-vis absorption spectra for macromolecules (A) **P1**, (B) **P2**, (C) **P3**, and (D) **P4**.

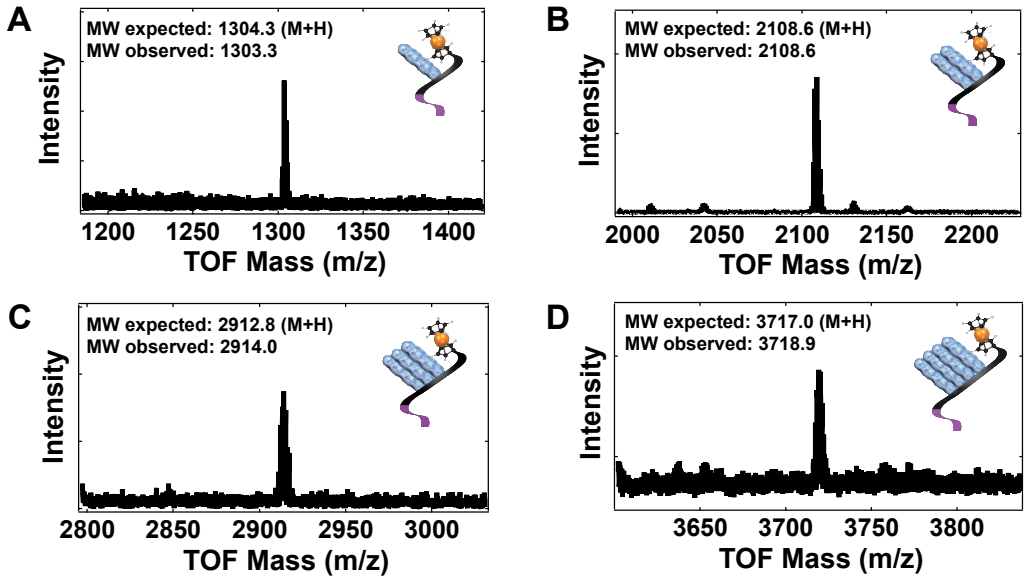

Figure S4.3: Mass spectrometry of the model systems. Experimental MALDI-TOF spectra for macromolecules (A) **P1**, (B) **P2**, (C) **P3**, and (D) **P4**.

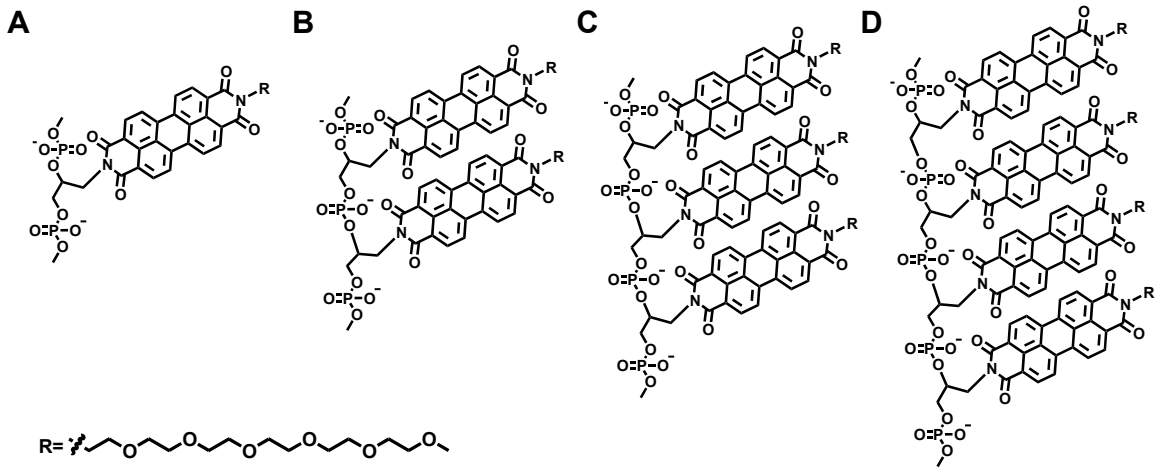

Figure S4.4: Subunits for the model systems**:** The chemical structures of the PTCDI subunits used for the molecular dynamics simulations. The subunits correspond to macromolecules (A) **P1**, (B) **P2**, (C) **P3**, and (D) **P4**.

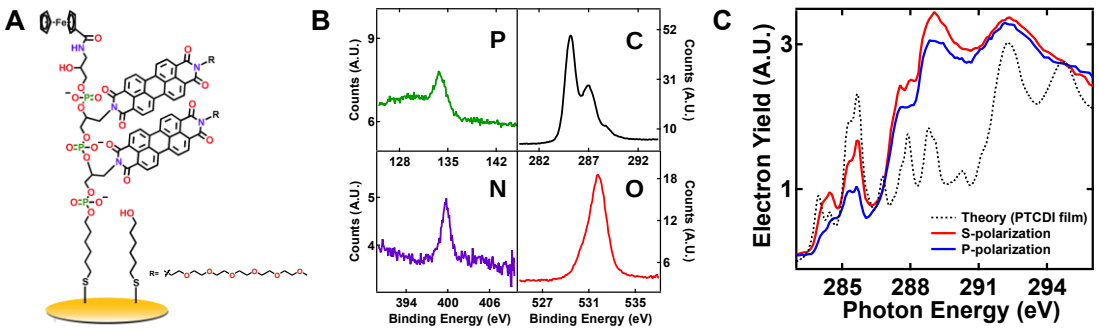

Figure S4.5: X-ray spectroscopy of the P2 monolayer. (A) Chemical structure of the **P2** monolayer formed on gold. The atoms are colored to correspond to the signals in B. (B) Typical phosphorus 2p, carbon 1s, nitrogen 1s, and oxygen 1s XPS spectra obtained for the **P2** monolayer, with the color of the traces correlated to the colored atoms in A. (C) Carbon K-edge NEXAFS spectra of the **P2** monolayer measured with the electric field polarized parallel (red) and perpendicular (blue) to the gold surface. The predicted theoretical spectrum is also shown (dashed line).[40] The substrate-relative orientation reported for the PTCDIs within the monolayer was calculated from the difference in signal intensity (dichroism) between the red and blue traces.

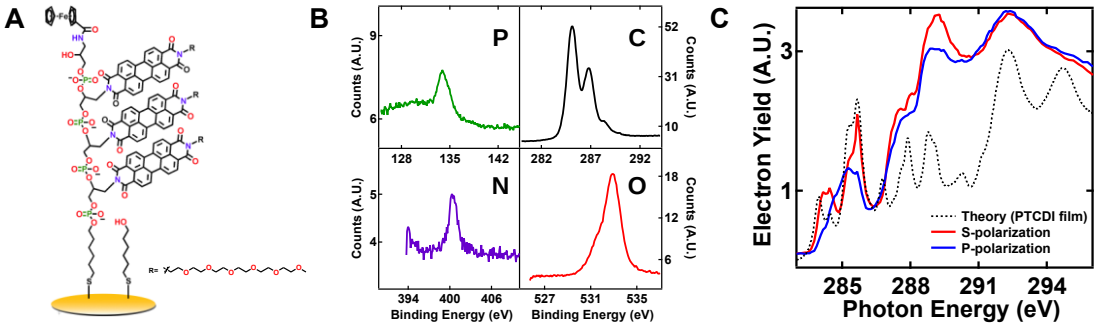

Figure S4.6: X-ray spectroscopy of the P3 monolayer. (A) Chemical structure of the **P3** monolayer formed on gold. The atoms are colored to correspond to the signals in B. (B) Typical phosphorus 2p, carbon 1s, nitrogen 1s, and oxygen 1s XPS spectra obtained for the **P3** monolayer, with the color of the traces correlated to the colored atoms in A. (C) Carbon K-edge NEXAFS spectra of the **P3** monolayer measured with the electric field polarized parallel (red) and perpendicular (blue) to the gold surface. The predicted theoretical spectrum is also shown (dashed line).[40] The substrate-relative orientation reported for the PTCDIs within the monolayer was calculated from the difference in signal intensity (dichroism) between the red and blue traces.

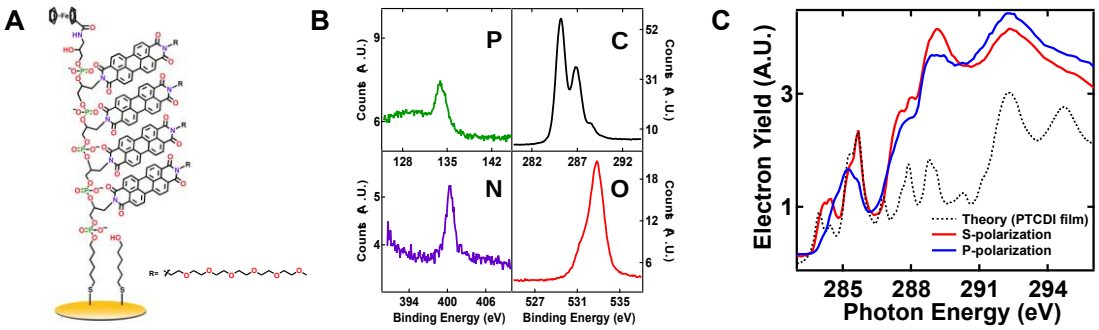

Figure S4.7: X-ray spectroscopy of the P4 monolayer. (A) Chemical structure of the **P4** monolayer formed on gold. The atoms are colored to correspond to the signals in B. (B) Typical phosphorus 2p, carbon 1s, nitrogen 1s, and oxygen 1s XPS spectra obtained for the **P4** monolayer, with the color of the traces correlated to the colored atoms in A. (C) Carbon K-edge NEXAFS spectra of the **P4** monolayer measured with the electric field polarized parallel (red) and perpendicular (blue) to the gold surface. The predicted theoretical spectrum is also shown (dashed line). [40] The substrate-relative orientation reported for the PTCDIs within the monolayer was calculated from the difference in signal intensity (dichroism) between the red and blue traces.

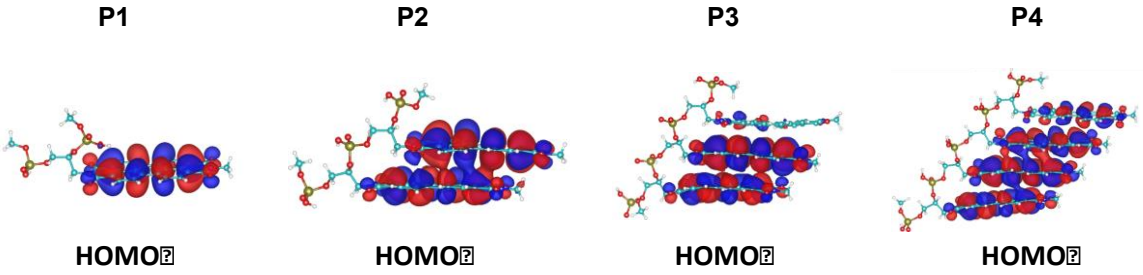

Figure S4.8: Molecular orbitals of the model systems. Isosurface plots for the HOMO of macromolecules **P1, P2, P3,** and **P4**. The isosurface values for all of the plots have been set to 0.01 |e|/Å^3.

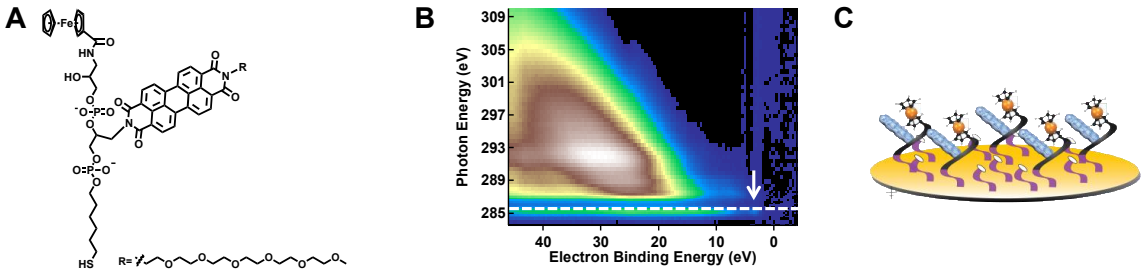

Figure S4.9: Resonant photoemission spectroscopy of P1 (A) Chemical structure of the **P1** macromolecule. (B) The RPES intensity map obtained for the **P1** monolayer. (C) Illustration of a mixed monolayer from **P1**.

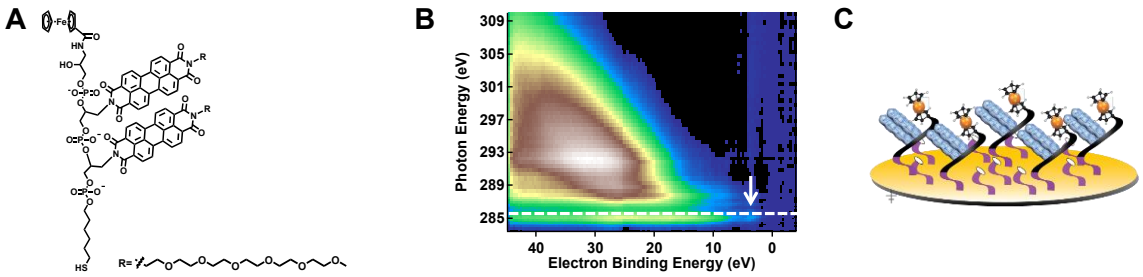

Figure S4.10: Resonant photoemission spectroscopy of P2. (A) Chemical structure of the **P2** macromolecule. (B) The RPES intensity map obtained for the **P2** monolayer. (C) Illustration of a mixed monolayer from **P2**.

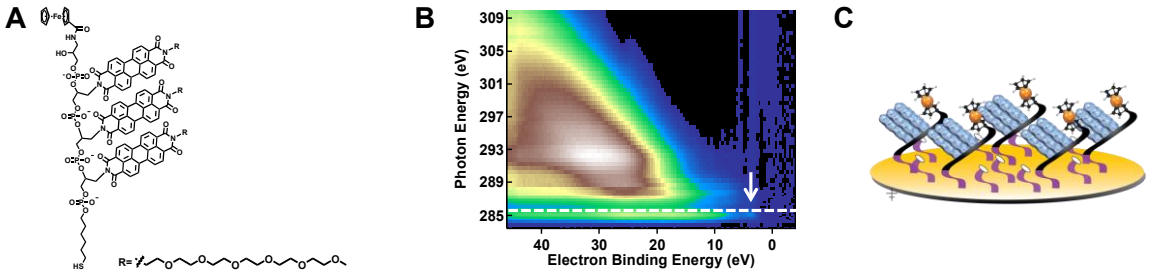

Figure S4.11: Resonant photoemission spectroscopy of P3. (A) Chemical structure of the **P3** macromolecule. (B) The RPES intensity map obtained for the **P3** monolayer. (C) Illustration of a mixed monolayer from **P3**.

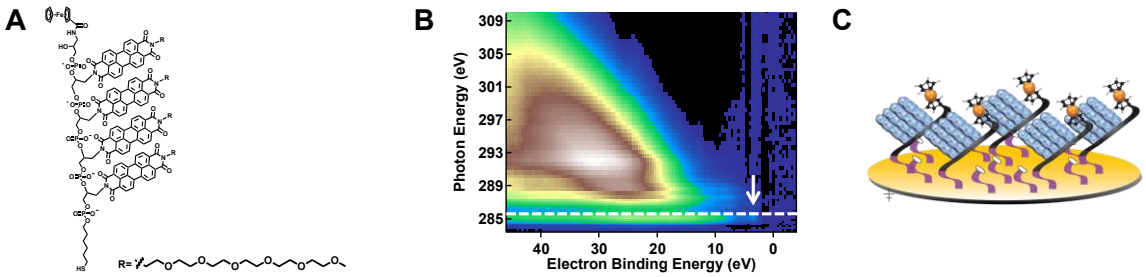

Figure S4.12: Resonant photoemission spectroscopy of P4. (A) Chemical structure of the **P4** macromolecule. (B) The RPES intensity map obtained for the **P4** monolayer. (C) Illustration of a mixed monolayer from **P4**.

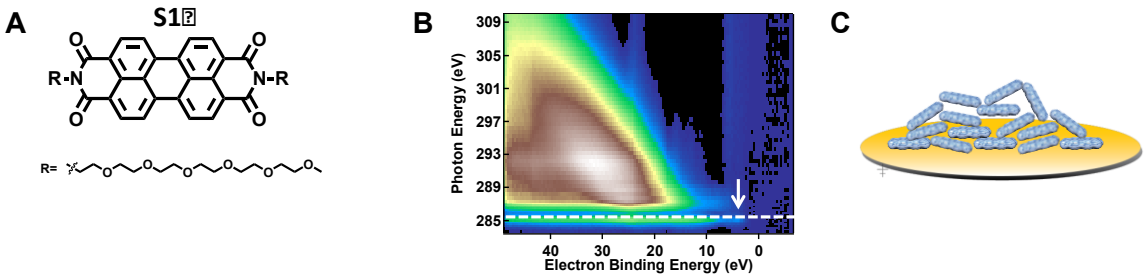

Figure S4.13: Resonant photoemission spectroscopy of the PTCDI multilayer. (A) Chemical structure of the small molecular PTCDI derivative **S1** used to form the multilayer. (B) The RPES intensity map obtained for the **P1** monolayer. (C) Illustration of a multilayer from the small molecular PTCDI derivative.

4.7 References

1. Sirringhaus, H. *Adv. Mater.* **2014**, 26, 1319–1335.
2. Dong, H.; Fu, X.; Liu, J.; Wang, Z.; Hu, W. *Adv. Mater.* **2013**, 25, 6158–6183.
3. Dou, L. *et al. Adv. Mater.* **2013**, 25, 6642–6671.
4. National Renewable Energy Laboratory, "Best Research-Cell Efficiencies" (NREL Revision 08-06-2015, 2015; http://www.nrel.gov/ncpv/images/efficiency_chart.jpg).
5. Hwang, J.; Wan, A.; Kahn, A. *Mater. Sci. Eng. R* ***2009***, 64, 1–31.
6. Braun, S.; Salaneck, W. R.; Fahlman, M. *Adv. Mater.* **2009**, 21, 1450–1472.
7. Liu, C.; Xu, Y.; Noh, Y-.Y. *Mater. Today* **2015**, 18, 79–96.
8. Coropceanu, V. *et al. Chem. Rev.* **2007**, 107, 926–952.
9. Kymissis, I. *Organic Field Effect Transistors: Theory, Fabrication and Characterization*; Springer: New York, New York, **2009**.
10. Tessler, N.; Preezant, Y.; Rappaport, N.; Roichman, Y. ; *Adv. Mater.* **2009**, 21, 2741–2761.
11. Kim, F. S.; Ren, G.; Jenekhe, S. A.; *Chem. Mater.* **2011**, 23, 682–732.
12. Rivnay, J.; Mannsfeld, S. C. B.; Miller, C. E.; Salleo, A.; Toney, M. F.; *Chem. Rev.* **2012**, 112, 5488–5519.
13. Brütting, W.; Adachi, C. Eds. *Physics of Organic Semiconductors,* 2nd ed.; Wiley-VCH: Weinheim, Germany, **2012**.
14. Puniredd, S. R. ; Pisula, W.; Müllen, K. *Handbook of Organic Materials for Optical and (Opto)Electronic Devices;* O. Ostroverkhova, Ed.; Woodhead: Philadelphia, Pennsylvania, **2013**, chap. 2.
15. Köhler, A.; Bässler, H. *Electronic Processes in Organic Semiconductors: An Introduction*; Wiley-VCH: Weinheim, Germany, **2015**.
16. Huang, C.; Barlow, S.; Marder, S. R. *J. Org. Chem.***2011**, 76, 2386–2407.
17. Würthner, F. *Chem. Commun.* **2004**, 1564–1579.
18. Geng, Y.; Li, H.-B.; Wu, S.-X.; Su, Z.-M. *J. Mater. Chem.* **2012**, 22, 20840–20851.
19. Baumstark, D.; Wagenknecht, H.-A.; *Chem. Eur. J.* **2008**, 14, 6640 – 6645.
20. Wilson, T. M.; Zeidan, T. A.; Hariharan, M.; Lewis, F. D.; Wasielewski, M. R. *Angew. Chem. Int. Ed.* **2010**, 49, 2385–2388.
21. Zeidan, T. A.; Carmieli, R.; Kelley, R. F.; Wilson, T. M.; Lewis, F. D.; Wasielewski, M. R. *J. Am. Chem. Soc.* **2008**, 130, 13945–13955
22. Wohlgamuth, C. H.; McWilliams, M. A.; Mazaheripour, A.; Burke, A. M.; Lin, K.-Y.; Doan, L.; Slinker, J. D.; Gorodetsky, A. A. *J. Phys. Chem. C* **2014**, 118, 29084−29090.
23. Markegard, C. B.; Mazaheripour, A.; Jocson, J.-M.; Burke, A. M.; Dickson, M. N.; Gorodetsky, A. A.; Nguyen, H. D. *J. Phys. Chem. B* **2015**, 119, 11459−11465.
24. Love, J. C.; Estroff, L. A.; Kriebel, J. K.; Nuzzo, R. G.; Whitesides, G. M. *Chem. Rev.* **2005**, 105, 1103−1169.
25. Gorodetsky, A. A.; Buzzeo, M. C.; Barton, J. K. *Bioconjugate Chem.* **2008**, 19, 2285–2296.
26. Tao, F.; Bernasek, S. L. *Chem. Rev.* **2007**, 107, 1408−1453.
27. Bard, A. J.; Faulkner, L. R. *Electrochemical Methods: Fundamentals and Applications,* 2nd Ed.; Wiley: Hoboken, New Jersey, **2000**.
28. Iyer, R. P.; Beaucage, S. L. 7.05. Oligonucleotide synthesis. *Comprehensive Natural Products Chemistry, Vol. 7: DNA and Aspects of Molecular Biology*. Kool, Eric T.; Editor. Neth., Elsevier: Amsterdam, **1999**, 105–152.

29. C. B. Reese, *Org. Biomol. Chem.* 3, 3851–3868, **2005**.
30. Levicky, R.; Herne, T. M.; Tarlov, M. J.; Satija, S. K. *J. Am. Chem. Soc.* **1998**, 120, 9787–9792.
31. A. Anne, C. Demaille, *J. Am. Chem. Soc.* **2006**, 128, 542–557.
32. Briggs, D.; Seah, M. P. Eds., *Practical Surface Analysis*, 2nd Ed.; Wiley: Chichester, England, **1992**, vol. 1.
33. Riviere, J. C.; Myhra, S. Eds., *Handbook of Surface and Interface Analysis*; Dekker: New York, New York, **1998**.
34. Herne, T. M.; Tarlov, M. J. *J. Am. Chem. Soc.* **1997**, 119, 8916–8920.
35. Lee, C.-Y. *et al.*, *Anal. Chem.* **2006**, 78, 3316–3325.
36. Petrovykh, D. Y.; Kimura-Suda, H.; Tarlov, M. J.; Whitman, L. J. *Langmuir* **2004**, 20, 429–440.
37. Retzko, I.; Unger, W. E. S. *Adv. Eng. Mater.* **2003**, 5, 519–522.
38. Stöhr, J.; *NEXAFS Spectroscopy* Springer-Verlag: Berlin/Heidelberg, Germany, **1992**.
39. DeLongchamp, D. M.; Lin, E. K.; Fischer, D. A.; *Organic Field-Effect Transistors*, Bao, Z.; Locklin, J.; Eds., CRC Press: New York, New York **2007**, pp. 277–300.
40. Fratesi, G. *et al.*, *Phys.Chem.Chem.Phys.* **2014**, 16, 14834–14844.
41. CAM-B3LYP functional.; A new hybrid exchange–correlation functional using the Coulomb-attenuating method. Yanai, T.; Tew, D. P.; Handy, N. C. *Chem. Phys. Lett*. 2004**,** 393, 51–57.
42. Gaussian 09, Revision D.01, Frisch, M. J.; Trucks, G. W.; Schlegel, H. B.; Scuseria, G. E.; Robb, M. A.; Cheeseman, J. R.; Scalmani, G.; Barone, V.; Mennucci, B.; Petersson, G. A.; Nakatsuji, H.; Caricato, M.; Li, X.; Hratchian, H. P.; Izmaylov, A. F.; Bloino, J.; Zheng, G.; Sonnenberg, J. L.; Hada, M.; Ehara, M.; Toyota, K.; Fukuda, R.; Hasegawa, J.; Ishida, M.; Nakajima, T.; Honda, Y.; Kitao, O.; Nakai, H.; Vreven, T.; Montgomery, Jr., J. A.; Peralta, J. E.; Ogliaro, F.; Bearpark, M.; Heyd, J. J.; Brothers, E.; Kudin, K. N.; Staroverov, V. N.; Kobayashi, R.; Normand, J.; Raghavachari, K.; Rendell, A.; Burant, J. C.; Iyengar, S. S.; Tomasi, J.; Cossi, M.; Rega, N.; Millam, J. M.; Klene, M.; Knox, J. E.; Cross, J. B.; Bakken, V.; Adamo, C.; Jaramillo, J.; Gomperts, R.; Stratmann, R. E.; Yazyev, O.; Austin, A. J.; Cammi, R.; Pomelli, C.; Ochterski, J. W.; Martin, R. L.; Morokuma, K.; Zakrzewski, V. G.; Voth, G. A.; Salvador, P.; Dannenberg, J. J.; Dapprich, S.; Daniels, A. D.; Farkas, Ö.; Foresman, J. B.; Ortiz, J. V.; Cioslowski, J.; Fox, D. J. Gaussian, Inc., Wallingford CT, **2009**.
43. Cardona, C. M.; Li, W.; Kaifer, A. E.; Stockdale, D.; Bazan, G. C. *Adv. Mater.* **2011**, 23, 2367–2371.
44. Brühwiler, P. A.; Karis, O.; Mårtensson, N. *Rev. Mod. Phys.* **2002**, 74, 703–740.
45. Björneholm, O.; Nilsson, A.; Sandell, A.; Hernnäs, B.; Mårtensson, N. *Phys. Rev. Lett.* **1992**, 68, 1892–1895.
46. Ohno, M. *Phys. Rev. B* **1994**, 50, 2566–2575.
47. Karis, O. *et al.*, *Phys. Rev. Lett.***1996**, 76, 1380–1383.
48. Vilmercati, P.; Cvetko, D.; Cossaro, A.; Morgante, A. *Surf. Sci.* **2009**, 603, 1542–1556.
49. Cao, L.; Gao, X.-Y.; Wee, A. T. S.; Qi, D.-C. *Adv. Mater.* **2014**, 26, 7880–7888.
50. Batra, A.; Kladnik, G.; Vázquez, H.; Meisner, J. S.; Floreano, L.; Nuckolls, C.; Cvetko, D.; Morgante, A.; Venkataraman, L. **2012**, *Nat. Comm.* 3, 1038.
51. Schiros, T. *et. al.*, *Adv. Enery Mater.* **2013**, 3, 894–902.
52. Cao, L. *et al.*, *J. Phys. Chem. C* **2014**, 118, 4160−4166.

53. Cao, L. *et al., J. Chem. Phys.* **2011**, 135, 174701 (2011).
54. Schnadt, J.; Schiessling, J.; Brühwiler, P. A. *Chem. Phys.* **2005**, 312, 39–45.
55. Genereux, J. C.; Barton, J. K. *Chem. Rev.* **2010**, 110, 1642–1662.
56. Muren, N. B.; Olmon, E. D.; Barton, J. K. *Phys. Chem. Chem. Phys.* **2012**, 14, 13754–13771.
57. Sontz, P. A.; Muren, N. B.; Barton, J. K. *Acc. Chem. Res.* **2012**, 10, 1792–1800.
58. Wang, L.; Zhang, K.-Q.; Gao, X.; Liu, X.-Y.; Wee, A. T. S. *Appl. Phys. Lett.* **2006**, 89, 013902.
59. Kato, H. S. *et al., Phys. Rev. Lett.* **2004**, 93, 086403.
60. Eley, D. D.; Spivey, D. I. *Trans. Faraday Soc.* **1962**, 58, 411–415.
61. Harris, R. K.; Becker, E. D.; Cabral de Menezes, S. M.; Granger, P.; Hoffman, R. E.; Zilm, K. W. *Pure Appl. Chem.* **2008**, 80, 59–84.
62. Momma, K.; Izumi, F. *J. Appl. Crystallogr.* **2011**, 44, 1272–1276.

CHAPTER 5 Summary and Future Work

We sought to gain a better understanding of charge transport phenomena and structure-function relationships in organic electronic materials. We worked towards this goal by formulating a model system in which the composition, geometry, and assembly are precisely controlled, making it an ideal platform for thorough and systematic studies of organic electronic materials and the evolution of their properties. Our work draws inspiration from DNA, allowing us to leverage well-established oligonucleotide synthesis protocols, assembly techniques, and analytical protocols towards our goals. We began by demonstrating the exquisite control offered by these methodologies by synthesizing a specific DNA sequence that corresponds to a prototypical DNA binding protein, then incorporating this sequence into a microfluidic-encapsulated carbon nanotube field effect transistor. The resulting devices successfully demonstrated high sensitivity of a specific sequence, showcasing the precision that these methodologies allowed us to access.

We continued our exploration by next introducing perylene-3,4,9,10-tetracarboxylic diimides (PTCDIs) as base surrogates, yielding DNA-PTCDI hybrid systems. Examination of the resulting molecular dynamics simulated and chemically synthesized constructs allowed us to establish a foundation for the rational design and construction of precisely defined one-dimensional organic nanowires. Building off of this knowledge, we prepared a novel class of chemically well-defined PTCDI-based organic semiconductor ensembles that could serve as a platform for investigating the emergent electronic phenomena in organic semiconductor materials. The strategies employed to realize these systems can be expanded not only to study systems of increasing length, but also to study systems of varying sequence context (Figure 5.1).

Overall the studies hold relevance for fundamentally understanding structure-function relationships in arbitrary organic materials, nanoscale charge transfer phenomena at device-relevant organic/inorganic interfaces, and electrical conductivity in biological and bioinspired systems.

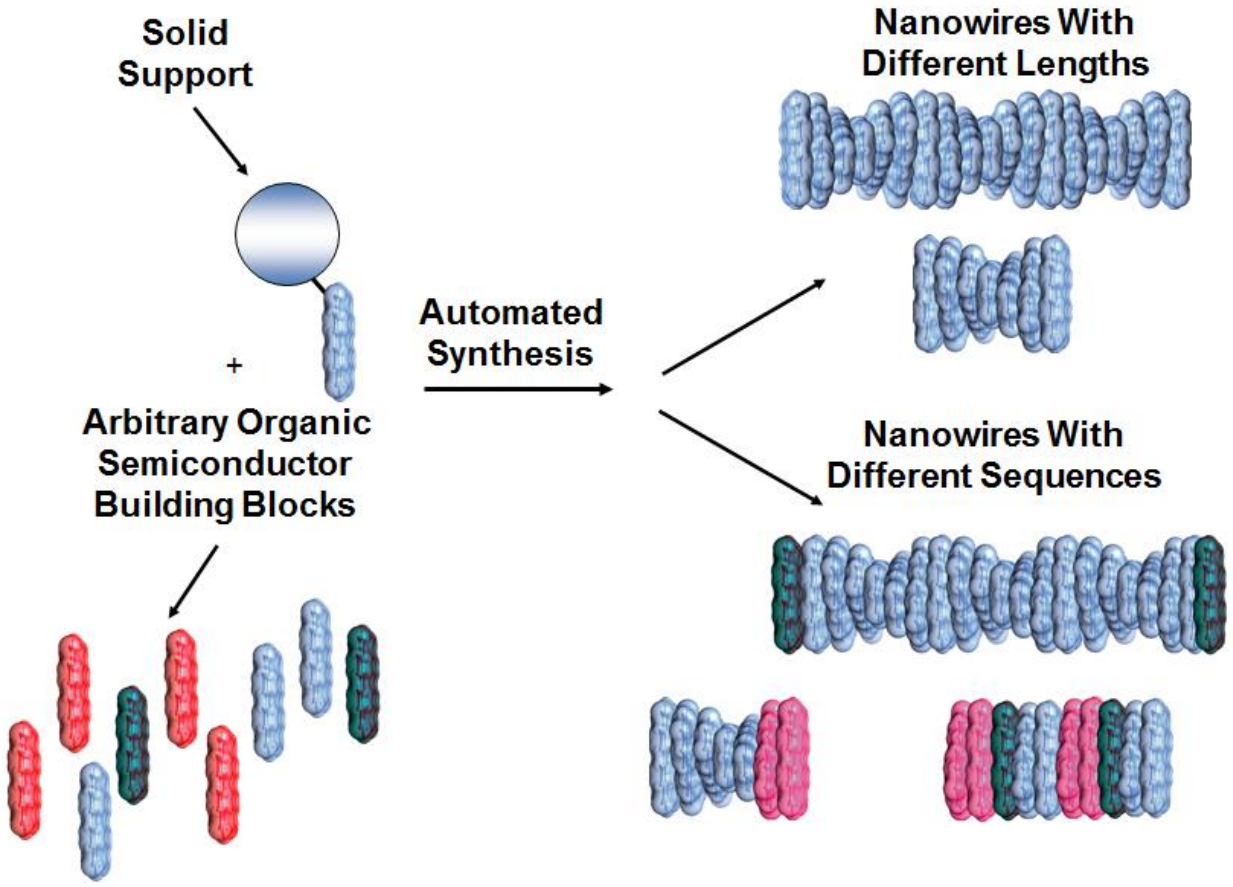

Figure 5.1: The strategy employed to realize our model systems is readily expandable to incorporate other arbitrary organic semiconductor building blocks, granting us access to constructs that vary both by length and by sequence context while maintaining a well-controlled geometry.